INFRARED OBSERVATIONS
OF H II REGIONS

Thesis by

Theodore William Hilgeman

In Partial Fulfillment of the Requirements

For the Degree of

Doctor of Philosophy

California Institute of Technology

Pasadena, California

1970

(Submitted December 10, 1969)

ACKNOWLEDGEMENTS

For help with the equipment, thanks go to D. McCammon, G. Neugebauer, E. Becklin, E. Groth, D. Vail, and G. Forrester.

H. Butcher, E. Ritz, H. Schaefer, and R. Jacques were of considerable help with the observing program. A. R. Hyland kindly took the 100 inch data on NGC 7027 and gave up some 60 inch time so I could observe IC 418.

I would like to thank H. Babcock, Director of the Mount Wilson and Palomar Observatories for the 60 inch observing time, and B. Murray of the Lunar and Planetary Lab for the 24 inch time.

To the California Institute of Technology goes a debt of gratitude for generous financial support.

I am indebted to E. Becklin, G. Neugebauer, R. Leighton, and G. Munch for time spent in discussion and for many useful suggestions.

My Research Advisor, Gerry Neugebauer, has shown patience above and beyond the call of duty.

I have watched with rigor
All he used to do,
And will now with vigor
Work my wonders too.

\- Sorcerer's Apprentice

Finally, my wife Susan typed my first handwritten copy of the thesis, no mean feat, and helped with calculations and keypunching. I am also grateful for her patience during the many nights I had to spend away from home.

What poor astronomers are they
Take women's eyes for stars!

\- John Dowland

ABSTRACT

Spectral data are presented, giving intensities of the Brackett γ (B_7) line at six positions in M 42 and of the Brackett ten through fourteen (B_{10}-B_{14}) lines plus the He $4d^3D-3p^3P^0$ line at three positions in M 42. Observations of the Brackett γ line are also given for the planetary nebulae NGC 7027 and IC 418. Brackett gamma is shown to exhibit an anomalous satellite line in NGC 7027. Broadband data are presented, giving intensities at effective wavelengths of 1.25μ, 1.65μ, 2.2μ, 3.5μ, and 4.8μ for three positions in M 42.

Comparisons with visual and radio data as well as 12 micron and 20 micron data are used to derive reddening, electron temperatures, and electron densities for M 42 and the two planetaries, as well as a helium abundance for M 42. A representative electron temperature of $8400^{\circ}K \pm 1000^{\circ}K$, an electron density of $1.5 \pm 0.1 \times 10^3$ cm^{-3} and a He/H number density ratio of $0.10^{+0.10}_{-0.05}$ are derived for the central region of M 42. The electron temperature is found to increase slightly with distance from the Trapezium.

M 42 is shown to emit in excess of the predicted recombination radiation throughout the entire infrared spectrum. The variations in the excess with wavelength and with position are analyzed to determine which of several physical processes may be operating. The longer wavelength infrared excess is shown to be dominated by dust emission, while the shorter wavelength infrared excess is caused by dust scattering. The dust is shown to be larger than the average interstellar particle. A new feature of the Orion red star ORS-1 is found in that it appears to have a reflection nebula around it.

TABLE OF CONTENTS

TABLE OF CONTENTS (Continued)

LIST OF TABLES

LIST OF TABLES (Continued)

LIST OF FIGURES

LIST OF FIGURES (Continued)

INTRODUCTION

For the past twenty years or so, the Orion Nebula (M 42, NGC 1976) has been considered by astrophysicists to be a primary source for the study of recombination radiation. It is close, relatively bright, and its radiation fits theoretical predictions quite well. This close agreement is important, because many recombination effects cannot be measured in the laboratory. It is in the Orion Nebula and some planetaries that they have found their experimental confirmation.

One of the main reasons why the radiation can be understood on a relatively simple theoretical basis is that in the nebulae, unlike in most other types of astronomical objects, there are few competing processes. The dominant radiation comes from either recombination (continuum and hydrogen lines) or from collisional excitation (metal lines); except for the stars and dust scattering, there is little else.

Recently, however, evidence has begun to build up which would indicate that, in the infrared at least, recombination radiation is not the major source of light. Two micron spatial scans (Becklin, Hilgeman, Neugebauer; unpublished data), as well as infrared photometry (Becklin, private communication), have shown the Orion Nebula to be a somewhat anomalous infrared emitter. The brightest portions of the nebula in the infrared do not correspond well with the visible or radio data. Also, spectral distribution of infrared energy is not consistent with the visible and radio distributions.

Far infrared photometry and spatial scans (Kleinman and Low ApJL 149, 1, 1967; Gillett et al. ApJL 149, 97, 1967; Gillett and Stein ApJL 155, 97, 1969; Ney and Allen ApJL 155, 193, 1969; Wolf ApJL 157, 37, 1969) have established that there is a considerable far infrared excess emission in the Orion Nebula, and in several planetaries.

A good model for the infrared emission is thus called for. The model, and the theoretical and observational basis for it, constitute the thesis.

Before outlining some of the origins of the problem, mention of a few of the visible and radio features of the nebula would be in order. Despite its rather irregular optical appearance, there is good evidence to support the idea that the density distribution is spherical with center somewhat near the Trapezium stars. Line ratios, such as the 3727 O-II lines, show the electron density to be a function only of distance from the Trapezium, even in the dark bay. Radio data, while not yet of good resolution, would also indicate a spherical symmetry. Both the radio and optical data provide temperatures, but there is a significant disagreement which has been explained in several different ways.

When the present thesis was started, the large (several orders of magnitude) excesses at the longer wavelengths were unknown. The only hint of an excess was at 2.2 microns, where photometry at various positions (Becklin, private communication) had disagreed by factors of from two to four with rough predictions based on radio fluxes. Since the expected excess over recombination radiation was not large, what was needed was a method of measuring the excess that was more sensitive than the method of extrapolation from other wavelengths. In the spring of 1968, after discussing some of the possibilities with a fellow graduate student, Eric Becklin, it was decided that a measurement of the Brackett Gamma line of hydrogen at 2.16 microns would enable an accurate estimate of the expected recombination continuum, and thus of the excess. Accordingly, some time was spent in March of that year on the 24 inch telescope to determine if the line strength was of the calculated magnitude. The test was successful, and an observing program was subsequently worked out which is described in Chapter II. In Chapter II will also be found a description of the equipment, reduction methods, and data which were obtained. Chapter III makes use of a bonus of the line measurement, in that many of the physical properties of the gas in the nebula can be determined, some of them more accurately than has been previously possible. Chapter IV returns to the original purpose of the experiment. The demonstration of the infrared excess is somewhat redundant now that the huge excess has been established at the longer wavelengths. However, a 10 micron excess by no means implies an excess at, say, 1.65 microns. The distribution of the excess, both spatially and with wavelength, is analyzed in order to determine the most likely physical processes acting in the nebula. When this is done, the excess at 10 microns is shown to be caused by a different process than the unexpected excess at 1.65 microns.

II. EQUIPMENT, OBSERVATION, AND REDUCTION

A. Chapter Introduction

This chapter contains information on equipment, observations, and data reduction. The discussion starts with the two primary instruments: the spectrometer and the photometer, and continues with the detectors, the electronics, and the observations. The analysis is carried to the point of presenting a set of line intensities or continuum intensities as the case may be. These intensities will be used in later chapters to derive properties of the nebulae.

The effort involved in obtaining the spectra can be shown by comparison with other published infrared spectra. To date, only three papers have been published claiming to show infrared nebular emission lines. Paper one by Gillet et al. (ApJL 149, 97, 1967) contains step scanning observations of the planetary nebula NGC 7027. The 10.53 micron line of S^{+++} was seen on one night two standard deviations above the continuum, but was not seen on another night. The detection of the line must be considered questionable. Paper two by Gillet and Stein (ApJL 155, 97, 1969) contains step scanning observations of the planetary nebula IC 418. The 12.8 micron line of Ne^+ was observed to be nine standard deviations above the continuum and was seen on several nights. For unknown reasons, the flux in the line was fifteen times weaker than predicted by Delmer et al. (ApJ 149, 495, 1967), making a derivation of nebular properties from this measurement extremely questionable. Paper three by Westphal and

Neugebauer (ApJL 156, 45, 1969) reports observations of the Brackett Gamma line in Eta Carinae. Since the wavelength region is the same, this paper provides the most useful comparison. The higher order Brackett lines were not measured, and the specific intensity of Brackett Gamma is two orders of magnitude greater than the brightest measurement (S/N = 20/1) in the Orion Nebula!

Another point of illustration is that reliable observations were made of part of the Orion Nebula too faint even for visual spectroscopy.

Interferometer observations of cool stars by Johnson et al. (Comm LPL 7, 83, 1968) and by Low et al. (ApJ,to be published) appear to show the Brackett Gamma line in emission in some of the stars. The S/N appears to be at best 2/1 on the reported detection and needs further improvement.

From comparisons with existing spectra then, the present work represents a considerable improvement. In order to achieve this sensitivity, careful attention had to be paid to both the spectrometer design and the factors affecting the signal to noise (S/N) ratio in the data reduction. Techniques had to be developed for obtaining and adding spectra of such low S/N that neither the continuum nor the lines could be seen on the strip chart recording. More than half a million data points had to be reduced, a process which required some seven million arithmetic operations.

Broad band continuum intensities in the atmospheric windows of 1.25, 1.65, 2.2, 3.5, and 4.8 microns (J, H, K, L, M) were not as difficult to obtain as the spectra, so not as much space will be devoted to them in this chapter. A sufficient number of positions were measured to have made up crude maps in the various colors, but instead the data was degraded to agree with the spatial resolution of the spectra.

B. Spectrometer

The spectrometer used is basically the same one as described by McCammon et al. (ApJ 147 p. 575, 1967). The design is of the Ebert Fastie type with a 300 groove/mm grating of 10 cm. ruled length giving a dispersion of 65 Å/mm at 2.2 microns in the first order and 32 Å/mm at 1.6 microns in the second order. The order to be used is isolated with broad band interference filters.

The grating is driven in wavelength by a synchronous motor geared down to a micrometer screw. The gear arrangement used in this investigation provided a scan rate of 11.28 Å/sec at 2.2 microns in the first order and 5.10 Å/sec at 1.6 microns in the second order. This rate was found to be constant within the bands to at least the accuracy of measuring the position of a feature (20 Å and 10 Å respectively) and did not change over the observing period. This is important as it makes possible the use of a periodic data sampling technique, the relative time of sampling determining the relative wavelength by a linear relationship. By always starting the scanning and the sampling at a given wavelenth, a unique relationship is established which permits the addition of spectra. The success of this method can be seen upon examining the final summed spectra; in all cases the resolution is within 15 Å (plus noise) of that predicted.

The spectrometer was aligned for use at the f5.02 focus of the 60 inch telescope on Mt. Wilson. The basic modifications for use at this f ratio instead of the usual f16 were made by Dan McCammon, Gerry Neugebauer, and Ed Groth in an attempt to obtain an infrared spectrum of the galactic nucleus. As is well known, a smaller f ratio permits more flux at a given wavelength resolution from an extended object regardless of telescope aperture. The telescope aperture used at a given f ratio then determines the possible spatial resolution. For a discussion of this point, see Appendix 1. The 60 inch telescope proved nearly ideal in this respect, since the entire visual nebula could be observed with a reasonable number of observation points (five). Because the infrared flux from the night sky is large, it is necessary to subtract it out by looking alternately at the object and the sky nearby. The input chopping system is shown in Figure 1 to scale. The entrance apertures are 2 mm. slits instead of the circular apertures which had previously been used for stellar spectra. The front plate is aluminized so that light which does not pass through the two slits is reflected back into a guiding telescope. After passing through the lower (reference) slit, the light beam is reflected upward by the reference mirror where it is directed by the chopper mirror either into the spectrometer or into a reference monitor detector. Similarly light which passes through the upper slit is directed by the chopper mirror into either the spectrometer or the reference detector. Thus, as the chopper turns, the spectrometer sees light from each slit in turn. The reference detector is open to the entire 2.2 micron wavelength window and is used to monitor sky transparency changes such as might be caused by clouds. The chopping is done at 5 Hz.

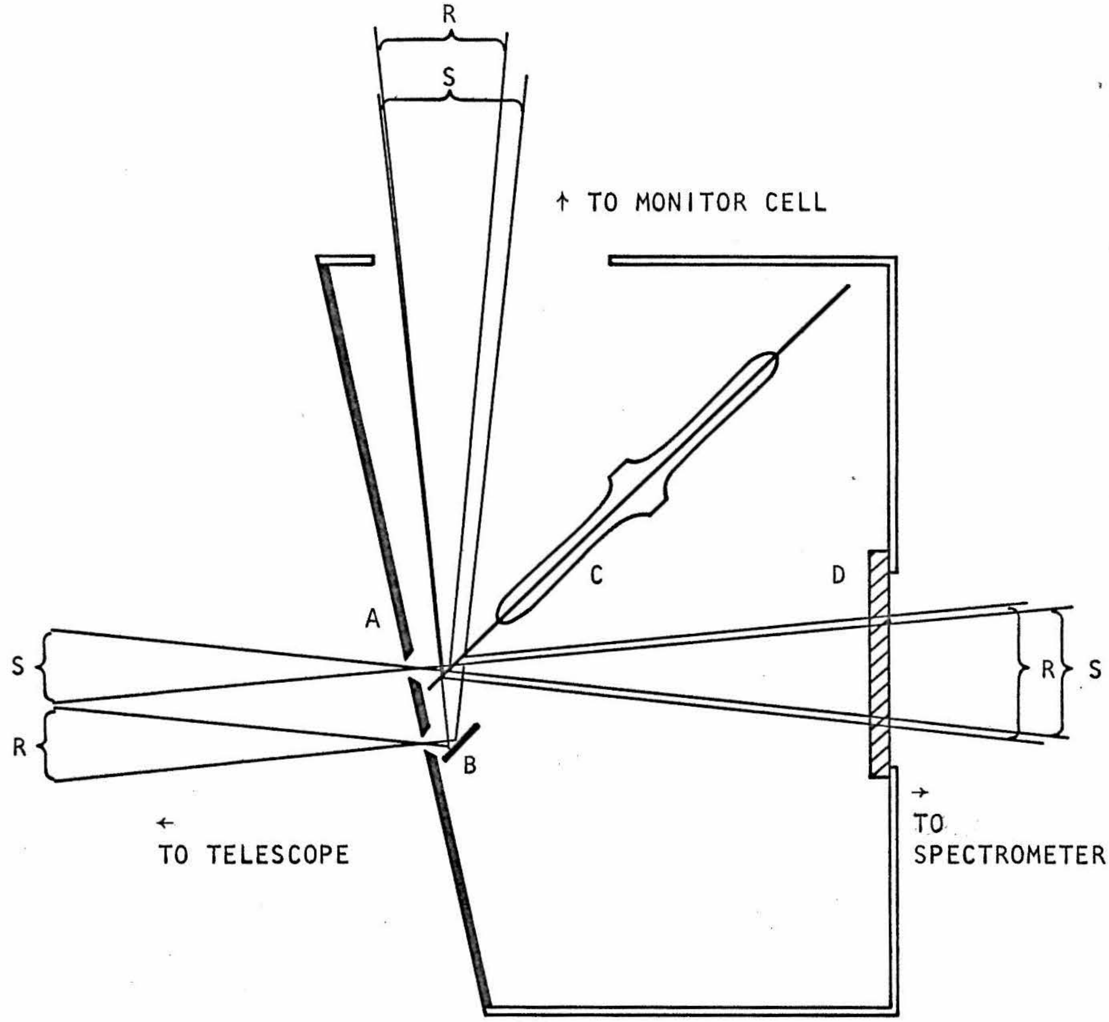

A - ALUMINIZED FRONT SURFACE APERTURE PLATE

B - ALUMINIZED FRONT SURFACE FLAT

C - ALUMINIZED BOTH SURFACE CHOPPER

D - ORDER SELECTION FILTER

FIGURE 1 F 5 INPUT CHOPPING UNIT FOR SPECTROMETER

At very low values of S/N, it is found that the two beams which are chopped do not quite cancel, so normally a second integration would be made with both beams on empty sky to get an effective zero. In the present experiment, however, the two slits are positioned close enough to one another that both beams are nearly in focus at the exit slit. Thus, instead of positioning the beams on empty sky for the second integration, the object may be placed in the lower beam. This results in a gain in S/N of about a factor of two, which means a gain of a factor of four in the amount of integration time. The slit spacing used (1 cm.) is a compromise between the requirements of wide spacing to get the reference beam off the object and narrow spacing to keep both beams almost in focus. As it turned out, the two outer regions of M 42 had to be done by a differential stepping technique which will be described later.

C. Photometer

The photometer used is basically as described by Becklin (Ph.D. Thesis, Caltech, 1968). Since some changes were made, however, a brief description will be given here.

The photometer accomplishes three basic functions: (1) selecting the wavelength to be observed, (2) chopping the field of view between the source and a nearby portion of the sky, and (3) guiding on the object.

The method of wavelength selection is by rotation of a wheel containing the various interference filters which define the wavelength bands. A selected filter can thus be brought into the optical path. The filters used for this experiment were the same as used by Becklin (Ph.D. Thesis, Caltech, 1968).

The chopping is done by means of a rapidly rotating aluminized sector wheel placed at 45 degrees to the incoming beam. This deflects the optical path by 90 degrees from the telescope optical axis. Near the sector wheel is a 45 degree mirror positioned so that when a vane of the sector wheel is not in the optical path, the detector looks out at a nearby portion of the sky. The distance of the flat from the sector wheel determines how close to each other the two alternating observation points are. Both beams cannot be in focus at the same time, but, for a reasonably close spacing on an extended object, this is not a serious problem. For this investigation, a spacing of 15 mm., corresponding to 315 arc seconds at the 24 inch telescope, was used. This is about the limit for maintaining a reasonable focus at f16 (½ mm. diameter blur circle) for 2 mm. diameter focal plane apertures. It was desired to keep the two beams in focus so that the source could be measured in each beam in turn. This produces a factor of two gain in the signal to noise ratio as was mentioned in the spectrometer discussion. The spacing, however, had to be at least this wide to keep the second beam off the nebula.

The chopping rate was also selected to optimize two opposing effects. First, it is generally desirable to chop as rapidly as possible to minimize the effect of sky fluctuations. Second, the cells have a finite time of response to the alternating light. For liquid nitrogen temperature, lead sulfide cells (used for 1 to 4 microns) respond well at frequencies around 5 Hz., while lead selenide cells (used for 4 to 6 microns) respond well to frequencies near 50 Hz. Since an important consideration in the photometry was to get color ratios at identical positions, both cells had to be used sequentially. Thus, a chopping frequency of 15 Hz. was used. Fifteen is also an exact even divisor of sixty, so that the possibility of any line voltage affecting the data is minimized.

Guiding was accomplished in two stages. First, the flip-in mirror system described by Becklin (Ph.D. Thesis, Cal Tech, 1968) was used to locate the position in the field. Then an offset guiding eyepiece was positioned on a convenient guide star and the flip-in mirror was removed. The guide star was moved between two previously determined positions on the guide reticle to move the source alternately into each beam. The flip-in mirror system could not be used for this since it did not always flip out to an identical position and the 5 micron detector's zero was somewhat sensitive to stray light on the lowest scales.

D. Detector Systems and Apertures

The detector used for the spectra was a liquid nitrogen cooled 0.5 mm. square lead sulfide photo resistor. This was preceded in the optical train by a cooled 3.2 mm. focal length coated silicon field lens which projected the f5 image of the primary onto a .64 mm. diameter circle. As discussed in Appendix 1, it was desirable to have a long slit, so the 6 mm. useable diameter of the field lens was allowed to set the slit length. Because of considerable astigmatism in the Ebert Fastie spectrometer optics when used at f5, and also because it was necessary to set the lens somewhat behind the focal plane, the half power points fell about 3.6 mm. apart or 98 arc seconds projected on the sky. With the slit width of 54 arc seconds, this gave an effective aperture of 1.26×10^{-7} ster. The plate scale of the 60 inch Newtonian focus was measured as 27.1"/mm. ±0.1, in agreement with the standard scale of 27.0"/mm. ±0.2. A cooled short pass filter to block out any radiation of wavelength longer than 2.6 microns was also used in front of the lens. Exposing the cell to the longer wavelengths results in a considerable increase in noise.

Two detectors were used for the photometry. For the wavelength bands J (1.25 microns), H (1.65 microns), K (2.2 microns), and L (3.5 microns) a liquid nitrogen cooled 0.5 mm. square lead sulfide photoresistor was used. For the band M (4.8 microns), a liquid nitrogen cooled 0.5 mm. square lead selenide photoresistor was used. Both cells were preceded by cooled 8 mm. focal length coated silicon field lenses. This gives a system f ratio of 16. The shorter wavelength cell was unfiltered except for the 1 micron cut-off of the silicon lens. The long wavelength cell had a cooled wide band filter of effective wavelength 4.8 microns preceding the lens. For the observations, room temperature focal plane diaphragms 2 mm. in diameter were used. This projected on 38.4 arc seconds on the sky for an aperture of 2.72×10^{-8} steradians. The plate scale for the 24 inch photometry (19.20"/mm. ±0.05) was determined assuming the N-S and E-W separation of θ_1^c and θ_2 Orionis to be 94.15 and 96.90 arc seconds respectively.

E. Electronics

The electronics used is now common in infrared observations, so only a brief description will be given. A block diagram is shown in Figures 2 and 3 for the set-ups used for the spectra and the photometry respectively. Before the magnetic tape unit was set up, and occasionally when it broke down, the integration unit was used to digitize the spectra. These two data units will be discussed later in this section.

Because of a large DC component caused by emission in the night sky, it is necessary to chop between the object and nearby sky. The amplifier is sensitive only to the alternating component of the signal so the sky is automatically subtracted out. In order to increase the signal to noise, a Dicke Switch type of demodulator is used on the amplified signal. The phase for the demodulator is determined by a light and photocell system which is triggered by the chopper blade.

A short time constant (0.5 sec. RC) is added before the signal goes to the chart recorder or data unit. For the chart recorder, this is a matter of convenience in viewing the signal. For the photometry (integration unit), the essential requirement is that the time constant be short enough, compared with the 10 second integration time used, that the effect of previous signals is small.

For the spectroscopy, the real signal is continually changing with time and the selection of the time constant is more critical.

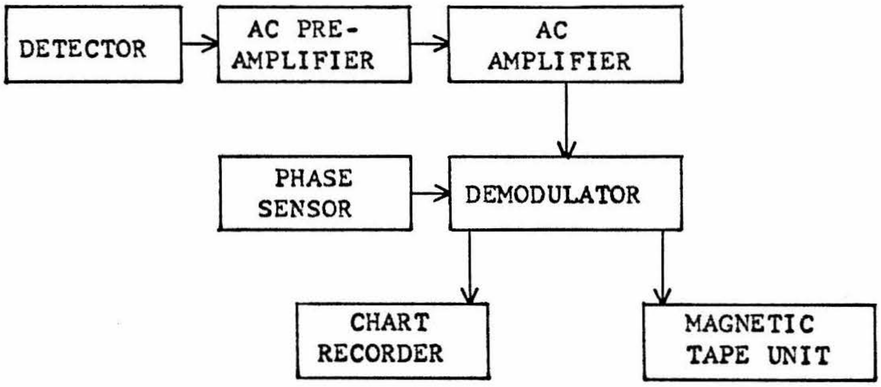

<u>FIGURE 2</u> SPECTROSCOPY ELECTRONICS

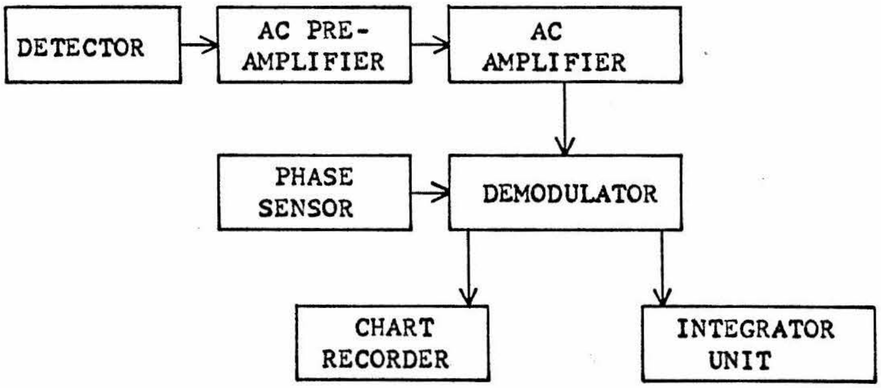

<u>FIGURE 3</u> PHOTOMETRY ELECTRONICS

The time constant is fixed by two requirements. First, to allow for possible sky variations, it was desired to complete single scans within ten minutes. Second, it was desired to have the time constant short with respect to the rise time of coming on the line. This permits an optimum weighting technique to be used in noise elimination as discussed in Appendix 2. Thus, for an exit slit of two millimeters and a scanning rate corresponding to 0.173 mm./sec., a time constant of 0.50 seconds "RC" (1.10 seconds "10 to 90") was chosen as short enough. A shorter time constant would also have worked, but the amount of data to be recorded would have increased without any increase in real information, i.e., no signal of interest had a high frequency component.

The integrator unit consisted of a voltage to frequency converter, a fixed time counter, and a paper printer. For the photometry, the counter integrated over ten second intervals. For the spectra, the integration time was one second. Including a dead time of 0.20 seconds necessary for printing, a data point was produced every 1.20 seconds. Because the voltage to frequency converter produced an ambiguity in ω in passing through zero, a voltage offset corresponding to ½ full scale was added to the signal before conversion. The strip chart recorder was also zeroed at half scale so that, as long as the signal did not go off on the strip chart, the voltage to frequency converter worked properly. Since a 0.5 second time constant was added before these two data units, their different speeds of response were not a consideration.

When using the integrator unit for scanning spectra, the 0.5 second time constant allowed a partial forgetting of the previous one second of signal during the 0.2 second dead time while preserving information about what occurred during the dead time for the next one second integration. This slight interdependence of successive points was not serious since it took twenty seconds to go over a feature anyway. A more serious limitation in the use of the integrator unit was that it was not computer compatible. Converting a night's data to cards generally took an experienced keypunch operator a full day.

The magnetic tape unit consisted of an analog to digital voltage converter, a time of day clock, a set of indicator switches, a multiplexer to switch in pre-programmed sequence between the voltage, time, and indicator switch information, and a tape handling unit. Since the information was recorded digitally, it could be read directly by computer.

Samples of the signal are taken by the MTU over a very short interval (about 1 millisecond) with the time between samples being a constant, but adjustable, quantity. The question of a proper time constant can be answered by the sampling theorem of information theory (e.g., see Papoulis, "The Fourier Integral and Its Applications" 1962, p.50). For a band limited signal described by $\Delta\omega$, sampling twice within a time interval corresponding to $2\pi/\Delta\omega$ obtains all the information available in that time interval. A system described by a time constant is not truly band limited, but for the present argument this should be an adequate approximation. With the 0.50 second "RC" time constant (1.10 seconds "10 to 90") fixed by other considerations, a sampling rate of once every 0.30 seconds was used for the spectra. This introduced a further data reduction simplification in that if four such points were averaged, the data could be combined with data from the integrator unit (every 1.20 seconds) without registration problems. The registration was found perfect over a full scan of ten minutes.

F. The Spectrometer Observations

The spectral observations were made on the 60 inch and 100 inch telescopes at Mt. Wilson. Table 1 gives the customary statistics. For brevity, standards are not listed, and the list is also restricted to those nights which were used.

The wavelength bands covered turned out to have the property that strong lines are very strong and weak lines are not seen. Thus, once the equivalent widths of the few strong lines have been measured, the spectra show very little additional information. For this reason, and because of the large number of spectra obtained, only sample spectra will be presented.

It is of more interest to show a sample spectrum at various stages of processing. For this purpose, 2 micron observations of the region 50 arcseconds south of the Trapezium on 14 October 1968 have been selected as being representative. Figure 4 shows a segment from the strip chart obtained that night. For the signal tracing, approximate values of the zero have been indicated at either side of the chart segment. Normally it is unnecessary to know the zero (which does change with wavelength) since a companion tracing is taken with the source in the other aperture. Because of the 180 degree phase difference in the chopping, this produces a deflection in the opposite direction. It is the difference of these two signals which ultimately is used. Also indicated is the wavelength of the Brackett Gamma line. Increasing wavelength is to the right. The sky monitor tracing is

TABLE 1

SUMMARY OF SPECTRAL OBSERVATIONS

Date	Telescope	Focus	Object	Region Covered*	λ Range (μ)	No. Scans	SecZ
4 Oct 68	100 inch	Cass.	NGC 7027	All	2.114-2.217	12	1.04
5 Oct 68	100 inch	Cass.	NGC 7027	All	2.118-2.219	12	1.01
14 Oct 68	60 inch	Newt.	M 42	50'' SOT	2.129-2.368	8	1.32
			M 42	Dark Bay	''	4	1.30
			M 42	Trap	''	4	1.30
15 Oct 68	60 inch	Newt.	M 42	Trap	2.128-2.353	4	1.64
			M 42	50'' NOT	''	4	1.54
			M 42	50'' SOT	''	4	1.46
			M 42	135'' NOT	''	16	1.36
			M 42	135'' SOT	''		
			M 42	Dark Bay	''	4	1.30
16 Oct 68	60 inch	Newt.	M 42	Trap	1.552-1.771	8	1.48

[continued on next page]

TABLE 1 (Continued)

Date	Telescope	Focus	Object	Region Covered*	λ Range (μ)	No. Scans	SecZ
16 Oct 68	60 inch	Newt.	M 42	50'' NOT	1.552-1.771	8	1.33
			M 42	50'' SOT	"	8	1.32
28 Nov 68	60 inch	Newt.	M 42	Trap	1.561-1.769	8	1.87, 1.32
			M 42	50'' NOT	"	8	1.62, 1.49
			M 42	50'' SOT	"	8	1.39, 1.66
30 Nov 68	60 inch	Newt.	M 42	Trap	1.585-1.707	4	1.58
			M 42	50'' NOT	"	16	1.49, 1.33
			M 42	50'' SOT	"	16	1.38
1 Dec 68	60 inch	Newt.	M 42	Trap	1.588-1.710	4	1.55
			M 42	50'' SOT	"	8	1.42, 1.35
			M 42	50'' NOT	"	4	1.40
2 Feb 69	60 inch	Newt.	IC 418	All	2.110-2.219	48	1.48-1.82
			M 42	Trap	"	4	1.65
1 Mar 69	60 inch	Cass.	IC 418	All	2.106-2.240	44	1.47-1.75

* SOT = South of Trapezium, NOT = North of Trapezium, Trap = Trapezium

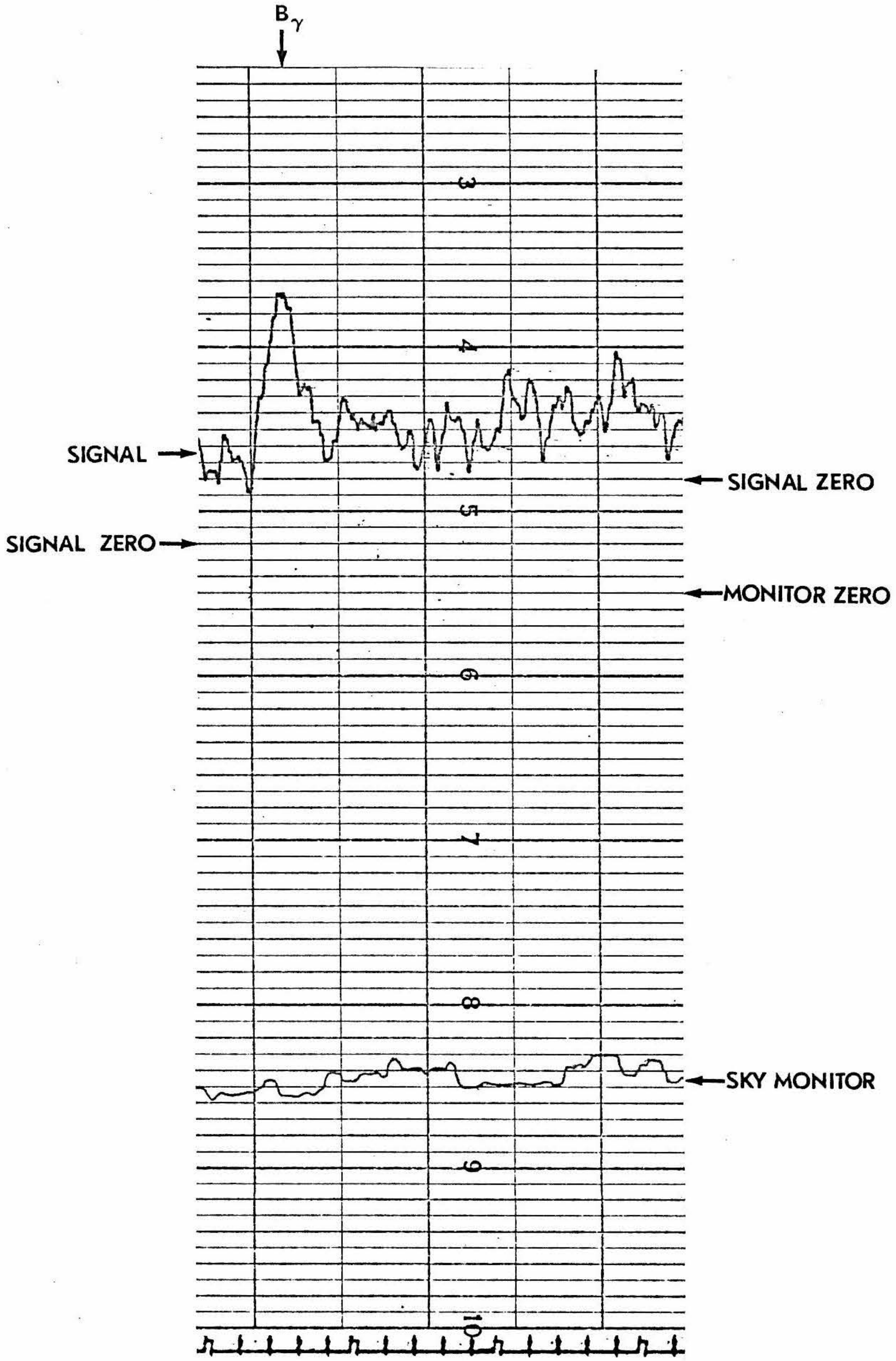

FIGURE 4 RAW DATA SAMPLE

run with a 180 degree phase reversal (positive deflection downwards) so that the two tracings do not interfere with one another. The changes in the sky monitor tracing are all cell noise, so that, in practice, quality of a single scan could only be assured to five or ten percent. This is not serious because many scans are added and small occasional transparency changes should thus have little effect.

Figure 5 shows the result of adding together the eight scans obtained that night. The deflection is in arbitrary units. The predicted triangular shape of the tracing over Brackett gamma can now be easily confirmed.

Figure 6 shows the result of correcting for sky and spectrometer wavelength response. The response is obtained by dividing a model stellar atmosphere for an AOV star by a scan of the star Alpha Lyra. An absolute flux can then be obtained at each wavelength by assuming the flux calibration at 2.2 microns is as given by Becklin (PhD. Thesis, Caltech, 1968).

Figure 7 shows the same scan after noise elimination by the convolution technique discussed in Appendix 2. This is the final form of the spectrum which could then be measured for the strength of the Brackett Gamma line (2.165 microns), for the strength of the nearby continuum, and for the amount of the continuum discontinuity at the limit of the Pfund series (2.28 microns).

In addition to providing a flux calibration, the standards also allow a check on the performance of the total system by providing a known spectrum to be reduced.

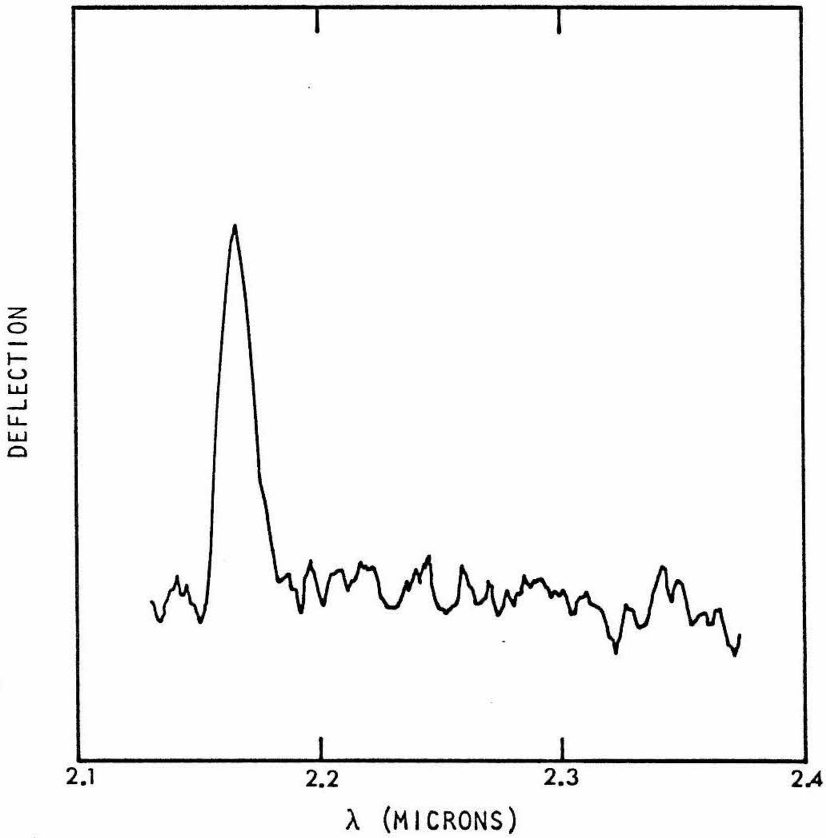

FIGURE 5 STAGES OF PROCESSING SPECTRA

1. 8 SCANS SUMMED

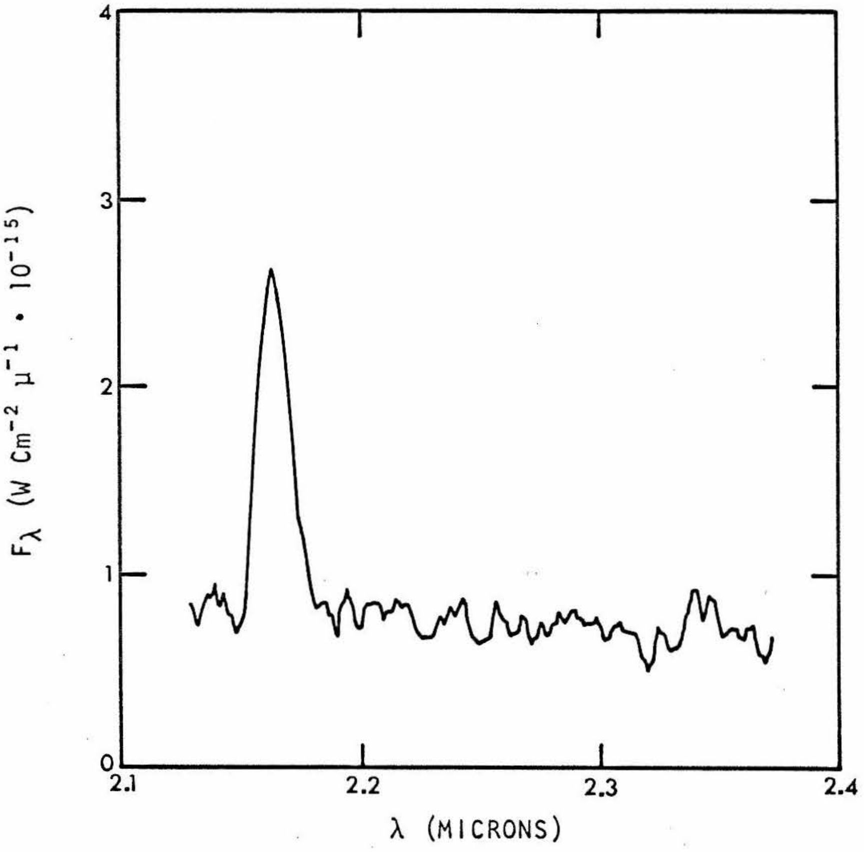

FIGURE 6 STAGES OF PROCESSING SPECTRA

II. ATMOSPHERE CORRECTED AND FLUX CALIBRATED

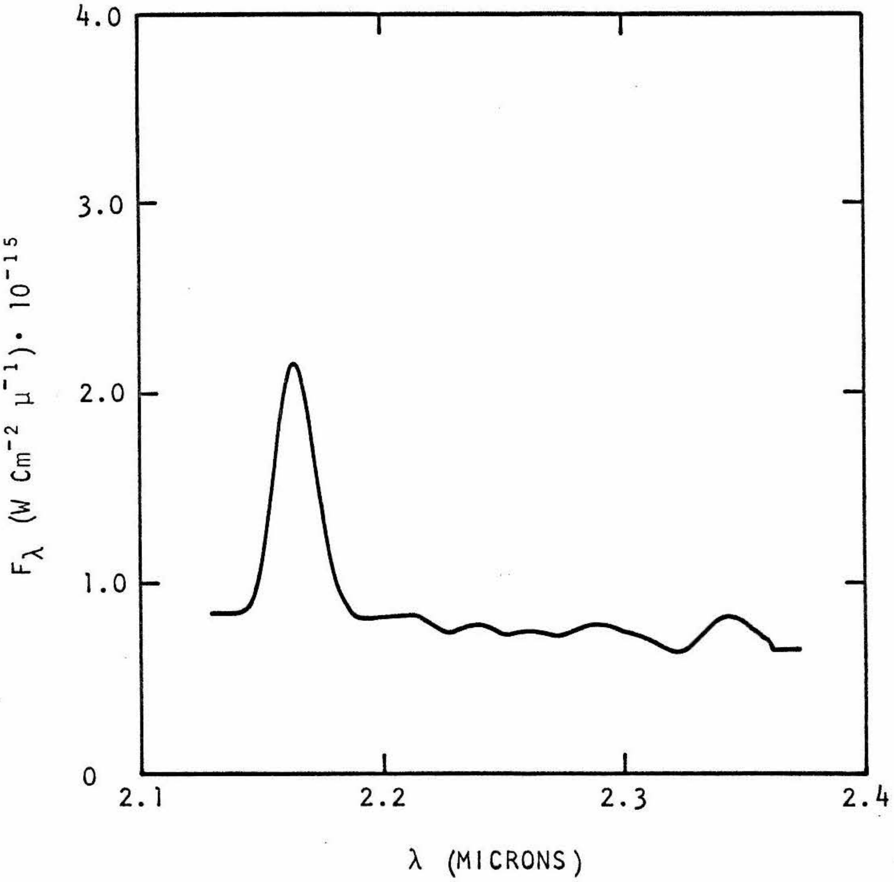

FIGURE 7 STAGES OF PROCESSING SPECTRA

III. SMOOTHED

Figures 8, 9, and 10 show convolved spectra of Alpha Lyra (0.03 K magnitude, AOV), Alpha Leo (1.62 K magnitude, B7V) and BS 8641 (4.75 K magnitude, A1V). For reference, the continuum deflection on the region 50 arcseconds south of the Trapezium corresponded to a K magnitude of 4.4. Figure 10, while quite noisy, indicates that there are no significant systematic problems, even at fainter magnitudes, than were measured for M 42. The deflections at 2.2 microns can be compared with the measured broad band fluxes with the result that the linearity of the spectrometer system corresponds to that of the broad band system to at least 10% over the range considered.

The Brackett Gamma line is in absorption in the three stars shown. For Alpha Lyra, the equivalent width is measured as 12.9 ± 1Å. This is in agreement with Hyland and Butcher's measurement of 13.2 ±1Å, using the same spectrometer at f16 (Hardorp & Scholz, Z Ap <u>69</u>, 350, 1968). The equivalent width predicted from model atmospheres varies from 10.3Å to 13.2Å, depending on choice of model and type of broadening used (Hardorp & Scholz Z Ap <u>69</u>, 350, 1968), so the agreement can be said good to about 15%. This would indicate that the slit profile does not have any significant wide shallow wings. To determine this is important since the measurement of the line strength could be in error by a significant amount if there were wings.

Another check was made on the telescope by measuring a star with and without a narrow band interference filter placed before the spectrometer entrance aperture. By this method it was determined

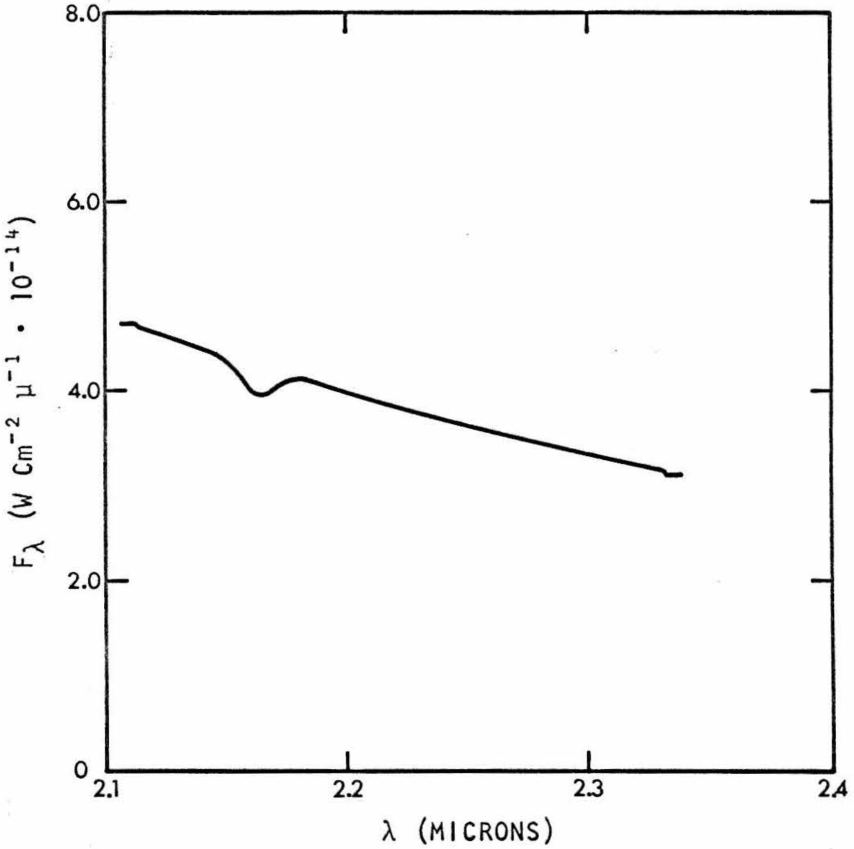

FIGURE 8 SPECTRUM OF ALPHA LYRA

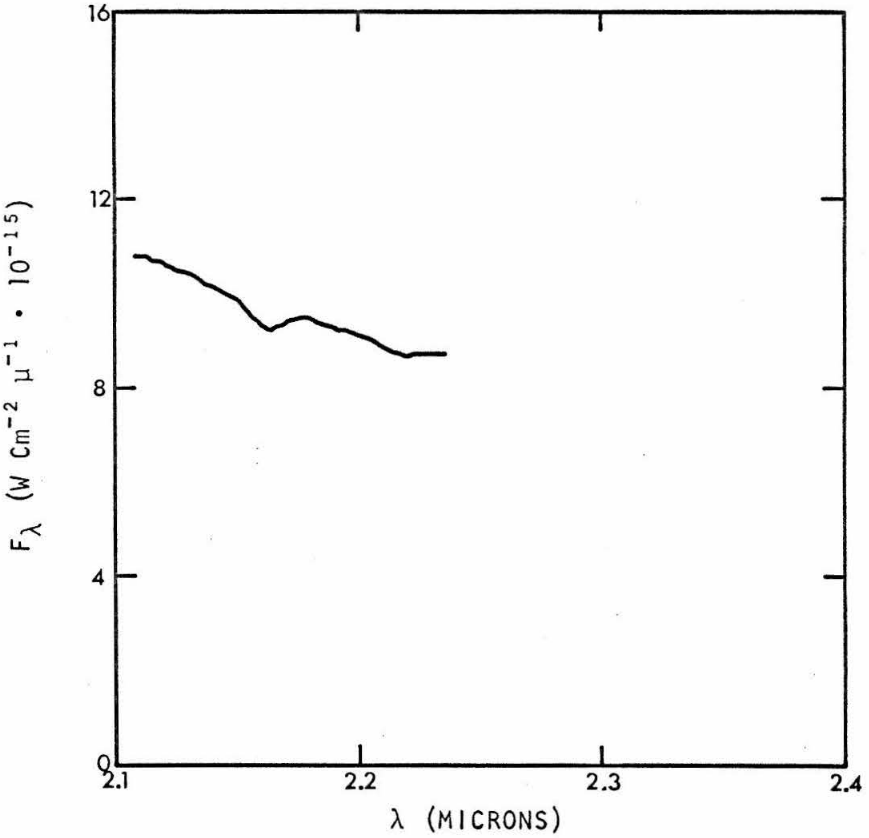

FIGURE 9 SPECTRUM OF ALPHA LEO

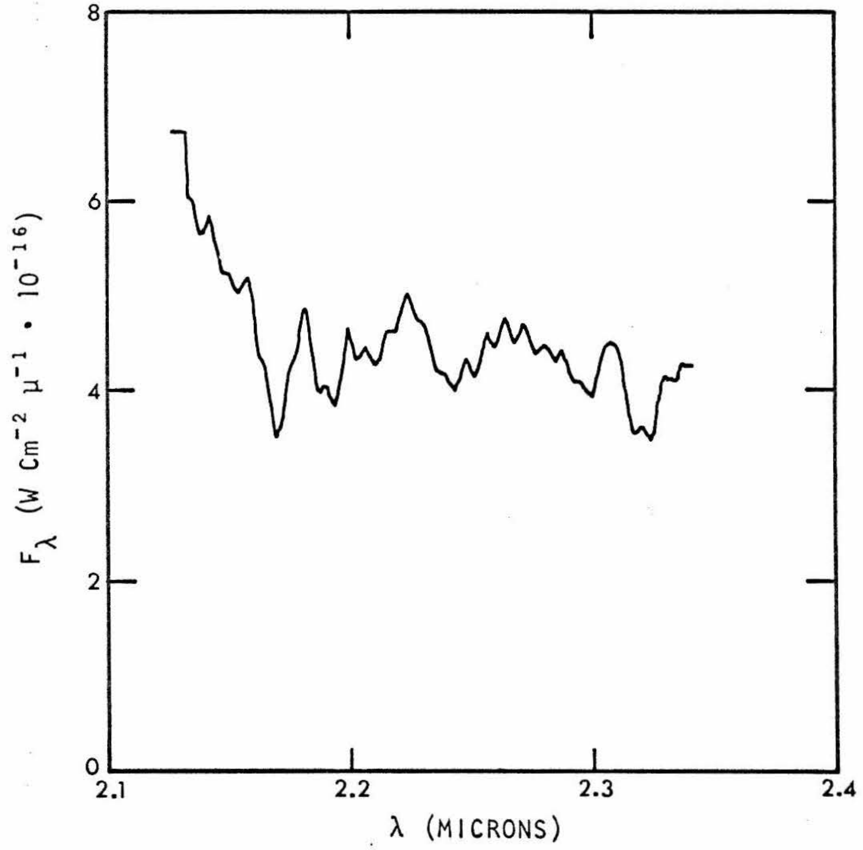

FIGURE 10 SPECTRUM OF B.S. 8641

that the energy outside the theoretical slit profile was of the order of 5% or less.

In order to take double beam data further than 1' north or south of the Trapezium, a special technique had to be employed. Figure 11 shows schematically the four observations which were taken. The Trapezium is represented by a black star, and the spectrometer focal plane apertures by S and R. If the measured deflection at each position i is given by M_i; the flux at positions 410" south is zero, 135" south is I_s, 135" north is I_n, and 410" north is zero; and the response of aperture S is taken as 1.0 and of aperture R is taken as R, then the following set of equations hold:

$$
\begin{aligned}
M_1(\lambda) &= I_S(\lambda) + C(\lambda) \\
M_2(\lambda) &= -R\, I_S(\lambda) + I_N(\lambda) + C(\lambda) \\
M_3(\lambda) &= -R\, I_N(\lambda) + C(\lambda) \\
M_4(\lambda) &= C(\lambda)
\end{aligned}
\tag{1}
$$

where C(λ) represents the lack of cancellation of sky emission between the two beams and also the constant electronics zero. Eliminating C(λ),

$$
\begin{aligned}
F_1(\lambda) &= M_1(\lambda) - M_4(\lambda) = I_S(\lambda) \\
F_2(\lambda) &= M_2(\lambda) - M_4(\lambda) = -R\, I_S(\lambda) + I_N(\lambda) \\
F_3(\lambda) &= M_3(\lambda) - M_4(\lambda) = -R\, I_N(\lambda)
\end{aligned}
\tag{2}
$$

The quantities to be calculated are $(\frac{1+R}{2}) * I_s$ and $\frac{1+R}{2} * I_n$. If R is known from other measurements, then there are more equations

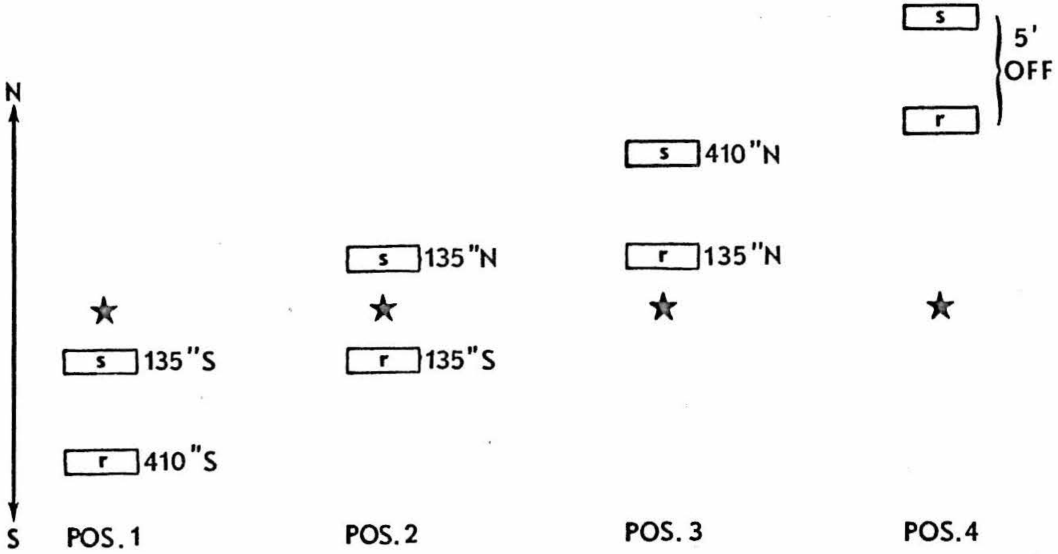

FIGURE 11 POSITIONS FOR DOUBLE STEPPING SPECTROSCOPY

than unknowns. The solution, when proper weighting is given for noise, is

$$\left(\frac{1+R}{2}\right) I_S(\lambda) = \left[F_1(\lambda)\frac{\sqrt{2}}{1+\sqrt{2}} - \frac{1}{R}\left(F_2(\lambda) + \frac{F_3(\lambda)}{R}\right)\frac{1}{1+\sqrt{2}}\right]\frac{1+R}{2}$$

(3)

$$\left(\frac{1+R}{2}\right) I_N(\lambda) = \left[-\frac{F_3(\lambda)}{R}\frac{\sqrt{2}}{1+\sqrt{2}} + \left(F_2(\lambda) + R\,F_1(\lambda)\right)\frac{1}{1+\sqrt{2}}\right]\frac{1+R}{2}$$

These equations then were used to obtain the spectra from 135 arc-seconds north and south of the Trapezium.

Table 2 summarizes the line and continuum intensity measurements at various positiona and wavelengths. Where relevant, the numbers are corrected for the flux from the stars in the beam.

TABLE 2

SUMMARY OF SPECTRAL DATA

			Equivalent Width (Å)		I_ν (W M^{-2} Hz^{-1} $Ster^{-1}$)*		I_{LINE}
Object	Position	λ (μ)	Raw	Corrected For Stars	Raw	Corrected For Stars	(W M^{-2} $Ster^{-1}$)*
M 42	Dark Bay	2.31			2.2±1.5 x 10^{-19}		
		2.52			3.0±1.5		
		2.166 B_7	416 ±100		2.8±1.5		6.9±1.0 x 10^{-7}
M 42	135'' NOT	2.31			5.2±2.0		
		2.52			4.9±2.0		
		2.166 B_7	282 ± 90		4.7±2.0		8.4±1.6
M 42	50'' NOT	2.31			20 ±2	15 ±2	
		2.52			19 ±2	15 ±2	
		2.166 B_7	160 ±68	190±80	18 ±2	15 ±2	18 ±3
		1.736 B_{10}	59 ±15	60±15	8.6±1	8.5±1	5.1±2.0
		1.681 B_{11}	46 ± 9	46± 9	8.8±1	8.7±1	4.3±1.3

[continued on next page]

TABLE 2 (Continued)

			Equivalent Width (Å)		I_ν (W M^{-2} Hz^{-1} $Ster^{-1}$)*		I_{LINE}
Object	Position	λ (μ)	Raw	Corrected For Stars	Raw	Corrected For Stars	(W M^{-2} $Ster^{-1}$)*
M 42	50" NOT	1.641 B_{12}	43 ± 9	43± 9	8.1±1 x 10^{-19}	8.0±1	3.9±1.2 x 10^{-7}
		1.611 B_{13}	43 ± 9	43± 9	7.6±1	7.6±1	3.8±1.1
		1.588 B_{14}	41 ±10	41±10	6.2±1	6.1±1	3.0±1.2
		1.700 H_e	25 ± 6	26± 6	7.7±1	7.6±1	2.0±0.8
M 42	Trapezium	2.31			31 ±1	22 ±1	
		2.52			32 ±1	23 ±1	
		2.166 B_7	162 ± 9	231±19	33 ±1	23 ±1	34 ±5
		1.736 B_{10}	28 ± 7	47±12	32 ±1	20 ±1	9.1±3.6
		1.681 B_{11}	26 ± 5	46± 9	31 ±1	18 ±1	8.6±2.6
		1.641 B_{12}	20 ± 4	35± 7	32 ±1	18 ±1	7.0±2.1
		1.611 B_{13}	18 ± 4	31± 6	33 ±1	19 ±1	6.8±2.0
		1.588 B_{14}	9.8± 2.4	18± 4	32 ±1	18 ±1	3.7±1.5

[continued on next page]

TABLE 2 (Continued)

			Equivalent Width (Å)		I_ν (W M^{-2} Hz^{-1} $Ster^{-1}$)*		I_{LINE}
Object	Position	λ (μ)	Raw	Corrected For Stars	Raw	Corrected For Stars	(W M^{-2} $Ster^{-1}$)*
M 42	Trapezium	1.700 H_e	12 ± 3	20± 5	32 ±1 x 10^{-19}	20 ±1	4.0±1.6 x 10^{-7}
M 42	50'' SOT	2.31			11 ±1		
		2.52			10 ±1		
		2.166 B_7	344 ±40		11 ±1		23 ±4
		1.736 B_{10}	66 ±16		9.3±1		6.1±2.4
		1.681 B_{11}	62 ±12		7.1±1		4.6±1.4
		1.641 B_{12}	44 ± 9		8.8±1		4.3±1.3
		1.611 B_{13}	37 ± 7		6.9±1		2.9±0.9
		1.588 B_{14}	22 ± 6		6.2±1		1.6±0.7
		1.700 H_e	29 ± 7		7.2±1		2.2±0.9
M 42	135'' SOT	2.31			4.4±2		
		2.52			2.8±2		

[continued on next page]

TABLE 2 (Continued)

Object	Position	λ (μ)	Equivalent Width (Å)		I_ν ($W\ M^{-2}\ Hz^{-1}\ Ster^{-1}$)*		I_{LINE}
			Raw	Corrected For Stars	Raw	Corrected For Stars	($W\ M^{-2}\ Ster^{-1}$)*
M 42	135'' SOT	2.166 B_7	544 ±120		$3.1 \pm 2 \times 10^{-19}$		$10.7 \pm 2.0 \times 10^{-7}$
NGC 7027	All	2.166 B_7	306 ± 40		$1.6 \pm 0.2 \times 10^{-26}$		$3.1 \pm 0.3 \times 10^{-14}$
		2.184 H_e?	71 ± 20		1.8±0.2		0.8±0.2
IC 418	All	2.166 B_7	204 ± 90		1.2±0.4		1.4±0.5

* Assuming $\Omega = 1.26 \times 10^{-7}$ ster. for planetaries, F_ν and F_{LINE} are given instead.

G. The Photometer Observations

The photometry was done on the 24 inch telescope at Mt. Wilson. Table 3 gives the customary statistics. The regions referred to are shown in Figure 12. Before the small regions were added together to approximate the spectrometer field, corrections were made for atmospheric extinction and known stars in the aperture. Table 4 gives the fluxes adopted for the Trapezium, for the Becklin-Neugebauer Object ORS-1 (ApJ 147, 799, 1967), and for a second red star, ORS-2, 10 arcseconds north of ORS-1. Thus, the averaged measurements given in Table 5 represent a best approximation to the nebular emission only. The names ORS-1 and ORS-2 (for Orion Red Star) are proposed here to avoid confusion.

All regions were weighted equally in the average rather than by estimated error. While the field is not precisely identical to that of the spectrometer, the data have the more important feature that the fluxes at various wavelengths can be directly compared. That is, the full set of bands were taken the same night, with the same aperture, and at the same position in the nebula.

Previously existing measurements in the infrared represent a hodgepodge of apertures and positions which have presented a serious limitation to a careful analysis of the nebular properties.

TABLE 3

SUMMARY OF PHOTOMETRY

Date	Region	No. of 10 Sec. Integrations 1.25μ	 1.65μ	 2.2μ	 3.5μ	 4.8μ	SecZ
18 Nov 1968	4	20	20	20	20	20	1.3
	7	20	20	20	20	40	1.3
	17	20	20	20	20	40	1.5
19 Nov 1968	3	16	16	16	16	16	1.3
	10	16	16	16	16	24	1.3
	11	16	0	0	16	24	1.5
	13	16	16	16	16	24	1.7
20 Nov 1968	2	16	16	16	16	16	1.4
	10	16	16	16	16	16	1.5
	12	16	16	16	16	16	1.6
	4	16	16	16	16	16	1.9
21 Nov 1968	4	8	8	8	8	8	1.4
	12	8	8	8	8	16	1.9
30 Dec 1968	7	8	8	8	8	12	1.4
	9	8	8	8	8	0	1.6
1 Jan 1969	7	8	8	8	8	16	1.4
	6	8	8	8	8	12	1.3

[continued on next page]

TABLE 3 (Continued)

Date	Region	No. of 10 Sec. Integrations 1.25μ	1.65μ	2.2μ	3.5μ	4.8μ	SecZ
1 Jan 1969	8	8	8	8	8	12	1.3
	15	8	8	8	8	12	1.3
	14	8	8	8	8	16	1.4
	16	8	8	8	8	16	1.4
	5	8	8	8	8	12	1.5
	1	8	8	8	8	12	1.7

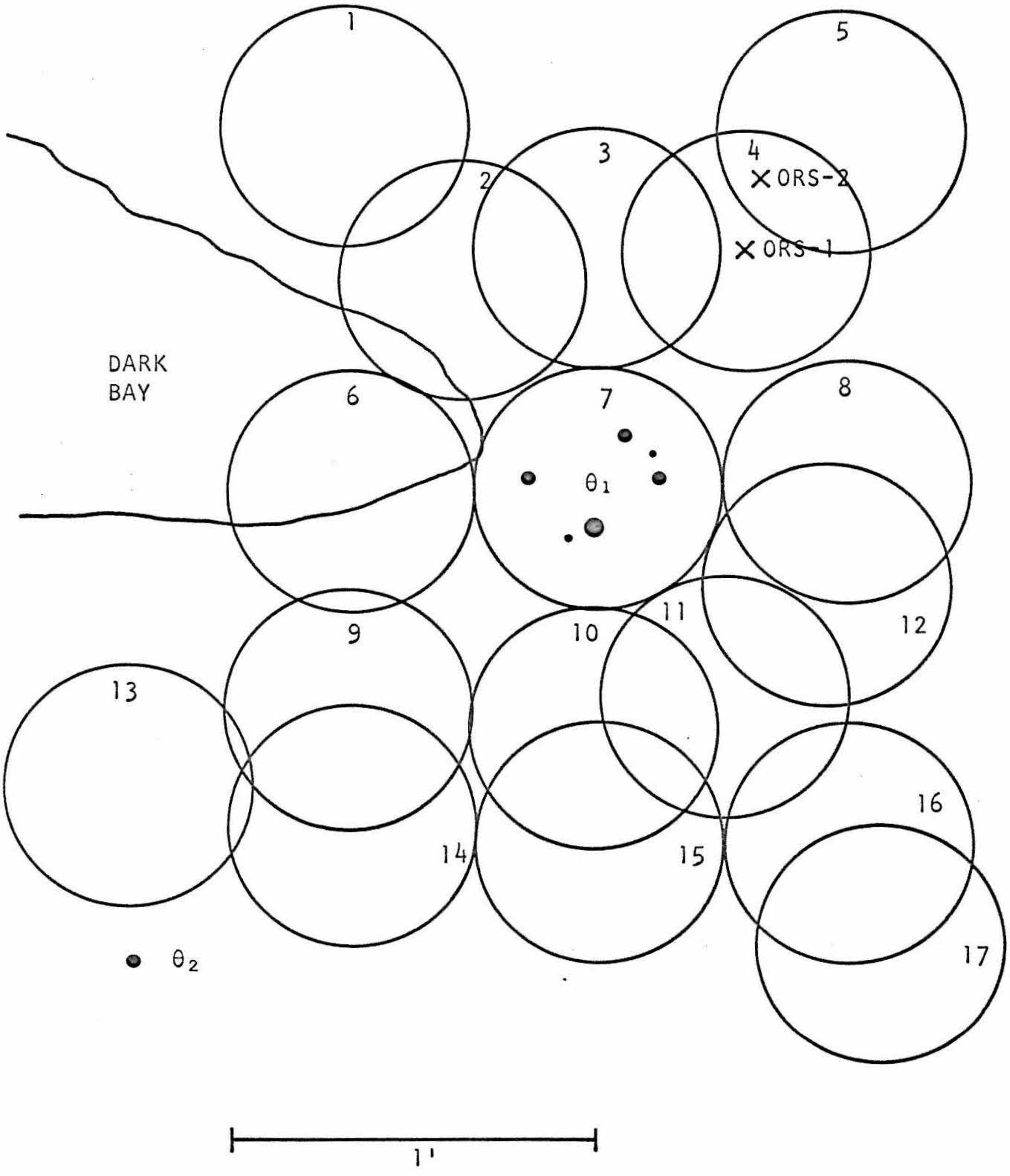

FIGURE 12 PHOTOMETRY REGIONS

TABLE 4

ADOPTED STELLAR FLUXES

Adopted Fluxes F_ν (W M^{-2} Hz^{-1})

	$1.22\mu^{-1}$	$1.00\mu^{-1}$	$.800\mu^{-1}$	$.606\mu^{-1}$	$.454\mu^{-1}$	$.286\mu^{-1}$	$.208\mu^{-1}$	$.099\mu^{-1}$	$.051\mu^{-1}$
Object	0.82μ	1.0 μ	1.25 μ	1.65 μ	2.2 μ	3.5 μ	4.8 μ	10.1 μ	19.5 μ
ORS-1				0.13×10^{-26}	5.5	56.	150.	120.	30.
ORS-2				0.29	1.4	5.1			
Trap	34.	27.	21.	17.	12.	7.4	4.9	3.6	

Adopted Fluxes F_λ (W Cm^{-2} μ^{-1})

Object	0.82μ	1.0 μ	1.25 μ	1.65 μ	2.2 μ	3.5 μ	4.8 μ	10.1 μ	19.5 μ
ORS-1				1.4×10^{-17}	34.	139.	197.	34.	2.3
ORS-2				3.2	8.6	12.6			
Trap	1500.	800.	404.	188.	74.	18.3	6.4	1.0	

TABLE 5

SUMS OF SMALL REGIONS FOR COMPARISON WITH SPECTROMETER DATA

Spectrometer Region	Regions Averaged	I_ν (W M^{-2} Hz^{-1} $Ster^{-1}$) · 10^{19}				
		1.25μ	1.65μ	2.2μ	3.5μ	4.8μ
50'' NOT	1, 2, 3, 4, 5	15.1±3.0	12.9±2.6	24.4±4.9	93 ±19	299±90
Trapezium	6, 7, 8, 12	35.6±3.6	21.2±2.1	20.4±2.0	43.5± 4.4	139±21
50'' SOT	9, 10, 11, 13, 14, 15, 16	17.1±3.4	10.4±2.1	11.1±2.2	14.4± 2.9	37±11

III. SPECTRAL LINE ANALYSIS (B_7, B_{10}-$_{14}$, He) FOR M 42, NGC 7027, AND IC 418

A. Chapter Introduction

This chapter contains primarily those analyses of the spectral data which yield information determinable by other means. By comparing the values here obtained for electron temperature, electron density, reddening, and helium abundance with those of other authors, one can get a feeling for the reliability of the data.

A considerable amount of material has been published on the Orion Nebula, and, as will be seen, much of it is contradictory. In order to make some sense out of the available material, it has been analyzed from the point of view of a model which fits the properties determined by the infrared spectra. Thus, outside data which agree tend not to be criticized too heavily, while every attempt is made to explain away unsatisfactory outside data within the limitations of the model. It is left to the reader to judge whether this has been done successfully. Note that since the model properties discussed here can be determined only by using outside data, a distinction must be made between outside data which gives "direct" measurements, such as line intensities, and outside data which gives "derived" measurements, such as temperature. Outside "direct" measurements are combined with the infrared "direct" measurements to give "derived" infrared measurements which can be compared with other "derived" outside measurements.

In order to orient the chapter, the results will be summarized in advance. This chapter largely ignores dust emission, which is considered in the next chapter. This separation is possible since only the lines are considered here and since neither the visual nor the radio data shows effects of the dust emission. Note that it is necessary to make a distinction between emission and scattering.

The basic parameters determined in this paper for the ionized region are (1) an average electron temperature between eight and nine thousand degrees; (2) a slight increase of electron temperature with distance from the Trapezium out to about 2' or 3' from the center followed by a decrease at greater distances; (3) an average electron density of about 2 x 10^3 electrons/cm^3 near the Trapezium; (4) a flat electron density with distance from the Trapezium for the central 3' followed by a decrease at greater distances; (5) an average visual reddening of about one magnitude; and (6) a helium abundance of about ten percent. This is a somewhat different picture of the nebula than is usually assumed. It should be emphasized that not all the properties have been equally well proven, but, nevertheless, all have been adopted as a framework within which outside data can be examined.

For comparison, externally determined parameters of the nebula would be (1) an electron temperature which ranges from 13,000°K to 1200°K, depending on what data are believed; (2) no change in temperature of a slight decrease with distance from the Trapezium; (3) an average electron density of about 2 x 10^3 electrons/cm^3 near the Trapezium; (4) a rapidly decreasing electron density with distance from the Trapezium; (5) a visual reddening of either one or two magnitudes; and (6) a helium abundance of 15 to 20 percent. *Appropriate* papers which suggest these other parameters are discussed following each determination of one of the infrared "derived" properties.

The planetary nebula data were taken primarily for comparison with M 42. It is felt that the planetaries provide an experimental check on the value of the M 42 data which is somewhat independent of theoretical considerations.

B. Theoretical Background

Following Menzel's (ApJ, 1937, p. 330) classic derivation, one arrives at expressions for the bound-bound, bound-free, and free-free emission in the nebula for hydrogenic atoms

$$(1)\quad E_{nn'} = N_i N_e \frac{KZ^4}{T_e^{3/2}} \frac{b_n g_{nn'}}{n'^3} \frac{2hRcZ^2}{n^3} e^{\frac{hRZ^2}{n^2 kT_e}} \quad \mathrm{ERG\ CM^{-3}\,SEC^{-1}}$$

$$(2)\quad E_{\nu_\kappa n'} = N_i N_e \frac{KZ^4}{T_e^{3/2}} \frac{g_{b.f.}}{n'^3} \quad h \quad e^{-\frac{h(\nu-\nu_{n'})}{kT_e}} \quad \mathrm{ERG\ CM^{-3}\,SEC^{-1}\,Hz^{-1}}$$

$$(3)\quad E_\kappa = N_i N_e \frac{KZ^4}{T_e^{1/2}} g_{f.f.} \frac{k}{2hRcZ^2} \quad e^{-\frac{h\nu}{kT_e}} \quad \mathrm{ERG\ CM^{-3}\,SEC^{-1}\,Hz^{-1}}$$

where n is the upper level, n' is the lower level, N_i is the number density of ions, N_e is the number density of electrons, K is a grouping of atomic constants ($K = 3.260 \times 10^{-6}$ erg$^{3/2}$ sec cm ^{o}K$^{3/2}$ gm$^{-3/2}$) Z is atomic charge, T_e is a representative electron temperature, b_n is a ratio number giving the departure from the thermodynamic equilibrium of the upper level, g is the Gaunt factor, h is Planck's constant, R is the Rydberg constant, c is the velocity of light, k is Boltzman's constant, ν is the frequency of the emitted light, and $\nu_{n'}$ is the minimum frequency of light needed to ionize from level n'.

Following Aller (Gaseous Nebulae, p. 151, 1957) one arrives at the expression for the two quantum emission in the nebula

$$(4)\quad E_{2\gamma} = N_i N_e \frac{KhZ^4}{T_e^{3/2}} \, y\,\phi_1(y) \frac{2x}{3.77} \quad \frac{\phi_2(\beta)}{\beta}$$

where y is defined by $\nu = y * \nu(2S - 1S)$, $y \leq 1$

β is defined by $\beta = \frac{hRcZ^2}{kT_e}$

X is the fraction of all recombinations to level n = 2 and higher which eventually reach the 2S state. ϕ_1(y) is tabulated in Aller (loc cit) and is proportional to the 2S-1S (two quantum) transition probability as a function of the "normalized" frequency y. $\phi_2(\beta)$ is also tabulated in Aller (loc cit) and is proportional to the total rate of recombination into level n = 2 and higher as a function of electron temperature.

Next, these emission rates are expressed in terms of intensity, an observable quantity. For each volume element, the intensity at the source is

$$(5) \qquad I_{o\nu} = \frac{E_\nu}{4\pi}$$

Integrating along the line of sight, and assuming some light is removed from the beam

$$(6) \qquad I_\nu = \int_0^L I_{o\nu} \, e^{-\gamma_\nu x} \, dx$$

where L is the distance through the nebula from the source and $\gamma_\nu x$ is the optical depth (τ). Note that τ can come from absorption by dust or from atomic absorption.

The integration is a simple one if it is assumed γ_ν and $I_{o\nu}$ do not depend on x

$$(7) \quad I_\nu = \frac{E_\nu}{4\pi}\left(\frac{1-e^{-\tau}}{\tau}\right)L$$

$$(8) \quad \text{Define } D_\nu = \frac{\tau}{1-e^{-\tau}}$$

$$(9) \quad \text{and } E_m = N_e^2 L$$

$$(10) \quad \text{then } I_\nu = \frac{E_m}{D_\nu} * \frac{E_\nu}{4\pi N_i N_e} * \frac{N_i}{N_e}$$

If the values of $I_{o\nu}$ and δ_ν do depend on x then Em must be assumed to represent a weighted average emission measure.

The expressions to be compared with the observations then become

$$(11) \quad I_{nn'} = \frac{E_m}{D_\nu}\,\frac{N_i}{N_e}\,\frac{KhZ^4}{4\pi}\left[b_n\,\frac{2g_{nn'}RcZ^2}{n'^3}\left\{\frac{1}{T_e^{3/2}}\,\frac{1}{n^3}\,e^{\frac{hRcZ^2}{n^2kT_e}}\right\}\right]$$

$$(12) \quad I_{bf} = \frac{E_m}{D_\nu}\,\frac{N_i}{N_e}\,\frac{KhZ^4}{4\pi}\left[\frac{e^{-\frac{h\nu}{kT_e}}}{T_e^{3/2}}\,g_{bf}\left\{\sum_{n>n'}^{16}\frac{e^{\frac{hRcZ^2}{n^2kT_e}}}{n^3}+\frac{\left(e^{\frac{hRcZ^2}{289kT_e}}-1\right)}{2hRcZ^2}kT_e\right\}\right]$$

$$(13) \quad I_{ff} = \frac{E_m}{D_\nu}\,\frac{N_i}{N_e}\,\frac{KhZ^4}{4\pi}\left[\frac{e^{-\frac{h\nu}{kT_e}}}{T_e^{1/2}}\,g_{ff}\,\frac{k}{2hRcZ^2}\right]$$

$$(14) \quad I_{2q} = \frac{E_m}{D_\nu}\,\frac{N_i}{N_e}\,\frac{KhZ^4}{4\pi}\left[\frac{1}{T_e^{3/2}}\left\{y\,\phi_1(y)\,\frac{2x}{3.77}\,\frac{\phi_2(\beta)}{\beta}\right\}\right]$$

These equations have a number of features which should be noted at this time. Since the electron density enters only in the emission measure, the ratio of the line intensity to the continuum intensity will be independent of density. Density fluctuations in the line of sight will not affect the ratio at a given frequency, nor will they affect it at different frequencies if the nebula is optically thin at those frequencies, i.e., if $D_\nu \approx 1$. As we shall see later, in the infrared wavelengths we are considering, the bound-free contribution to the continuum is about equal to the free-free contribution. Thus, there will be some dependence of the line to continuum ratio upon temperature, weaker than in the radio region, where the continuum is virtually all free-free, and stronger than in the visual where the continuum is bound-free and two quantum.

C. Reddening of M 42

One of the most important features of the infrared lines is that they are only slightly reddened, if at all. This will be shown in later sections of this chapter. The basic arguments are that the differential reddening between the higher order (10-14) Brackett lines at 1.6 μ and Brackett Gamma at 2.16 μ is small and also that the electron temperature calculated from Brackett Gamma and the radio continuum would be unrealistic if a large reddening correction were applied. Upon examining equations 1 and 11, one sees that if transitions from the same upper level are considered, a very simple expression for the ratio of line strengths can be derived. This is essentially just the ratio of the transition probabilities, purely atomic constants and independent of temperature and pressure. Strictly speaking, though, there is a temperature dependence which can creep in. If one considers the transitions in detail, one must talk of $b_{n,L}$ values instead of b_n values. For the values of n and the physical conditions considered here, the population among the various L values is not that of thermodynamic equilibrium. For the purposes of this discussion it is proposed to include this effect by substituting a new quantity $\overline{b_{nn'}}$ in place of b_n in the expressions for the line intensity. $\overline{b_{nn'}}$ is simply b_n times a correction factor which depends on the lower level through the permitted L values of the transition. $\overline{b_{nn'}}$ may be thought of as an effective level population parameter as far as the nn' transition is concerned. This formulation was first introduced by Burgess (loc cit). Equation 15 gives a more precise definition of $\overline{b_{nn'}}$ in terms of the squared radial matrix elements of the diploe moment, $|R_{nL,n'L'}|^2$, which appear in the transition probability.

$$(15)\quad \overline{b_{nn'}} = \frac{\sum_{L,L'} b_{nL} \max(L,L') \, |R_{nL,n'L'}|^2}{\sum_{L,L'} \max(L,L') \, |R_{nL,n'L'}|^2}$$

The $\overline{b_{nn'}}$'s do not exactly cancel and there can be a slight temperature dependence. Burgess (MN 118, 477, 1958) gets a 30% difference between Paschen and Balmer $\overline{b_{nn'}}$'s. Accordingly, $\overline{b_{nn'}}$'s were calculated separately for the lines given in Table 6. The radial matrix elements of the dipole moment were taken from Green et al. (ApJ Sup. 3, 37, 1958), and the $b_{(n,L)}$ were as given by Clarke (Thesis, Univ. Microfilm #6600211, 1965). Table 6 gives the $\overline{b_{nn'}}$'s used for the lines of interest, and Table 7 gives the predicted intensities with the emission measure and absorption left as adjustable parameters. Also shown in Table 7 are Seaton's (Rept. Prog. Phys. 23, 313, 1960) predicted values for some of the same lines for 10,000°K. Seaton did not have Clarke's accurate $b_{(n,L)}$ values, so the slight disagreement is not surprising.

From the data of Mendez (Bol. de Los Obs. Ton. y Tac., No. 28, p. 91, 1967) it is seen that the variation from position to position of the higher order Balmer and Paschen to H_β ratios is stronger than the variation with distance from the Trapezium. The area covered by the slits in this experiment's data is much larger than in any useful visual data. The available visual data also show a considerable

TABLE 6

POPULATION PARAMETERS FOR DEPARTURE FROM LTE

n	n'	$\overline{b_{nn'}}$ (T_e = 6000°K)	$\overline{b_{nn'}}$ (T_e = 10,000°K)
2	4	0.079	0.203
2	7	0.179	0.321
2	10	0.227	0.365
2	11	0.237	0.373
2	12	0.246	0.381
2	13	0.252	0.386
2	14	0.258	0.391
3	7	0.219	0.369
3	10	0.273	0.414
3	11	0.284	0.423
3	12	0.293	0.431
3	13	0.301	0.436
3	14	0.307	0.441
4	7	0.275	0.435
4	10	0.332	0.478
4	11	0.343	0.487
4	12	0.352	0.494
4	13	0.361	0.499
4	14	0.367	0.504

TABLE 7

PREDICTED LINE INTENSITIES

				Predicted Intensity · $\frac{D_\nu}{E_m}$ (W M^{-2} Str^{-1} Cm ^{6} Pc^{-1})		Seaton's Predicted
Element	Transition	λ (μ)	λ^{-1}	T_e = 6000°K	T_e = 10,000°K	T_e = 10,000°K
Hydrogen	7-4	2.17	.462	12.13 x 10^{-13}	7.20 x 10^{-13}	
	10-4	1.74	.576	3.96	2.38	
	11-4	1.68	.595	2.97	1.79	
	12-4	1.64	.609	2.27	1.38	
	13-4	1.61	.621	1.78	1.07	
	14-4	1.59	.630	1.42 x 10^{-13}	.841 x 10^{-13}	
	7-3	1.005	.995	23.02 x 10^{-13}	14.57 x 10^{-13}	
	10-3	.901	1.109	7.66	4.84	
	11-3	.886	1.128	5.76	3.66	
	12-3	.875	1.142	4.46	2.83	
	13-3	.866	1.154	3.46	2.17	

[continued on next page]

TABLE 7 (Continued)

Element	Transition	λ (μ)	λ^{-1}	Predicted Intensity · $\frac{D_\nu}{E_m}$ ($W\ M^{-2}\ Str^{-1}\ Cm^{6}\ Pc^{-1}$) T_e = 6000°K	T_e = 10,000°K	Seaton's Predicted T_e = 10,000°K
Hydrogen	14-3	.860	1.163	2.78×10^{-13}	1.72×10^{-13}	
	4-2	.486	2.058	429×10^{-13}	265×10^{-13}	259×10^{-13}
	7-2	.397	2.518	62.24	41.81	50
	10-2	.380	2.632	20.78	13.96	18
	11-2	.377	2.651	15.69	10.52	
	12-2	.375	2.666	12.16	8.13	
	13-2	.373	2.677	9.48	6.33	
	14-2	.372	2.686	7.63×10^{-13}	4.98×10^{-13}	
Neutral He	$4d\,^3D-3p\,^3P^0$	1.70	.692	22.93×10^{-13}*	15.17×10^{-13}*	
	$4d\,^3D-2p\,^3P^0$	.447	2.237	327.59×10^{-13}*	217.24×10^{-13}*	176×10^{-13}
Singly Ionized He	10-7	2.19	.457	21.55×10^{-13}*	14.35×10^{-13}*	

* Not corrected for abundance. f values for neutral He lines from Wiese et al. (NSRDS-NBS 4, 1966).

spread from observer to observer. Thus, it it not to be expected that the present visual data will allow an accurate estimate of the differential reddening across the nebula, and it has not been attempted.

In caluculating the reddening given in Figure 13, the values of the ratios of the various lines of interest to H_β were averaged from the values given by Mendez and then absolute values of H_β given by Mendez in regions near or in my standard regions were used to compute the energy in the visual lines listed in Table 8. These were then compared with the infrared lines from the same upper level to obtain the reddening, which is an average over the three central regions. Absolute values for the Paschen 12 line were taken from Werner et al. (ApJ 155, 485, 1969) and thus were reduced independently of the assumed H_β flux. No useable visual data could be found for the Dark Bay, so it was not possible to compute the reddening there by this method. The assumption was made that the 2 μ nebular reddening was 0.1 magnitudes. Johnson's (Nebulae & Interstellar Matter, Vol. VII of Stars & Stellar Systems, p. 167, 1968) Figure 37 for the Trapezium stars is also shown in Figure 13. Johnson's curve has been adjusted for his measured excess in B - V of 0.35.

The HeI line error bar includes ±20% for an estimated uncertainty from two causes. First, the He b_n values do not take into account the permitted L values of the transitions. Second, it appears (Drake et al., Phys. Rev. 180, 25, 1969) that Mathis' (ApJ 125, 318, 1957) He b_n values (the ones used) have been calculated assuming an incorrect rate of depopulation of the metastable 2^3S state. A

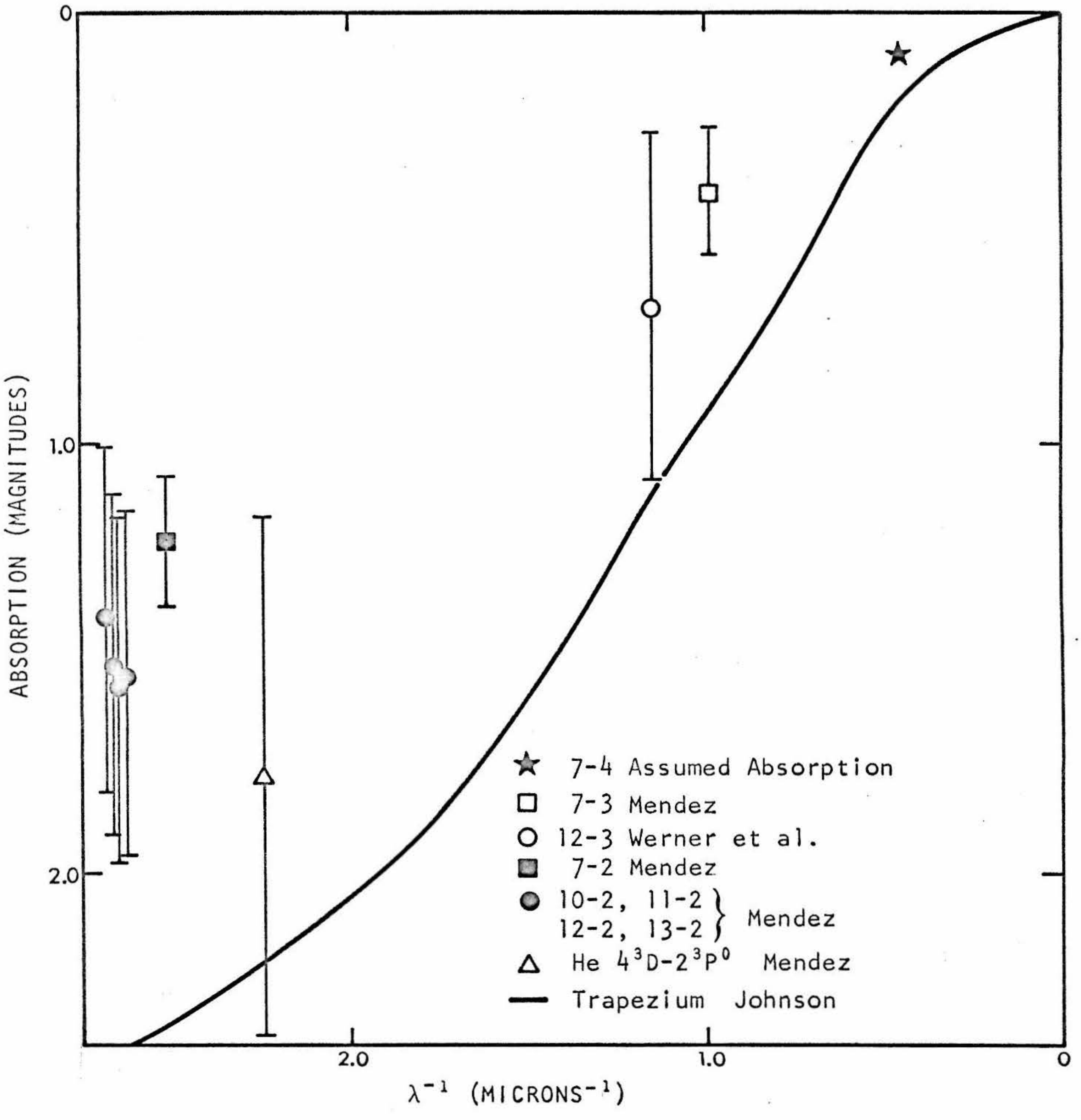

FIGURE 13 AVERAGE NEBULAR ABSORPTION COMPARED WITH ABSORPTION FOR TRAPEZIUM STARS

TABLE 8

ADOPTED RATIOS TO H_β

Transition	Ratio
3- 7	.118
He 4471	.035
2- 7	.149
2-10	.038
2-11	.033
2-12	.028
2-13	.021

ADOPTED VALUES OF H_β FLUX

Region	Intensity (W M^{-2} $Ster^{-1}$)
2) NOT 135"	7.8×10^{-6}
3) NOT 50"	19.1×10^{-6}
4) Trapezium	36.0×10^{-6}
5) SOT 50"	17.5×10^{-6}
6) SOT 135"	11.2×10^{-6}

slower rate of depopulation would make the higher triplet levels sensitive to the light from the Trapezium stars. Mathis' estimated rate was almost an order of magnitude too fast. However, it should be pointed out that the one photon decay rate of the 2^3S state has not been calculated, and, although it is highly forbidden, it may be faster than the two photon rate. Mathis' b_n values may be adequate.

Comparing the nebular reddening with the Trapezium reddening, it appears that Mathis' (ApJ 125, 328, 1957) assumption of a probable nebular reddening of ½ that of the Trapezium was correct. The reddening curves derived may be used to show that the Trapezium stars are behind most of the visible nebular material. If a very approximate equation of transfer, assuming constant nebular absorption and emission with depth, is used, it is possible to compute the depth of the Trapezium stars within the gas. That is, the intensity from the nebula is represented by Equation 16, and the flux from the stars is represented by Equation 17 where only the reddening factors are included.

$$(16) \qquad I_N \propto \frac{1 - e^{-\tau}}{\tau}$$

$$(17) \qquad I_S \propto e^{-\tau \frac{L_0}{L}}$$

L_0 is the unknown depth of the stars within the total depth L. From Equations 16 and 17 a differential reddening between the nebula and the stars can be predicted as a function of the stars' reddening and of L_0/L. Note that this relation is independent of the form of the reddening law. This relationship is shown in Figure 14 along with the observed points taken from 7-2 and 7-3 to 7-4 transition ratios. Thus, this simple model would indicate that the Trapezium stars are behind approximately 80% of the nebular material.

An argument can be made that the conclusions from this model and also Figure 13 would be incorrect if the 2 micron absorption were anomalously large, say 0.6 magnitudes. Johnson's absorption data apparently has some extra emission in the long wavelength regions, so the shape of the Trapezium absorption curve gives no strong counter argument. It would also be possible to account for a large 2 micron absorption with large particles. The reasons for assuming a small 2 micron absorption, however, are that (1) comparison of Brackett lines 10 through 14 with Brackett Gamma indicates little or no differential absorption between 1.6 microns and 2.2 microns, and (2) comparison of Brackett Gamma with radio data gives reasonable electron temperatures. Adding 0.5 magnitudes to the measured intensity of Brackett Gamma would drive the calculated electron temperatures down to around 3000°K. This does not rule out the possibility that the 2 micron absorption could be as high as .20 magnitudes or as low as no absorption with a corresponding shift of the points plotted in Figure 13.

A consideration which has been neglected is that if the extinction takes place within the gas, the starlight is reduced by both scattering

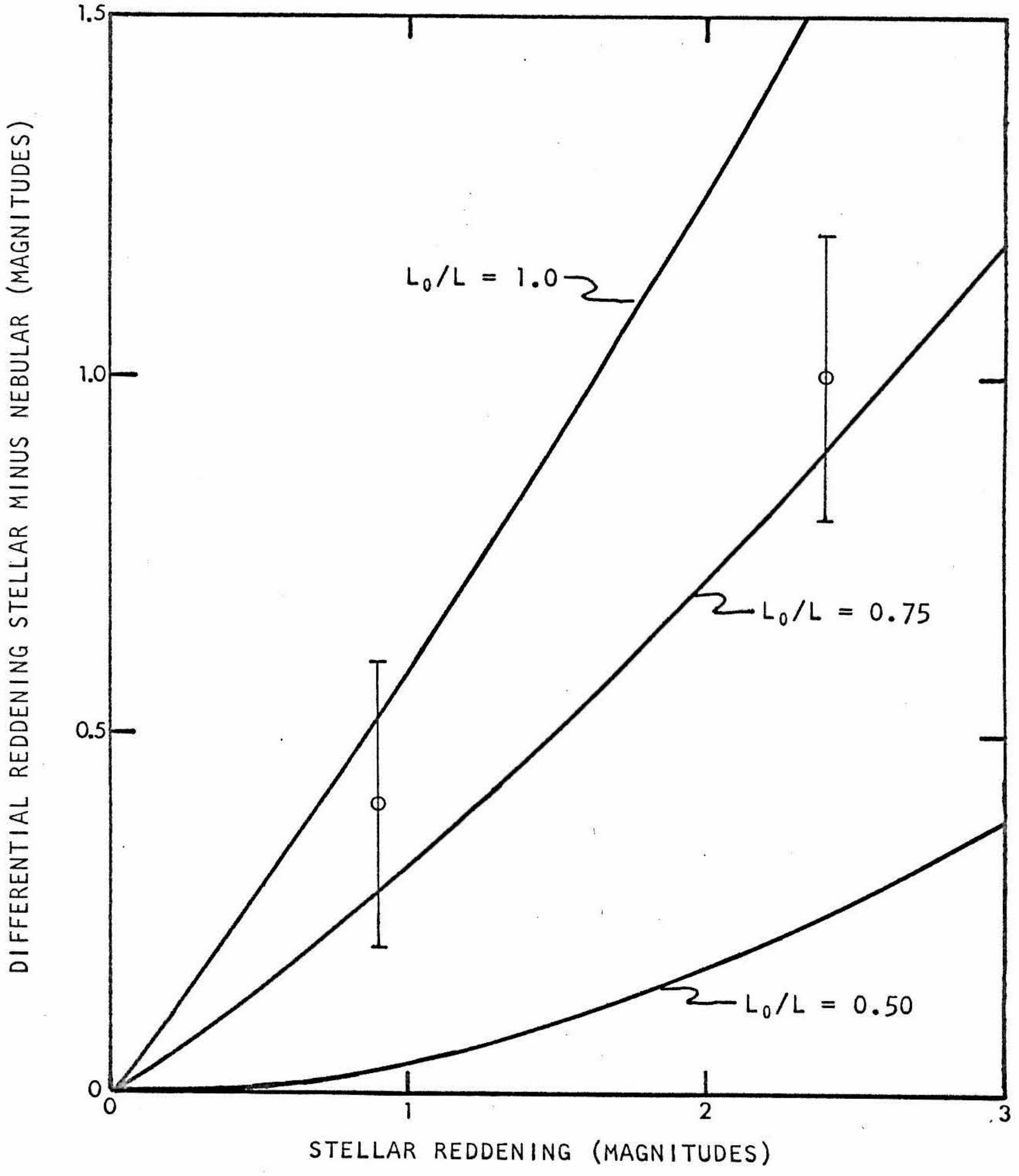

FIGURE 14 STELLAR MINUS NEBULAR REDDENING VS. STELLAR REDDENING FOR VARIOUS TRAPEZIUM POSITIONS

and absorption, whereas the nebular light is reduced by absorption only. A different form of the extinction law, as well as a smaller extinction than for the stars would thus be predicted for the nebula on this basis alone. The depth of the Trapezium within the gas could be thus reduced, but still could not be made zero. At zero depth, the Trapezium reddening would have to be all interstellar, as would the reddening of the nebula. Scattering would then add to the extinction of the nebula and a contradiction would exist between the extinctions of the stars and of the nebula. With this effect included, the Trapezium stars can then be said to be between 0.3 and 0.8 of the distance through the nebula.

Wurm (1963 Technical Report No. 1, AFCRL-63-730) has attempted to show that the Trapezium stars are in front of the nebula. Most authors have assumed symmetry and placed the Trapezium stars in the center, that is, behind the visible nebula.

The present results disagree somewhat with Mendez' (Bol de Los Obs. Ton. y Tac. 28, 91, 1967) similar calculation using the Paschen to Balmer line ratios. Mendez' value for the reddening between Paschen and Balmer wavelengths (approximately 0.8 magnitudes) agrees with this paper. He then uses some theoretical calculations (based on an assumed electron temperature of 10,000°K) which purport to show an additional 0.7 magnitude of reddening between the Paschen line wave-lengths and $\nu = 0$. That is, he gets a total visual reddening of 1.5 magnitudes. This is where we disagree. These data show half of the additional reddening to be fictional. Since Mendez had to use values for the emission measure at various distances from the Trapezium in his calculations, and since a different emission measure-distance relationship is derived in the present work, this is another possible explanation of the difference. A change in assumed electron temperature to 10,000° will affect the present method's results by only 5%.

While it is not possible to compute the absorption in the dark bay by the accurate method just used, an approximate value can be obtained from the reddening of the infrared flux. Looking ahead to Table 13, it is seen that the calculated temperature is hardly realistic. Inverting the calculation and assuming a realistic temperature should then enable the prediction of an unreddened line flux. If an electron temperature of 8000°K and an emission measure of 2×10^{6} $cm^{-6}pc$ is assumed, the unreddened intensity of Brackett Gamma should be 18×10^{-7} $wm^{-2}ster^{-1}$, a factor of 2.6 (1.05 magnitudes) greater than measured. From Johnson's Trapezium reddening curve, this would then imply between eight and twelve magnitudes of visual reddening. The question arises of whether it is valid to use the Trapezium reddening in this region. Johnson (Nebulae and Interstellar Matter, Vol. VII of Stars and Stellar Systems, 167, 1968) finds every star he has measured near this region to have essentially the same reddening law, so significant deviations are unlikely.

If an absolute stellar visual magnitude of -5, corresponding to a late main sequence O star, is combined with a distance modulus of 8.5 magnitudes, stars should be seen with a visual magnitude of 11.5

to 15.5. Inspection of a good photograph of the region shows no stars at all with a detectable limit of about 18th magnitude.

Admittedly, the derived visual reddening is somewhat uncertain, but it is an interesting exercise to examine the consequences if the discrepancy were real. In deriving the expected visual magnitude, the assumption has been made that the stars would show the same reddening as the nebula. As has been shown, for the Trapezium this is only true if the dust is in front of the nebula. The argument for the dust being in front of the nebula is essentially theoretical - if there were considerable dust mixed with the gas, the ionizing radiation would not easily penetrate and the gas-dust coupling would provide rapid cooling. The detection of the Brackett Gamma line from this region is proof that the ionized gas does exist. On the other hand, mixing the dust with the gas would allow the stellar reddening to be as much as six magnitudes greater than the nebular reddening in the visual, easily explaining the magnitude discrepancy. The choice of cloud positions appears to be balanced between two hypotheses, both of which have difficulties. Perhaps the cloud is partially mixed with the gas, and partially in front.

D. Reddening of the Planetaries

Since the two planetaries (IC 418 and NGC 7027) were measured on different telescopes, there exists a considerable difference in S/N. Accordingly, they will be treated separately.

IC 418 was observed on the 60 inch and has such low S/N compared with the known small amount of reddening that there is little hope of adding any useful information to the reddening law. Instead, the known reddening will be used along with Balmer and Paschen line strengths to predict the expected flux of Brackett Gamma. Since the line flux from IC 418 was some seven times fainter than the line flux from the faintest region measured in M 42, this method can provide a check on the accuracy of the M 42 spectra.

Table 9 shows the reddened fluxes adopted for IC 418 and NGC 7027 for H_7 and P_7. The fluxes are taken from O'Dell (ApJ 138, 1018, 1963 and ApJ 135, 371, 1962). The H_7 line is a blend with a NeIII line, so the flux was estimated by interpolation between adjoining Balmer lines free of blends. The value obtained is in agreement with Wyse's (ApJ 95, 356, 1942) estimate of the relative contribution of the two lines to the blend.

The values of the Brackett Gamma flux predicted for IC 418 using the measured Balmer and Paschen fluxes, and the reddening curve given by Pipher and Terzian (ApJ 155, 475, 1969) and an electron temperature of 10,000°K are 2.2×10^{-14} wm^{-2} from H_7 and 1.9×10^{-14} wm^{-2} from P_7. This is in satisfactory agreement with the measured flux of

TABLE 9

ADOPTED VISUAL LINE FLUXES FOR PLANETARIES

Object	Adopted Flux (W/M^2)	
	Balmer 7	Paschen 7
IC 418	3.9×10^{-14}	3.2×10^{-14}
NGC 7027	$.81 \times 10^{-14}$	4.1×10^{-14}

1.4×10^{-14} wm^{-2} ± 0.6 from this experiment. If all the difference came from a flux loss in the spectrometer, then the worst data on M 42 would be good to 3%. This is a good check for absolute losses, but not percentage losses (which were covered in Chapter III).

NGC 7027 was observed on the 100 inch, so the S/N is considerably better than for IC 418. In addition, the reddening is seven times as large. The reddening at P_7 and H_7 was calculated from the value of B_7 observed in this experiment assuming an electron temperature of 10,000°K, and is shown in Figure 15. Also shown is O'Dell's (ApJ 138, 1018, 1963) curve derived by fitting a standard interstellar reddening curve as given by Seaton (Repts. on Prog. in Phy. 23, 313, 1960) to observed line ratios between the Paschen and Balmer series. This experiment's points have been fitted to O'Dell's curve at P_7. Within the accuracy of the present experiment, there is no disagreement.

While it is possible that all the extinction is interstellar, the 10 micron measurement of NGC 7027 by Gillet et al. (ApJL 149, 97, 1967) suggests dust absorption and reemission within the gas. The amount of absorption by dust within the nebula (again, scattering does not contribute to the intranebular extinction) can be approached in two ways. An estimate can be made of the optical depth either by comparing the brightness temperature of the dust with its color temperature or by comparing the energy emitted by the dust with the total energy emitted by the nebula. From the paper by Gillet et al., it may be assumed the spectrum peaks at 20 microns at 7×10^{-24} $wm^{-2}Hz^{-1}$

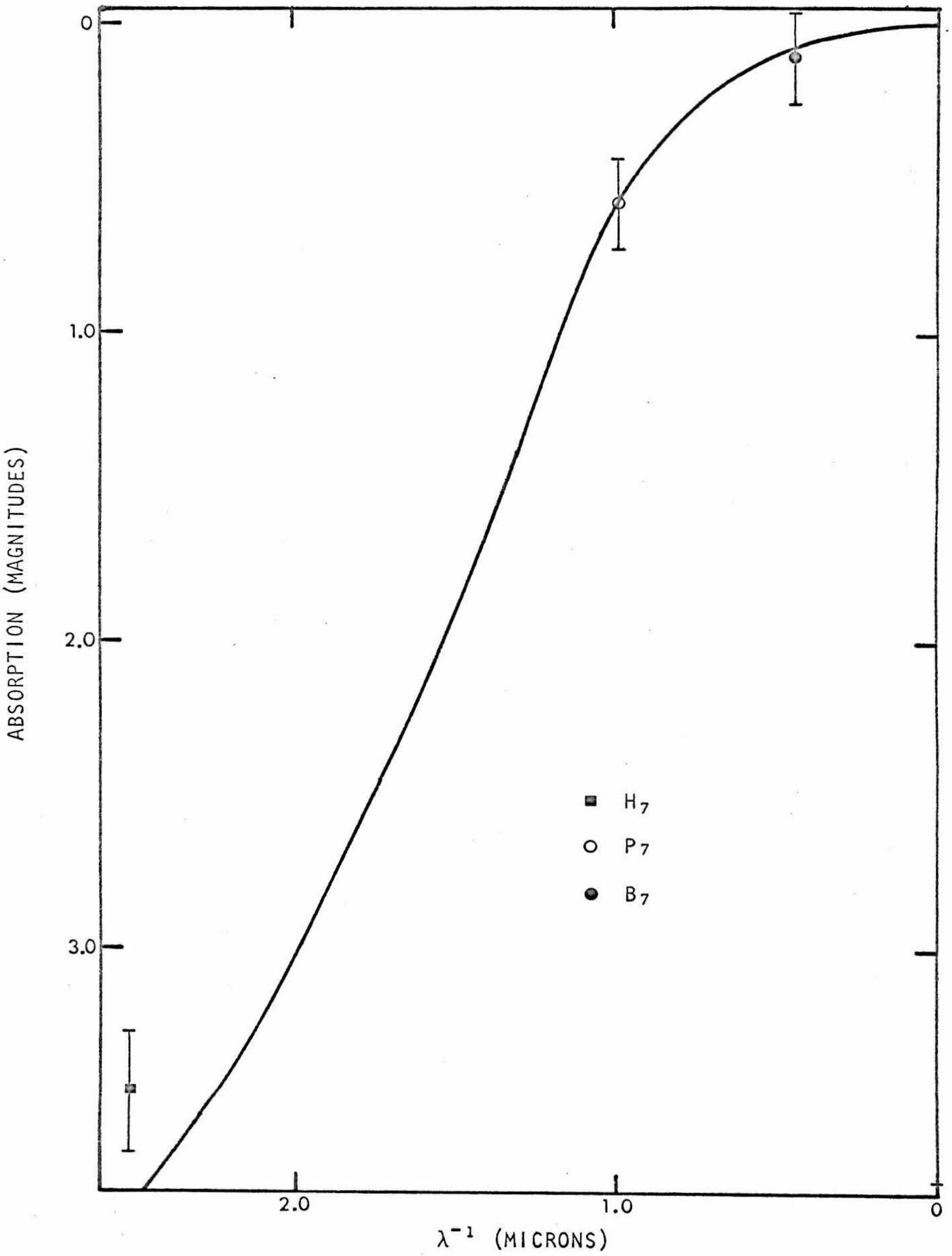

FIGURE 15 REDDENING OF NGC 7027

and that the color temperature is 250°K. From Thompson et al. (ApJ 148, 429, 1967) the solid angle subtended is 2.7×10^{-9} ster. A value of τ of 0.10 is obtained if the dust emissivity is taken as 0.01.

From the paper by Gillet et al., it may also be estimated that approximately half the nebular light is emitted by the dust (if the ultraviolet leakage is small). Assuming that a third of the heating energy comes from the starlight directly, a value of τ of 0.15 is obtained. These two results have required a number of simplifying assumptions, but they should at least be good to an order of magnitude, sufficient for the present argument.

Essentially, the conclusion is that despite the large dust emission, the nebular contribution to the extinction is small compared with the interstellar extinction. Unlike the Orion Nebula, the dust properties of NGC 7027 can only be determined by infrared observations.

E. Helium Abundance in M 42

From the ratios of the hydrogen and helium lines, it is possible to measure the abundance of helium relative to hydrogen.

The method assumes that the ratio of the number densities of hydrogen and helium is equal to the ratio of the emission measures for hydrogen and helium, all other factors cancelling out in the intensity ratios. Since the emission measure is an average over the line of sight, several uncertainties arise over this simplification. First, there is the question of the relative radii of the Stromgren spheres for the hydrogen and helium. Swihart (Thesis, University of Indiana, 1952) has treated this problem in some depth. With reasonable assumptions for the temperature of the Trapezium stars (40,000°K) and for the ratio of the number densities of hydrogen to helium (10), M 42 falls well within the region of Swihart's calculations where the radii are equal. Then if the gross regions of emission coincide, the emission measures can be said to represent averages over the same regions. Of course, because of density fluctuations, temperature variations, and reddening within the regions, even these averages must be interpreted with some caution.

Experimental evidence (also the results of this paper) suggest an error in Swihart's calculations. Johnson (ApJ 118, 370, 1953) found that the ratio of He 5876 to H_β varies strongly with distance from the Trapezium. This would indicate that singly ionized helium is becoming less abundant with increasing distance from the

Trapezium; the logical assumption is not that the total abundance is changing, but that the helium is becoming neutral.

The abundances measured by various observers are shown in Table 10, corrected to Mathis' b_n values, and the values from the present data in Table 11. Also included in Table 11 is the minimum abundance which could have been detected for doubly ionized helium. Since Mathis (ApJ 126, 493, 1957) has shown several planetaries with properties similar to M 42 to have an He III abundance ratio of approximately 0.05, the non-detection is somewhat surprising and lends credence to the idea that the helium is not fully singly ionized. The non-detection is also in agreement with the radio limit shown.

The present data gives a lower abundance than has been generally obtained visually. Also, the abundance appears to decrease away from the Trapezium. Despite the supporting evidence from the radio lines, the lower abundance is probably not caused by the different depths in the nebula which are seen in the visual and infrared. It is likely that the theoretical helium decrements will require a more refined calculation before any of these methods (infrared included) can be trusted. A glance at Table 10 shows considerable differences from line to line, even for the same observer.

TABLE 10

ABUNDANCE OF HELIUM IN M 42 (VISUAL AND RADIO LINES)

	Measured By				
From Line	Wyse (1942)	Tcheng and Dufay (1944)	Johnson (1953)	Mathis (1957)	Aller and Liller (1959)
10830					0.24
5876	0.27		0.37	0.18	0.28
4471	0.16	0.71		0.19	0.12
4026	0.16	0.43		0.16	0.15
		Palmer et al. (ApJ <u>156</u>, 887, 1969)			
He 109α, H 109α		$N_{He^+}/N_{H^+} = 0.083\pm0.004$		$N_{He^{++}}/N_{H^+} \leq 0.003$	

TABLE 11

ABUNDANCE OF HELIUM IN M 42 (INFRARED LINES)

Region	N_{He^+}/N_{H^+}*	$N_{He^{++}}/N_{H^+}$**
50'' North of Trap.	$.049\pm^{0.05}_{0.02}$	≤ 0.03
Trapezium	$.105\pm^{0.10}_{0.05}$	
50'' South of Trap.	$.060\pm^{0.06}_{0.03}$	

* Measured from λ1.700μ $4d\,^3D \rightarrow 3p\,^3P^0$

** Attempted Measurement λ2.191μ He^+ 10-7

F. The Anomalous Satellite Line in NGC 7027

A faint line was observed near the Brackett Gamma line on each of the two nights of observing NGC 7027. The intensity and wavelength are given in Table 2. The accuracy of the wavelength is about 20 Å, so the line has tentatively been identified as the $7d^1D-4p^1P^0$ transition of HeI. Making this identification introduces a problem in that the helium abundance then appears anomalously high. This may be shown by a comparison with an Orion Nebula spectrum, or by direct calculation.

The 2.184μ line was not seen in the Orion Nebula spectrum. From the minimum line intensity which could have been detected in M 42, it follows that the abundance of HeII relative to hydrogen is at least five times higher in NGC 7027 than in M 42. That is, if the M 42 N He II/NH II ratio is 0.08 (see Section E), the implied ratio for NGC 7027 is 0.40 or greater. A direct calculation, assuming the population factor (b_n) to be 0.2 gives an abundance NHe II/NH II = 0.49 ± 0.15.

The above determinations are to be compared with the value of the He abundance for NGC 7027 of 0.10 given by Osterbrock (Ann. Rev. 2, 95, 1964). The difference is larger than might be believed from experimental error, so it is concluded that either the line is misidentified, or some mechanism such as resonance fluorescence is acting, or Osterbrock's value is wrong. It should be pointed out that further infrared spectral observations outside the narrow band covered by the present data might help to resolve the first two of the above possibilities.

G. The Brackett Lines 10-14 in M 42

Figures 16-18 show the observed intensities of the Brackett lines (corrected for reddening by the nebular reddening curve derived in Section C) at several positions in the nebula. Also shown are the intensities expected at 10,000°K and 6,000°K if the emission measure were fitted to the B_7 point. Note that the expression for the intensity (Equation 11) has two independent parameters - the emission measure and the electron temperature. Clearly, a single line may be fit in an infinity of ways. The emission measure may be eliminated if only ratios of line strengths are considered. This is essentially what has been done here by adjusting the value of the emission measure to fit the B_7 point. The Brackett decrement (here meaning line ratio to B_7) is clearly not a sensitive function of temperature. Thus, even a set of lines can be fit with a large spread of values of emission measure and electron temperature. Instead of trying to determine the parameters with these data, it makes more sense to use the fact that the decrement is independent of the emission measure and insensitive to the temperature in order to check other assumptions. The reasonable agreement between the observed and predicted decrement is an indication that the reddening correction is not far wrong and also that the overall observation-theory description is a good one. Other than these qualitative comparisons, the higher order Brackett lines are not accurately enough observed to test theoretical predictions. They will, however, be used in Chapter IV to demonstrate an excess continuum in the 1.6 micron band, an unexpected property of M 42.

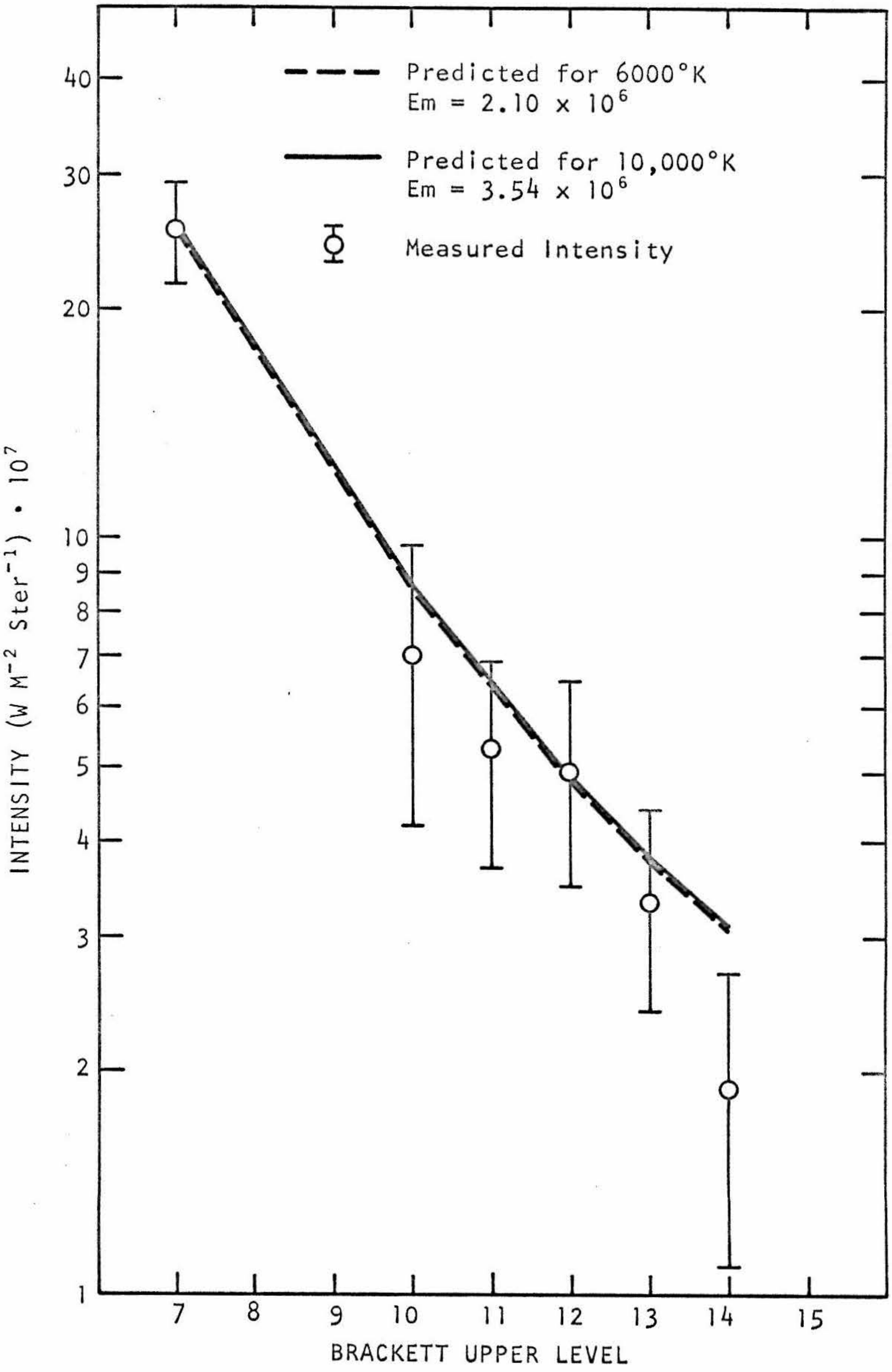

FIGURE 16 BRACKETT LINES - 50'' SOUTH OF TRAPEZIUM

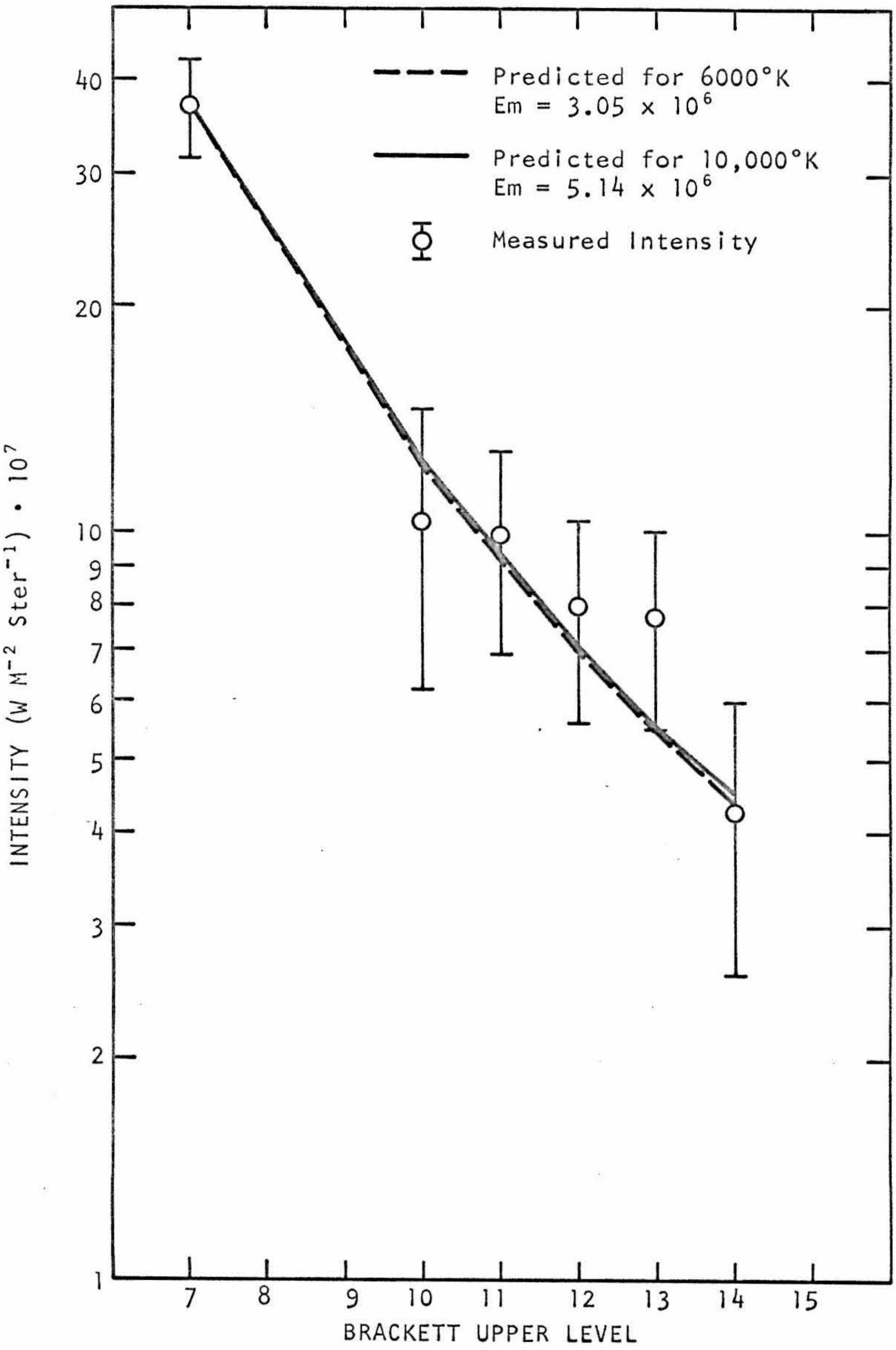

FIGURE 17 BRACKETT LINES - TRAPEZIUM

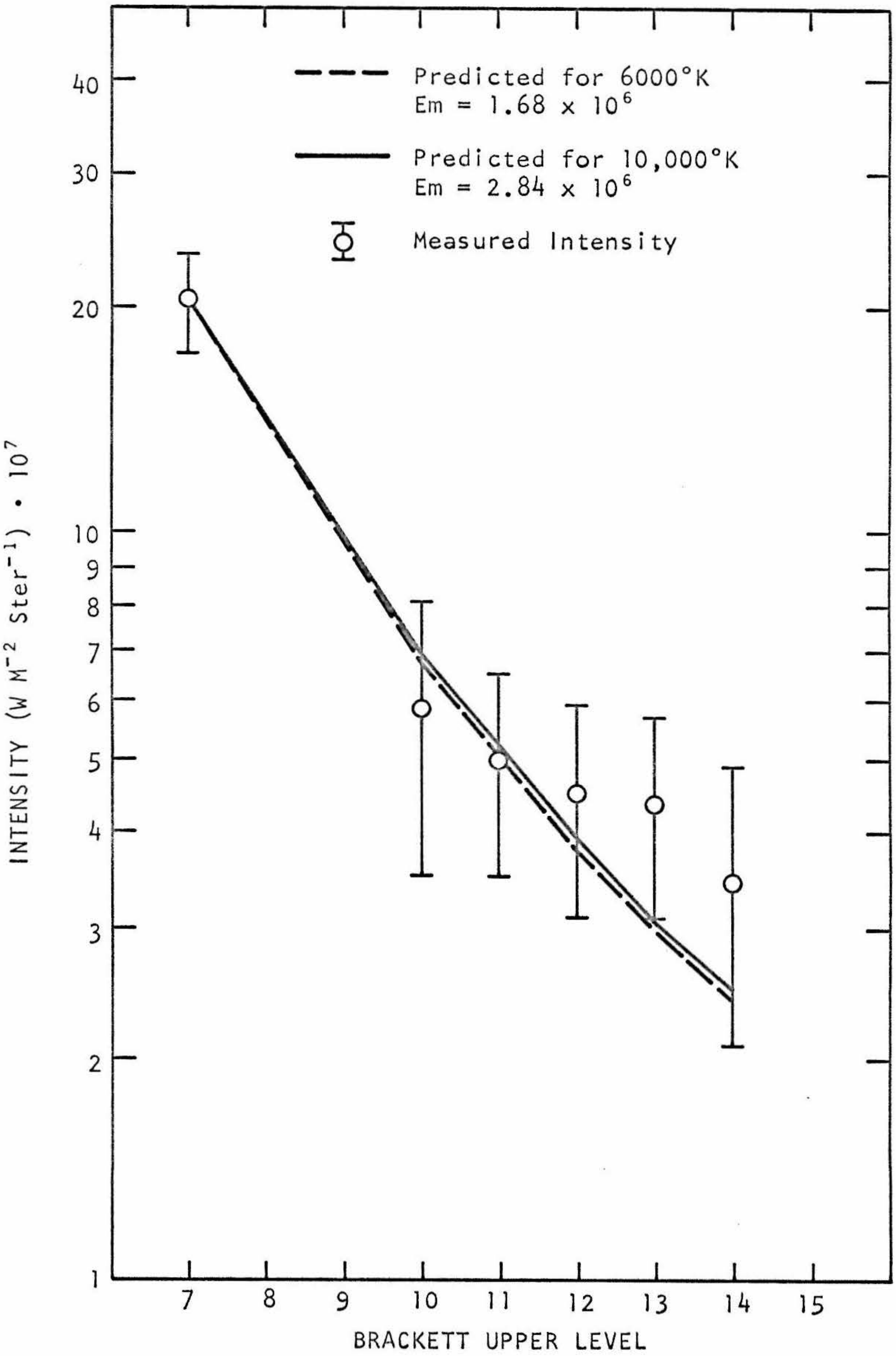

FIGURE 18 BRACKETT LINES - 50" NORTH OF TRAPEZIUM

H. Te and Ne in M 42

A determination of the electron temperature and emission measure can be made by comparison of the Brackett Gamma line with radio measurements of the free-free continuum.

At the higher radio frequencies, Equation 13 becomes

$$(18)\quad I_{ff}^{RADIO} = E_m \cdot 9.73\times10^{-21}\,\frac{(17.65 - \ln\nu + \frac{3}{2}\ln T_e)}{T_e^{1/2}}\ \mathrm{ERG\,SEC^{-1}\,CM^{-2}\,H_Z^{-1}\,STER^{-1}}$$

D_ν has been set equal to 1 since self absorption and dust absorption and emission should be negligible. This will be demonstrated later. The radio Gaunt factor has been adopted from Oster (R M P 33, no. 4, 525, 1961)

$$(19)\quad g_{ff}^{RADIO} = \frac{\sqrt{3}}{\pi}\ln\left[\frac{(2\,k\,T_e)^{3/2}}{4.22\,\pi\,m^{1/2}\,e^2\,Z\nu}\right]$$

the number densities of helium have been assumed to be NHe II/NH II = 0.10 and NHe III/NH II = 0.03. These enter into Equation 13 both in the nuclear charge dependence of the Gaunt factor, and in the electron to proton ratio of the gas.

For the Brackett Gamma line, Equation 11, corrected for helium blends, with the same assumed He number densities as above, becomes

$$(20)\quad I_{74} = 1.27\times10^{-3}\,\frac{B_7(T_e)\,E_m}{T_e^{3/2}}\;e^{\frac{3220}{T_e}}\ \mathrm{ERG\,SEC^{-1}\,CM^{-2}\,STER^{-1}}$$

where the reddening has not been included. Taking the ratio and ignoring possible differences in E_m between the two types of data, the density factor cancels and only a temperature dependence remains (at a given radio frequency)

$$(21)\quad \frac{I_{ff}^{RADIO}}{I_{74}} = 7.66 \times 10^{-18} \cdot \left(17.65 - \ln \nu_{RADIO} + \tfrac{3}{2} \ln T_e\right) \frac{T_e}{B_7(T_e)} e^{-\frac{3220}{T_e}} H_\gamma^{-1}$$

To get the radio continuum, we refer to the paper by Schraml and Mezger (ApJ <u>156</u>, 269, 1969). From the contour map given, the average brightness temperature at each of the six regions observed in Brackett Gamma has been converted to intensity by means of Equation 22 and is given in Table 12.

$$(22)\quad I_\nu = \frac{2 k T_B}{\lambda^2} = 7.26 \times 10^{-13} T_B$$

The emission measure and electron temperatures which follow from an iterative solution of Equation 21 are given in Table 13.

Several very interesting features appear, some contrary to externally determined parameters of the nebula. While comparisons with outside data will be reserved for the next three sections, it is worthwhile at this time to point out the more important inferences to be drawn from Table 13.

The temperature calculated for the Dark Bay is clearly too high. No reddening correction has been applied to this datum, so it is shown separated from the rest of the data, which were calculated with B_7 corrected by 10% for reddening. As was discussed in Section C, the temperature can be made reasonable if a reddening correction of a factor of 2.6 is applied.

Looking at the data for the more visible regions, an average electron temperature of 8000°K is obtained. The individual points

TABLE 12

ADOPTED RADIO INTENSITIES (15.375 gHz)

Region	T_b (°K)	I_ν (Erg Sec^{-1} Cm^{-2} Hz^{-1} $Ster^{-1}$)
1) Dark Bay	26	1.89×10^{-15}
2) 135'' NOT	12.2	0.886
3) 50'' NOT	30.0	2.18
4) Trapezium	32.0	2.32
5) 50'' SOT	28.5	2.07
6) 135'' SOT	13.9	1.01

TABLE 13

DERIVED TEMPERATURES AND EMISSION MEASURES

Region	T_e (°K)	Em (Cm^{-6} Pc.) $\times 10^{-6}$
1) Dark Bay	$34,800\pm^{6100}_{5400}$	3.7 ± 0.2
2) 135'' NOT	$9,200\pm^{2300}_{1900}$	1.1 ± 0.1
3) 50'' NOT	$10,700\pm^{2700}_{2200}$	2.9 ± 0.2
4) Trapezium	$5,200\pm^{1100}_{800}$	$2.4\pm^{0.2}_{0.1}$
5) 50'' SOT	$7,200\pm^{1800}_{1400}$	$2.4\pm^{0.2}_{0.1}$
6) 135'' SOT	$7,800\pm^{1900}_{1500}$	1.2 ± 0.1
Avg. T_e	8,000	

show a large spread which is not random around this average. The effect is of an increase in temperature with greater distance from the center of the nebula. To explain this by reddening would require the reddening to increase away from the center of the nebula, an unlikely possibility, and would also require a change in the 2 micron reddening amounting to nearly a factor of two in intensity, also unlikely. Mendez (Bol. de Los Obs. Ton. y Tac. 28, 91, 1967) finds a reddening which decreases away from the center of the nebula.

The region 50" north of the Trapezium shows a considerable amount of dust emission in the infrared (Ney and Allen ApJL 155, 193, 1969) so it is possible that a very slight (10%) increase in the two micron reddening in this region would apply. This correction would then bring the calculated temperature in this region down to about 9800°K. The change is hardly significant, considering the errors.

The emission measure at the Trapezium is 2.4×10^6 pc cm^{-6} and shows a slight decrease with greater distance from the center of the nebula.

One possible explanation for the decrease in temperature to the center is that the spatial resolution of the radio data is weighting the regions differently. Accordingly, the regions of this investigation were degraded by adding together to get about the same spatial resolution (2') as the radio data. The results are shown in Tables 14 and 15. The same decrease to the center is seen, but it is now barely significant. An average electron temperature of 8400°K is

TABLE 14

ADOPTED RADIO INTENSITIES (15.375 gHz) CORRESPONDING TO COMBINED INFRARED REGIONS

Region	T_b (°K)	I_ν(Erg Sec^{-1} Cm^{-2} Hz^{-1} $Ster^{-1}$)
2+3	24.5	1.78×10^{-15}
3+4	31.0	2.25
4+5	31.0	2.25
5+6	22.5	1.63

TABLE 15

DERIVED TEMPERATURES AND EMISSION MEASURES FOR COMBINED INFRARED REGIONS

Region	T_e (°K)	Em (Cm^{-6} Pc.) $\times 10^{-6}$
2+3	$12{,}600\pm^{2200}_{1800}$	$2.5\pm^{0.1}_{0.2}$
3+4	$6{,}900\pm^{1200}_{1000}$	2.6±0.1
4+5	$6{,}100\pm^{1100}_{900}$	2.5±0.1
5+6	$8{,}000\pm^{1400}_{1200}$	2.0±0.1
Avg. T_e	8,400	

obtained.

The calculation of the electron temperatures by this method is rather sensitive to errors in absolute intensities in either the radio or infrared data. A non-quantitative argument exists, however, which demonstrates the temperature decrease to the center of the nebula and which is independent of absolute calibrations and insensitive to different spatial resolution. The argument is based on a comparison of the half-power points of the radio and infrared data along a north-south line. The radio FWHM from Schraml and Mezger (ApJ 156, 269, 1969) is 244 arc seconds and the FWHM in Brackett Gamma from this investigation is 130 arc seconds. Corrections for the beam widths bring these down to 210 arc seconds and 120 arc seconds for the radio and infrared measurements respectively. The most reasonable explanation for this disagreement is a temperature increasing outward from the Trapezium.

I. Comparison of Average Temperatures for Ionized Regions of M 42

The average of the temperatures from Table 15 is 8400°K. Although the spread in determining this number is large, it is still interesting to compare it with other determinations. A summary of characteristic determinations of the electron temperature from a number of different optical and radio observations is given in Table 16. Quoted statistical errors generally are in the range 800°K to 1500°K and are not included since systematic errors are clearly more important.

For this discussion, it should be remembered that all methods of determining electron temperature now used are sensitive to the calculation parameters. That is, changes of 1000°K or more in calculated values can be caused by errors of 10% in the data or in the theoretical predictions. With an acceptance window of about 2000°K, the data in Table 16 can be divided into four broad classes of temperatures centered at 3000°K, 7000°K, 9000°K, and 11,000°K. The full range is outside of experimental error, and probably reflects theoretical difficulties, oversimplified models, incorrect assumptions, etc.

Discussing first the low temperature values, the 1200°K determination by Kaler appears to have good data. The reddening, however, was determined by the method of fitting Paschen-Balmer line ratios to a standard interstellar reddening curve, and this is a possible source of the unreasonable temperature. Johnson (Nebulae & Interstellar

TABLE 16

ELECTRON TEMPERATURES DETERMINED BY VARIOUS METHODS

T_e	Method Used	Reference
1,200°K	Balmer Decrement (High n Lines)	Kaler (ApL 1, 227, 1968)
3,000°K	Free-Free Continuum Shape (Radio)	Terzian et al. (ApL 1, 153, 1968)
4,700°K	Balmer Cont./H_β	Lee (ApL 1, 225, 1968)
6,800°K	Hydrogen 109α Line	Mezger and Ellis (ApL 1, 159, 1968)
6,800°K	Balmer Jump/H_β	Peimbert (ApJ 150, 825, 1967)
8,000°K	Free-Free T_b at 408 MHz	Mills and Shaver (Aust. J. Phys. 21, 95, 1968) Corrected by Shaver (MNRAS 142, 273, 1969)
8,300°K	O III Line Ratios	Peimbert, Priv. Comm. to Terzian et al. (ApL 1, 153, 1968)
8,400°K	Brackett γ/Radio Cont. (15 GHz)	Hilgeman (Ph.D. Thesis, Cal. Tech., 1970)
9,000°K	O III Line Ratios	O'Dell (ApJ 143, 168, 1965)
9,200°K	O III Line Ratios	Kaler (ApJ 143, 722, 1966) Peimbert (ApJ 150, 825, 1967)
9,300°K	O II & N II Lines/H_α	Pottash (Vistas in Ast. 6, 149, 1965)
9,700°K	Line Widths - O II, O III, H	Munch (RMP 30, 1035, 1958)
11,000°K	$H_{n\alpha}$, $H_{n\beta}$, $H_{n\gamma}$, $H_{n\delta}$ Lines	Hjellming and Churchwell (ApL - To Be Published)
11,000°K	Free-Free Continuum Shape (Radio)	

[continued on next page]

TABLE 16 (Continued)

T_e	Method Used	Reference
11,000°K	0 II to N II Line Ratios	Peimbert, Priv. Comm. to Terzian et al. ApL 1, 153, 1968)
13,000°K	0 II to N II Line Ratios	Peimbert (ApJ 150, 825, 1967)

Matter, Vol. VII of Stars & Stellar Systems, p. 167, 1968) has shown that the reddening in the Orion Nebula has a different wavelength dependence than the standard interstellar reddening. The difference is such that if Kaler had used the correct reddening function, he would have gotten somewhat lower values for the high-n intensities and a considerably higher temperature. A rough estimate suggests the corrected temperature should lie between 5000°K and 10,000°K.

It should be pointed out that even with this modification, the data suffer from a difficulty common to all the visual data. That is, because of the dust, visually derived parameters must necessarily be heavily weighted to the near side of the nebula and probably are representative only of the outer regions on the near side. Since the electron temperature is a function of distance from the Trapezium, visual temperature determinations which involve different characteristic wavelengths (and thus different depths of penetration of the dust) will show different temperatures even if done correctly.

The 3000°K determination by Terzian is based on the observed turndown in the radio spectrum at frequencies where the nebula becomes optically thick. Because the radio observations were made with various spatial resolutions which were generally large compared with the size of the nebula, the theoretical predictions depend not only on temperature, but also on a model for the emission measure as a function of distance from the Trapezium. This model is highly uncertain, as can be seen by comparing the temperature of 11,000°K, which Hjellming gets from a different model, using the same data. Until more is understood about the details of the nebular structure, this method of determining the electron temperature must be considered unreliable.

The temperatures of 4700°K by Lee and 6800°K by Peimbert are obtained by comparing the energy in the Balmer Discontinuity with that in H_β. Aside from certain difficulties such as the differential reddening and the estimation of the Balmer Continuum, the data may represent a real temperature. That is, the extinction is quite large at the wavelength of the Balmer Discontinuity, so only the very outer regions of the nebula are seen.

The measurement of 8000°K by Mills and Shaver uses the fact that at low radio frequencies the nebula is "optically thick." That is, the antenna brightness temperature T_b is identical with the nebular electron temperature T_e. It is not felt that the value obtained is in serious disagreement with higher temperatures. This is because the high "optical thickness" precludes seeing the center of the nebula.

The temperature of 6800°K by Mezger and Ellis is typical of many determined from the ratio of high level hydrogen lines to the continuum. When properly done, non-LTE calculations imply a maser effect in the radio lines. The data under discussion did not take this effect into account. As will be shown later, the more comprehensive theory gives a temperature of approximately 11,000°K. Note that this method and the infrared line to radio continuum method used in the previous section are the only methods which can hope to determine the temperature near the center of the nebula since it is only in the wavelength range from 2 microns to 30 cm. that the nebula is transparent.

The O III line ratio measurements by many authors range from 8300°K to 9300°K. These are probably fairly reliable determinations despite the difficulty involved in calculating forbidden line upper level populations. Note that the wavelengths are longer than for other visual data which have been discussed, thus permitting a deeper penetration into the nebula and explaining a higher temperature. Note also that the lines are close enough in wavelength that the differential reddening is small.

The temperature of 9300°K obtained by Pottash by taking the ratios of forbidden oxygen and nitrogen lines to H_α is probably very inaccurate. Theoretical uncertainties in the line ratios and experimental uncertainties in the reddening make this determination unreliable. It is probably only fortuitous that it is near a believable temperature.

For the same reasons that the O III line ratio temperatures are acceptable, the measurement by Munch of 9700°K using O III and H_γ line widths should also be. There is a possibility that the value may be a bit high because of a weighting toward regions of higher temperatures.

The temperatures of 11,000°K and 13,000°K which Peimbert obtains from the ratio of O II lines to N II lines are probably rather uncertain. The theoretical forbidden line strengths are less certain than those of hydrogen, and these particular lines have large differential reddening corrections.

Hjellming and Churchwell's temperature of 11,000^{o}K represents a three parameter (T_e, N_e, Em) fit to all existing radio line data using a revised non-LTE calculation first proposed by Goldberg (ApJ 144, 1225, 1966). The fit is excellent. The question arises whether this temperature is significantly different from the infrared determination of the previous section. The errors involved in representing the Orion Nebula emission by a delta function centered at the Trapezium are hard to estimate but five percent is probably not unreasonable. The helium contribution to the free-free continuum prediction could also be off by five percent. It is also not known what the effect of a distribution of temperature across the nebula instead of a single temperature would have on the fit to the data.

A sample set of predictions of the non-LTE theory (Hjellming et al. ApL 3, 111, 1969) can be used to estimate the effect of an error in the predictions on the temperature. If the predicted continuum were underestimated by 10%, the best fit temperature would drop to around 9000^{o}K. This is only a crude estimate, but should be adequate to show that the possible errors are large. The disagreement with the infrared data is probably not significant. Note that uncompensated reddening of the infrared lines would make the infrared line estimated temperature appear too high, not too low.

In summary, measurements of electron temperature and the interpretation of the measurements is a non-trivial task. Visual and long wavelength radio measurements do not penetrate the entire nebula and the temperatures from them must be regarded as characteristic only of the nearer regions. Of the two methods which do penetrate the nebula, each has its disadvantages. The radio line to radio continuum ratio method requires complicated non-LTE calculations, a three parameter representation, and is incapable of accounting for temperature variations across the nebula in any simple way. The infrared line to radio continuum ratio method involves measurements at different wavelengths and different spatial resolutions. Nevertheless, these two methods give reasonably close agreement. It is hoped that the addition of the infrared temperature to the published data will help to resolve the current high temperature-low temperature controversy.

J. Comparison of Temperature Variations

None of the methods of calculating electron temperatures permit an accurate determination. It might be expected, however, that the relative values of the temperature at different distances from the Trapezium would be in agreement. This is not the case. As a rough orientation to what is to follow, theoretical energy balance considerations predict an electron temperature which increases outward to the edge of the ionized region then falls off. Experimental data to date have indicated either a flat temperature distribution or one which decreases outward. The results of this experiment agree with the theoretical predictions, and, at first glance, appear to disagree with all previous experimental results. Clearly some discussion is in order. This section, then, consists of a review (with comments) of the theoretical predictions and outside experimental results.

Hjellming (ApJ 143, 420, 1966) has given a dynamical model which predicts a temperature rise away from the center. The basic physical reason is that the ionization cross section is higher for lower enegy photons. Thus, the lower energy photons are captured preferentially closer to the source, and the higher energy photons are captured preferentially further from the source. Unfortunately, Hjellming's model is for a uniform density H II region, so it is not certain that his conclusions can be applied to the Orion Nebula. One consequence, though, of adopting a temperature rise going away from the Trapezium is that the calculated emission measure (and thus the electron density does not decrease strongly with distance. Thus, as we shall see later, there is a possibility that the average density over large volumes is constant, at least in the Huygenean region.

While there are theoretical reasons for the decrease to the center, experimental radio data to date have indicated an increase to the center or no change. Mezger and Ellis (ApL 1, 159, 1968), with a 6' half power beam width at 5 gHz, show a temperature 6800°K constant to ±200°K going south at least 4' from the Trapezium. Going north, there is a decrease followed by an increase and another decrease, but the temperature can be said to be constant at $6800^{+200^\circ}_{-800}$ K. They claim their data show a constant plateau of 6800°K with a shell-like structure of higher temperature around it. My data fall in the region of their "plateau."

Gordon and Meeks (ApJ 152, 417, 1968), with a 2½' half power beam width at 7.8 gHz, get the following values:

(1)	Trapezium	6610 ±400°K
(2)	3' N. of Trap.	4060 ±330°K
(3)	2½'S. of Trap.	4730 ±380°K

that is, a decrease away from the Trapezium.

Mills and Shaver (Aust. J. Phys. 21, 95, 1968), with a 3' half power beam width at 408 MHz., obtain a contour map in temperature which shows a decrease away from the Trapezium. The full width at half maximum is 370 arc seconds in the north-south direction corrected for the beam width. It is interesting to compare this number with the values obtained in Section H from the high frequency radio measurement and the infrared line measurement. The much larger width of this measurement is probably because the large "optical depth" at this frequency does not permit seeing deep into the nebula.

It should be noted that the half power beam width of these radio observations is of the order of the size of the region of the increasing T_e suggested by the infrared data. Thus, a possible explanation of the discrepancy is that the radio beams smooth over the small region near the center where the temperature is increasing outward and emphasize regions at greater distance from the center where the temperature is decreasing outward. Dieter (ApJ 150, 435, 1969) has made the point that the half power beam width can be different for the line and continuum if the electron temperature is changing within the beam width. Thus, there could be systematic errors in the radio data outside of the statistical ones quoted.

Experimental visual data on temperature variations is rather sparse and also inconclusive. Because of the large absorption, the temperatures are indicative only of the regions of the nebula nearest the sun. Dombrovsky (Publ. Leningrad Astr. Obs. 15, 166, 1950) finds cont/H_B increases away from the Trapezium. Gurzadin (Ann of Burakan Obs. 16, 3, 1955) finds cont/H_β decreases away from the Trapezium. Pottash (Vistas in Astr. 6, 149, 1965) has analyzed data by Osterbrock & Flather (ApJ 129, 26, 1959) on forbidden oxygen transitions and has obtained the following temperature values:

Distance from Trapezium	T_e(°K)
0'.1	9900
0'.9	9300
2'.3	8700
3'.9	8300
10'	8600

He cautions, however, that the result will be affected by possible errors in the collision cross section or the O/H ratio. Increasing O/H by a factor of 2 would decrease the temperature gradient by 40%.

Reitmeyer (ApJ 141, 1331, 1965) shows a temperature decreasing away from the Trapezium. The work is of poor spatial resolution and contains calibration errors.

In general, the visual data may be said to agree with the results of Mills and Shaver at 408 MHz. That is, on the near side of the nebula, the temperature shows a decrease at greater distances from the Trapezium. This is not in contradiction with the infrared model.

K. Comparison of Electron Density

At present, there exist two independent methods of determining the electron density: the ratios of some forbidden lines are relatively independent of temperature, but still are density dependent; the strength of the hydrogen lines are dependent on the square of the average electron density, as given in Equations 1 and 11.

To obtain the electron densities from the emission measures, it was necessary to first remove a factor of depth in line of sight. The only way this could be obtained while still preserving the independence of the forbidden line data was to assume that the circular symmetry shown in radio maps projected into a spherical symmetry in three dimensions. From the measurements of Schraml and Mezger (ApJ 156, 269, 1969), the half power nebular widths in different directions range from 2.6' to 3.5'. Thus the expected error in the depth scale from nonsymmetry is of the order of 30%. The defined radius of the emitting region is then fixed by the physical information desired. In this case, it was desired to select a radius which would be large enough to include most of the flux from the nebula (approximately 70%), yet not be so large as to include the extended low electron density cloud which seems to surround the core region. From the discussion of Schraml and Mezger, the contour interval at 10% of maximum on their map was selected as satisfying this criterion, and a radius of the central region of 4' (o.58 pc) was used. N_e was then calculated from

$$(23) \quad \log N_e = \frac{1}{2} \log E_m - \frac{1}{2} \log(2 R_N) - \frac{1}{4} \log\left[1 - \left(\frac{R}{R_N}\right)^2\right]$$

where Em represents the emission measure (cm^{-6} pc), R_N is 0.58 pc, and R is the radius at which the emission measure was obtained.

The available data are summarized in Figure 19. The most striking feature initially is that the forbidden lines give a density an order of magnitude higher than the hydrogen lines. To make the determinations agree, the nebula would have to be a thin sheet, 1/100 thick as it is wide. This is not a likely possibility. An alternative, already discussed by Osterbrock and Flather (ApJ 129, 26, 1959), is that the nebula has large density fluctuations. This is in agreement with the observation by Wilson et al. (ApJ Suppl. IV, 159, 1959) that large, randomly oriented velocity gradients exist in the nebula.

In comparing the emission measures from this paper with that of Mendez (Bol. de Los Obs. Ton. y Tac. 4, No. 28, 91, 1967), the same value of R (0.58 pc) has been assumed in Figure 19. The major differences can be ascribed to the different methods of data reduction. Statistical errors are small, of the order of .02 in the logarithm, and systematic errors are not likely to affect the relative curve shapes. Mendez had no high resolution radio data, so he assumed a uniform electron temperature of 10,000°K. The curve from this paper would agree in slope with Mendez' if a uniform temperature had been assumed, and Mendez' curve would agree in slope with the curve from this paper if he had determined temperatures from the radio data. The flatter density distribution is to be preferred, since its basis lies more securely in experimental data than in theoretical assumptions.

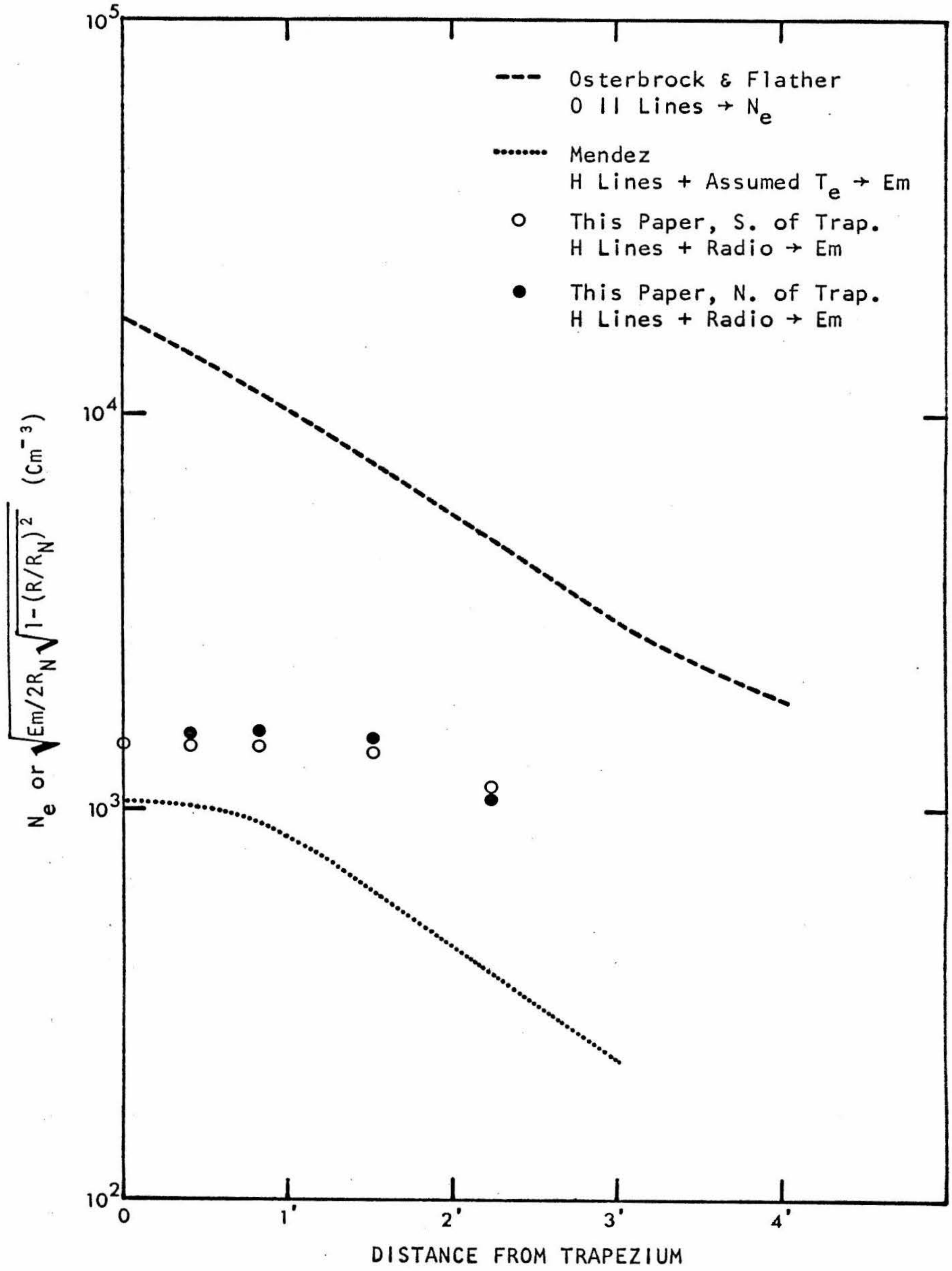

FIGURE 19 ELECTRON DENSITY VS. DISTANCE FROM TRAPEZIUM

The difference in absolute units near the Trapezium can be explained by considering that Mendez' emission measures were not corrected for reddening, since he used them to derive the reddening.

A comparison between the infrared determined density distribution and that from the forbidden lines would indicate that the inhomogeneities decrease outward for at least the first 2' from the Trapezium. Mendez claims his data show the inhomogeneities increase outward. Since either case could be explained by conditions existing before the formation of the Trapezium stars, little can be said as to which is more likely from the physical standpoint. Radio line widths (Gordon and Meeks ApJ <u>152</u>, 417, 1968) suggest that turbulence increases away from the Trapezium, but the data are taken over a larger region than is covered here.

L. T_e and N_e in Planetaries

The Brackett Gamma line measurements of NGC 7027 and IC 418 permit a determination of the electron temperature and emission measure by a method similar to that used in Section H. For the radio flux, values measured by Ehman (Priv. Com. to Terzian, "Planetary Nebulae" IAU Symp. No. 34, p. 87, 1967) at 8 gHz were used. Table 17 lists the object, assumed angular radius, the radio flux, the Brackett Gamma flux corrected for reddening, the derived temperatures, the derived emission measures, and the derived electron densities. The emission measures depend on the assumed angular diameters and are thus somewhat difficult to interpret in terms of real electron densities. For IC 418, the angular radius is assumed to be as given by Wilson and Aller (ApJ 114, 421, 1951). For NGC 7027, the angular radius of 7.1" is from O'Dell (ApJ 135, 371, 1962) and that of 6.0" is from Thompson et al. (ApJ 148, 429, 1967). Note that the derived temperatures and emission measures are higher than for the Orion Nebula (Table 12), although IC 418 is not as different as NGC 7027. To obtain the electron densities, it was necessary to assume distances to the nebulae. O'Dell (ApJ 135, 371, 1962) obtains values of 1900 pc. for IC 418 and 1800 pc for NGC 7027 from the flux in H_β and the angular diameter.

The distances to the nebulae were combined with the angular radii to give physical radii. Average depths-in-line-of-sight of $\sqrt{2}$ times the physical radii were then combined with the emission measures to obtain the electron densities. The error is primarily in the unknown distances to the nebulae, probably good to about 50%.

TABLE 17

DERIVED ELECTRON TEMPERATURE AND DENSITY FOR PLANETARY NEBULAE

Object	Assumed Radius	Flux ($W\ M^{-2}\ Hz^{-1}$) 8.0 GHz	Flux ($W\ M^{-2}$) B_7	T_e (°K)	Em ($Cm^{-6}\ Pc$)	N_e (Cm^{-3})
IC 418	6.2"	1.75×10^{-26}	1.45×10^{-14}	$11{,}400\pm^{7200}_{4600}$	$7.6 \times 10^{6}\pm^{1.4}_{1.1}$	3.1×10^{3}
NGC 7027	6.0"	6.20	3.38	$20{,}300\pm^{3100}_{2800}$	$35.1 \times 10^{6}\pm^{1.8}_{1.7}$	6.9×10^{3}
NGC 7027	7.1"	6.20	3.38	$20{,}300\pm^{3100}_{2800}$	$25.0 \times 10^{6}\pm^{1.3}_{1.2}$	5.3×10^{3}

M. Comparison of T_e and N_e for Planetaries

Because the planetaries are harder to measure, there has been less work done on determining their electron temperatures and densities than for the Orion Nebula. An examination of the few outside determinations which do exist is still worthwhile, however. These are summarized in Tables 18, for T_e, and 19, for N_e.

Comparing Table 19 first with Table 16 for the Orion Nebula, it is seen that (1) the temperatures are generally similar for similar methods for IC 418 and generally higher for similar methods for NGC 7027; and (2) the various methods for a given nebula produce the same relative high or low temperatures. Point (1) is in agreement with the relative temperatures measured for the Orion Nebula and the two planetaries by the infrared line plus radio continuum method. Point (2) suggests that the differences in the values obtained are caused either by incomplete theoretical treatment, or by temperature fluctuations which are weighted differently by the different methods. It is not likely that errors in data would throw all three points off in the same direction for a given determination. The analysis of the relative merits of the various methods of temperature determination has been discussed in Section I and will not be repeated here.

Turning to Table 19 and comparing it with Figure 19 and Table 17, it is seen that for the planetaries the electron density determined by the O II lines is in generally good agreement with that determined

TABLE 18

SUMMARY OF OTHER DETERMINATIONS OF T_e FOR PLANETARIES

Nebula	T_e	Method	Reference
IC 418	2,500°K	Balmer Decrement (High n Lines)	Kaler (ApL 1, 227, 1968)
	4,800°K	Balmer Cont./H_β	Lee (ApL 1, 225, 1968)
	7,100°K	Free-Free Continuum Shape (Radio)	Thompson (ApL 1, 25, 1967)
	9,500°K	O III Line Ratios	Schmitter and Millis (ApJ 149, 721, 1967)
	11,200°K	O III Line Ratios	Kaler (ApJ 143, 722, 1966)
	12,500°K	Free-Free T_B At 408 MHz	LeMarne and Shaver (Proc. ASA 1 (5), 216, 1969)
NGC 7027	$\leq$ 1,000°K	Balmer Decrement (High n Lines)	Kaler (ApL 1, 227, 1968)
	$\leq$ 3,000°K	Balmer Cont./H_β	Lee (ApL 1, 225, 1968)
	13,900°K	O III Line Ratios	Kaler (ApJ 143, 722, 1966)
	16,000°K	O II & N II Line Ratios	Seaton (Repts. on Progr. Phys. 23, 313, 1960)
	16,500°K	O III Line Ratios	

TABLE 19

SUMMARY OF OTHER DETERMINATIONS OF N_e OR Em FOR PLANETARIES

Nebula	N_e (Cm^{-3})	Source	Reference
IC 418	4.2×10^4	O II Lines	Kaler (ApJ <u>143</u>, 722, 1966)
	2.1×10^4	Emission Measure	Aller ("Landolt-Börnstein Tables, Zahlenwerte Und Funktionen, Band: Astr. U. Astrophysik" Springer-Verlag, 1965)
NGC 7027	6.6×10^3	O II Lines	Kaler (ApJ <u>143</u>, 722, 1966)
	9.8×10^3	Emission Measure	Aller (loc. cit.)
	2×10^4	Emission Measure	Seaton, (Repts. on Prog. Phys. <u>23</u>, 313, 1960)
	38×10^6*	Emission Measure	Terzian (Planetary Nebula IAU Symposium No. 34, p. 87, 1967)

* Em, not N_e

by the emission measure, unlike the Orion Nebula. This would suggest that contrary to the visual appearance, density fluctuations are not as severe in the planetaries.

IV. CONTINUUM ANALYSIS OF M 42

A. Chapter Introduction

The preceding chapter, treating the line analysis, involved relatively straight-forward theoretical considerations. This was primarily because it could be assumed that the emission of a given line was produced entirely by a single atomic species and by a single mechanism. This is not the case in this chapter. Among the sources which could contribute to the continuum, and which must be examined, are (1) unresolved infrared stars; (2) helium free-free, bound-free, and 2 quantum radiation; (3) hydrogen free-free, bound-free, and 2 quantum radiation; (4) H^- radiation; (5) dust thermal emission; (6) dust scattering of starlight; (7) electron scattering of starlight; and (8) synchrotron emission.

To unravel the relative importance of these various sources is not a simple process. The approach which has been taken has been to compare data on the spatial and frequency variations of the radiation intensity with theoretical predictions. Despite the hazards of such an approach, it is felt that a reasonable model of the physics of the nebula has been obtained. Thus, while the previous chapter stressed the physical conditions which could be determined, the present chapter stresses the physical processes which can be determined.

The continuum data to be used is drawn from the spectroscopy results of Table 2 (both the equivalent width and the continuum are used) and from the photometry results of Table 5. As will be recalled, the photometry data at different positions averaged to give regions roughly comparable to the three inner regions of the spectroscopy. Since the continuum data of Tables 2 and 5 have been reduced independently, a comparison is worthwhile. To first order, the numbers should agree, and they do. The slight differences may be explained by an incomplete agreement in the area represented and also by the inclusion of the line flux in the photometry data.

Synchrotron radiation and unresolved infrared stars are initially eliminated as possible sources of the continuum. The next step is to show that the hydrogen and helium recombination radiation does not fully account for the infrared radiation. The excess may conveniently be divided into long wavelength infrared and short wavelength infrared at two microns. The long wavelength infrared excess can be shown to be dominated heavily by dust emission and, this is used to derive some properties of the dust.

Also of interest is the short wavelength infrared excess which is reported here for the first time. Dust emission can be ruled out, as can H^- emission. This leaves a choice of (1) some previously unknown mechanism, (2) dust scattering, or (3) electron scattering. The best choice is scattering by the dust.

The thesis would be incomplete without some discussion of the infrared nebula north of the Trapezium, so this is included as the final topic of the chapter.

B. Synchrotron Emission or Infrared Stars?

The basic argument against synchrotron emission is that the radio spectrum is well accounted for by other means. A comparison of H_{α} line intensities and the radio flux by Pottash (Vistas in Astr. 6, 149, 1965) shows agreement with a thermal spectrum to 2%. It is not considered likely that the synchrotron process could operate in the infrared without being detectable at other wavelengths.

Unresolved infrared stars could provide a background of virtually arbitrary spectral shape. The argument used against them thus cannot depend only upon the spectral distribution. The spatial distribution, however, does provide a fairly plausible argument. The essential argument is that lack of large intensity fluctuations in high resolution spatial scans provides an upper limit to the infrared star density which is too large to be realistic.

A series of spatial scans in the 2.2 μ band were taken on the 60 inch telescope at Mount Wilson on the night of 22 Jan 1968 with a 12" diameter aperture. Figure 20 shows one of these East-West scans, taken 20" south of ORS-1, that is, approximately midway in declination between ORS-1 and the Trapezium stars. The peak to the left of center is a star. The noise is of the order 2.5×10^{-19} wm^{-2} $\mathrm{H_z}^{-1}$ Ster^{-1}. From the lack of fluctuation in the traces, a minimum of at least two stars per beamwidth would have been necessary to produce the observed flux. If a depth-in-line-of-sight of 0.33 pc, corresponding to 3 arc minutes projected on the nebula, is assumed, the infrared

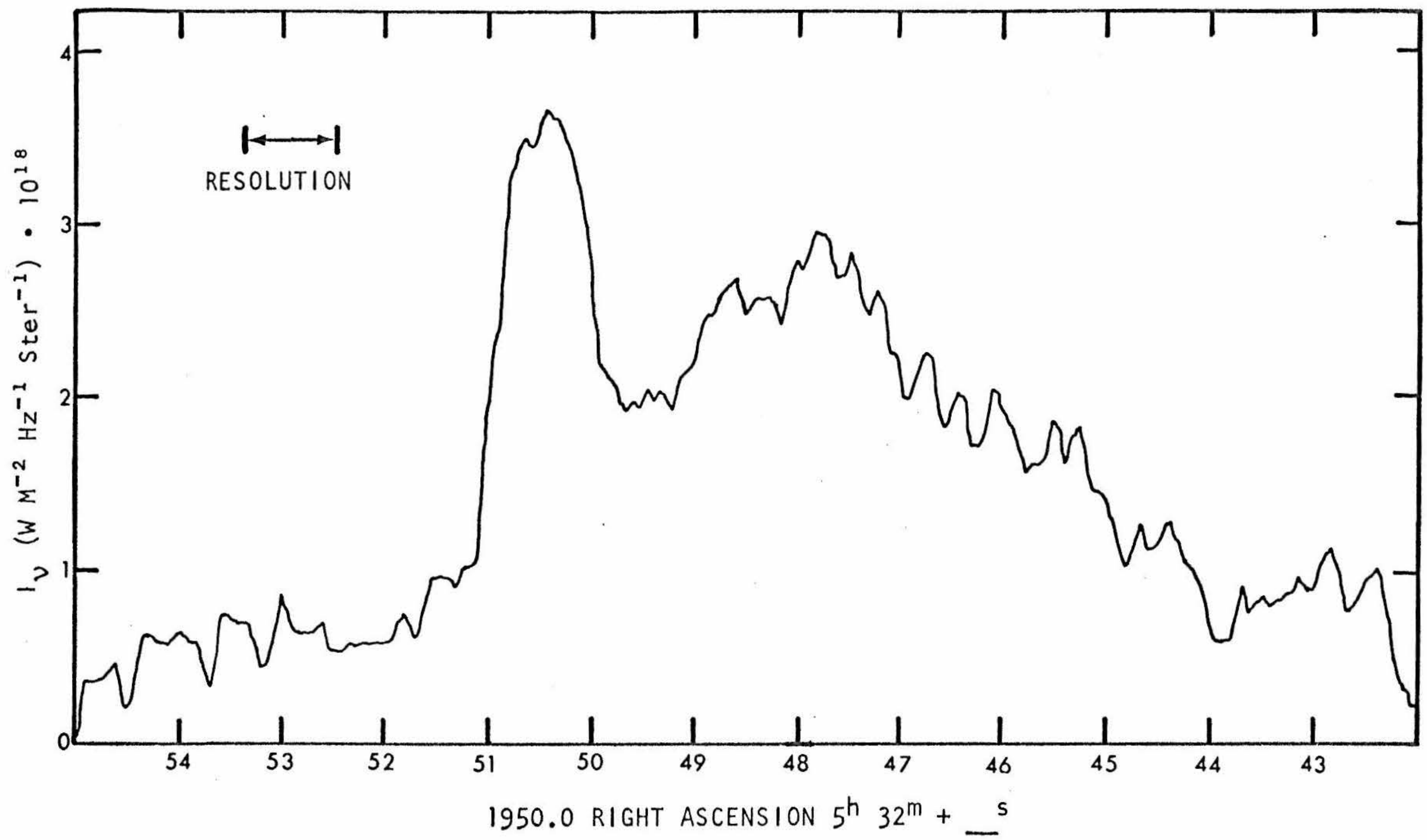

FIGURE 20 SPATIAL SCAN ACROSS ORION NEBULA

star density would be of the order of 10^4 stars/pc^3. This is greater by an order of magnitude near the Trapezium (Johnson, H. M., Pub AsP 73, 147, 1961).

From the supposed density of these infrared stars, the observed flux, and the distance to the Nebula, a very rough luminosity and color can be derived. Since the spectrum of the excess appears flat, the hypothetical stars will be assumed to be at a temperature around 1300°K. From the observed flux and the assumption of two stars per beamwidth it is then possible to calculate that the luminosity would have to be about 10^{27} wm^{-2} or three solar luminosities. Even with the large errors, these hypothetical infrared stars would fall in the "protostar" region of the H-R diagram, more than doubling the number of such stars now known or suspected.

While neither the star density nor color-luminosity arguments is totally convincing, it is felt that they cast enough suspicion on the infrared star hypothesis to make its acceptance at this time unlikely. It should be pointed out that the question could be decided on larger telescopes in that either the limits would be stretched to total implausibility, or infrared stars would be found.

C. Infrared Excess Emission in M 42

As can be seen from the preceding chapter, recombination radiation is well enough understood that it can be used to derive some of the physical properties of the nebula. Hydrogen and helium recombination can thus here be regarded as established contributions, and subtracted from the continuum total.

Unlike the visual and radio regions, the infrared regions of the spectrum contain important contributions from all three of the recombination continuum mechanisma. As a sample of the type of output which was used to obtain the excess continuum, Figure 21 shows the predicted continuum spectrum and the various contributions for $0.16 \leq \lambda^{-1} \leq 1.25$ (microns^{-1}) at an electron temperature of $9,000^{\circ}$K and assuming NHe II/NH II = 0.10, NHe III/NH/ II =0.03. The emission measure and reddening factors have been left out as in Table 7. As a check, the values of the various contributions calculated for $10,000^{\circ}$K were compared with Seaton's (Rept. on Prog. Phys. 23, 313, 1960) predicted values. At wavelengths where the calculations overlapped, the agreement was good to 5%.

One of the primary reasons for obtaining the infrared spectra was to use the property that a knowledge of the line intensity allows an accurate prediction of the continuum intensity from recombination. That is, the infrared line to continuum ratios (equivalent widths) are fixed only by the electron temperature, which is known to a few thousand degrees. Figures 22-27 show the predicted ratios for

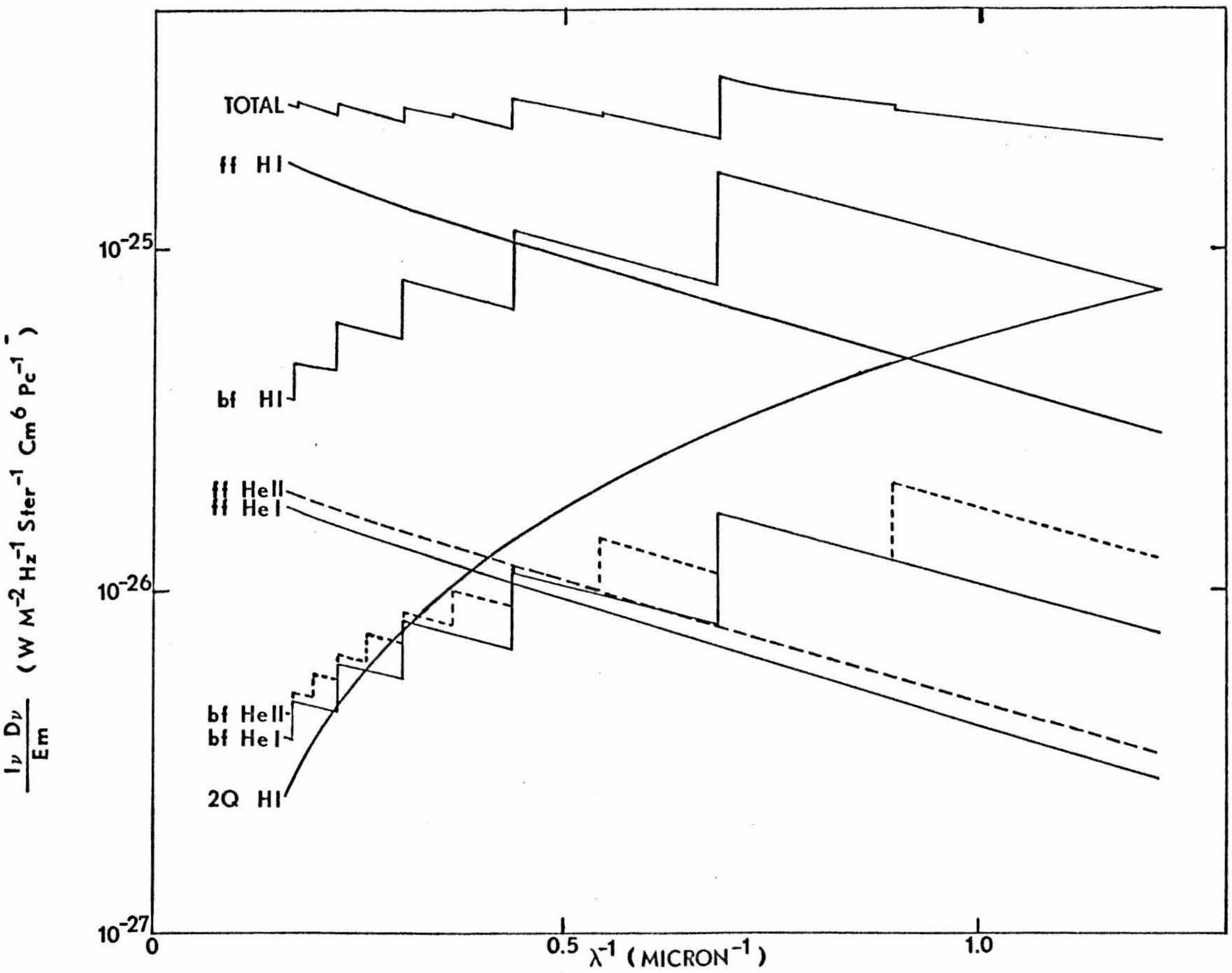

FIGURE 21 PREDICTED INTENSITIES FOR T_e = 9000°K

various temperatures (graphed as 1/equivalent width to indicate the continuum excess directly) along with the experimental points for the six regions in which spectra were taken. It should be noted that these experimental numbers are virtually free of systematic effects such as reddening, absolute calibration, etc. For any reasonable choice of electron temperature, it is seen that there is some excess for most of the data. None of the data have a smaller continuum than predicted. The regions of the Trapezium and the red star have had the stellar continuum flux subtracted before their ratios were formed (see Table 4), so the excesses are representative of the nebula, not the stars.

Table 20 shows the excess at each position for an assumed electron temperature of 8000°K. The 1.6 micron data have been averaged for the five lines. The principal features of the table to be noted for later interpretation are that (1) the ratios peak at the Trapezium for the 1.6 μ band, but at the red star for the 2.2 μ band; (2) the absolute amounts of the excesses are peaked at the Trapezium in both cases; (3) the 2.2 μ band shows a larger absolute excess North of the Trapezium than to the South (in fact, there is no excess 135" South), while the 1.6 μ band shows no significant difference between north and south; (4) if a representative distance of 100" is taken for the Dark Bay, it appears to be a region more characteristic of the south end than the north end of the Nebula. An interpretation of these features will be reserved until after the other methods of demonstrating the excess have been discussed.

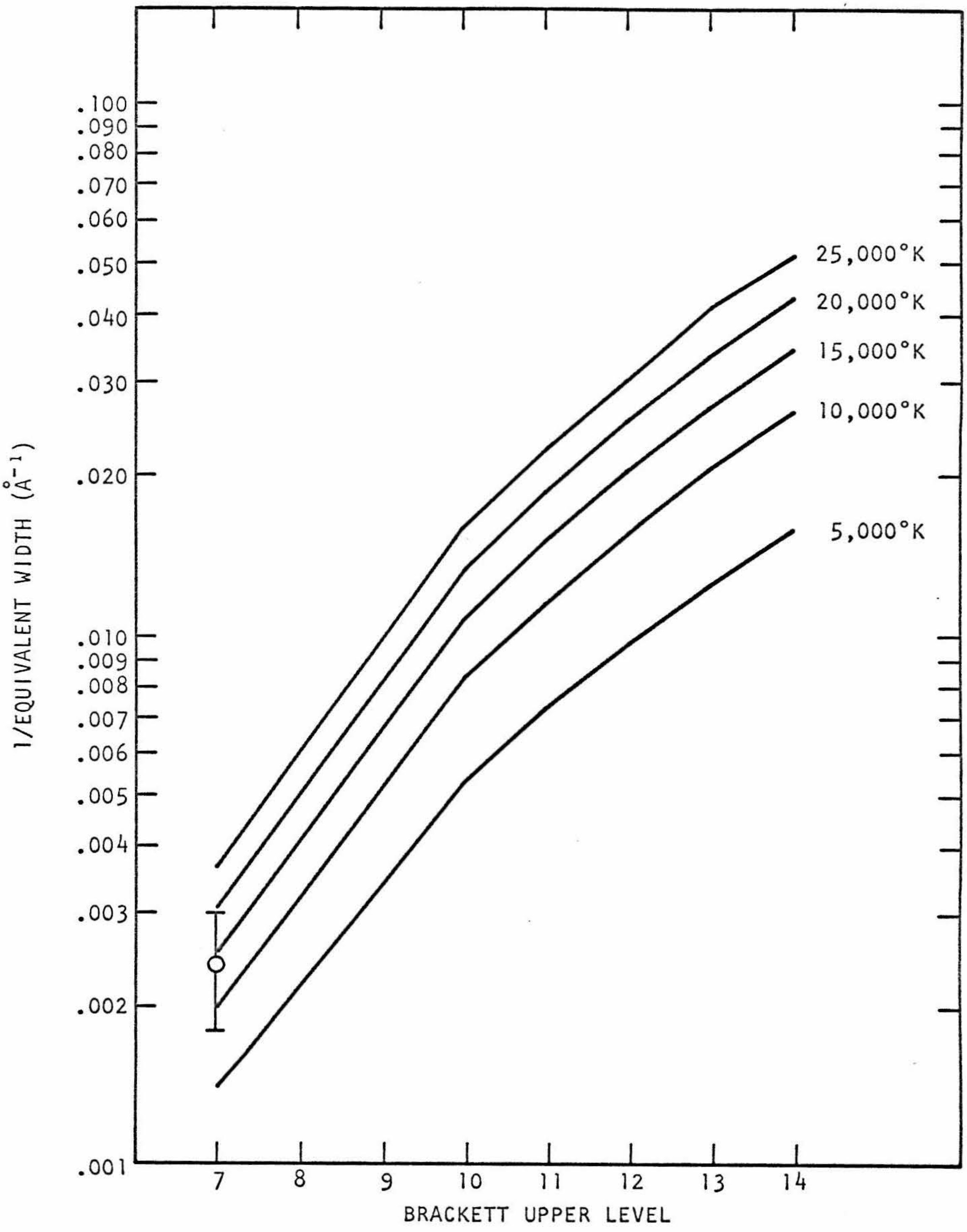

FIGURE 22 DARK BAY

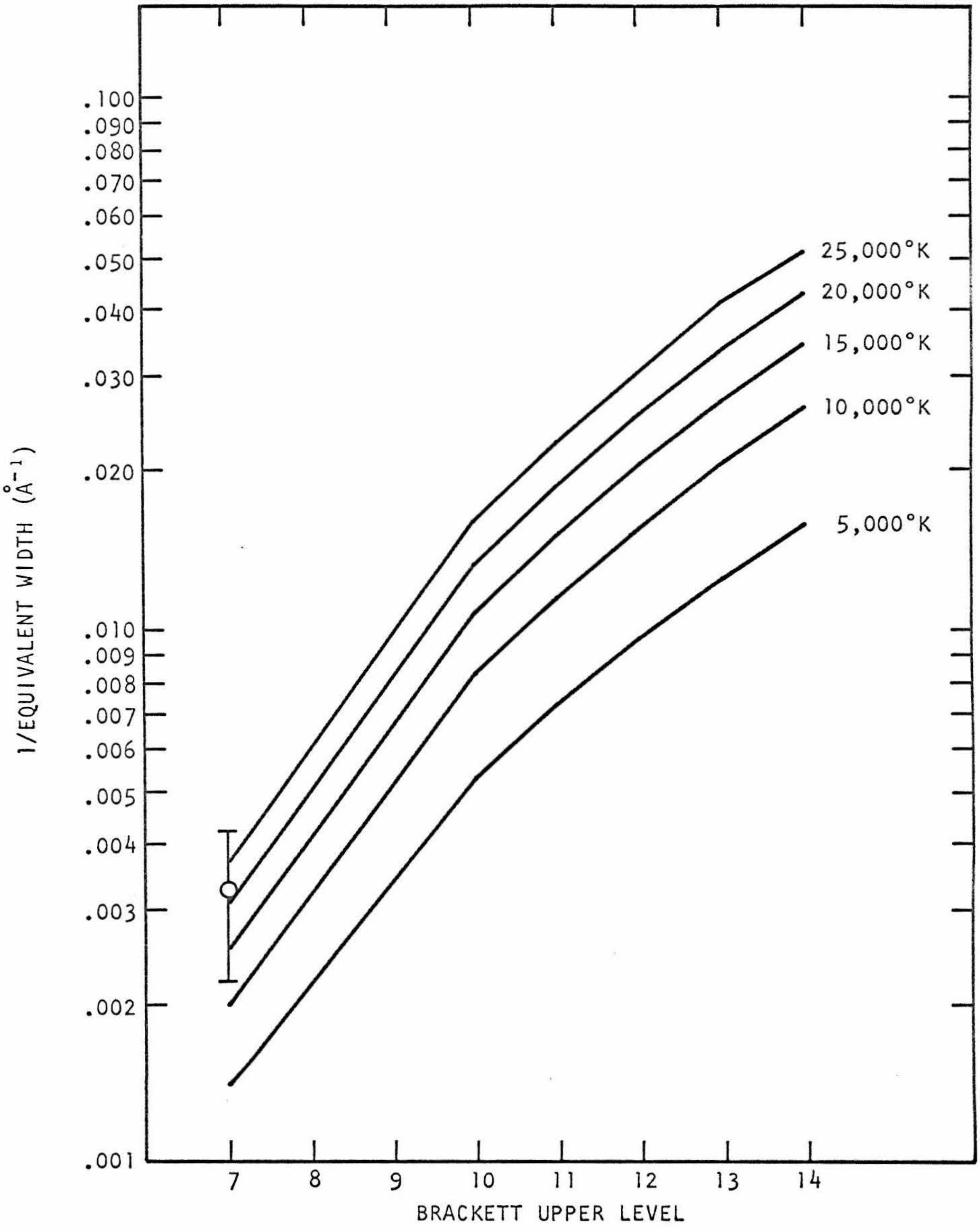

FIGURE 23 135'' NORTH OF TRAPEZIUM

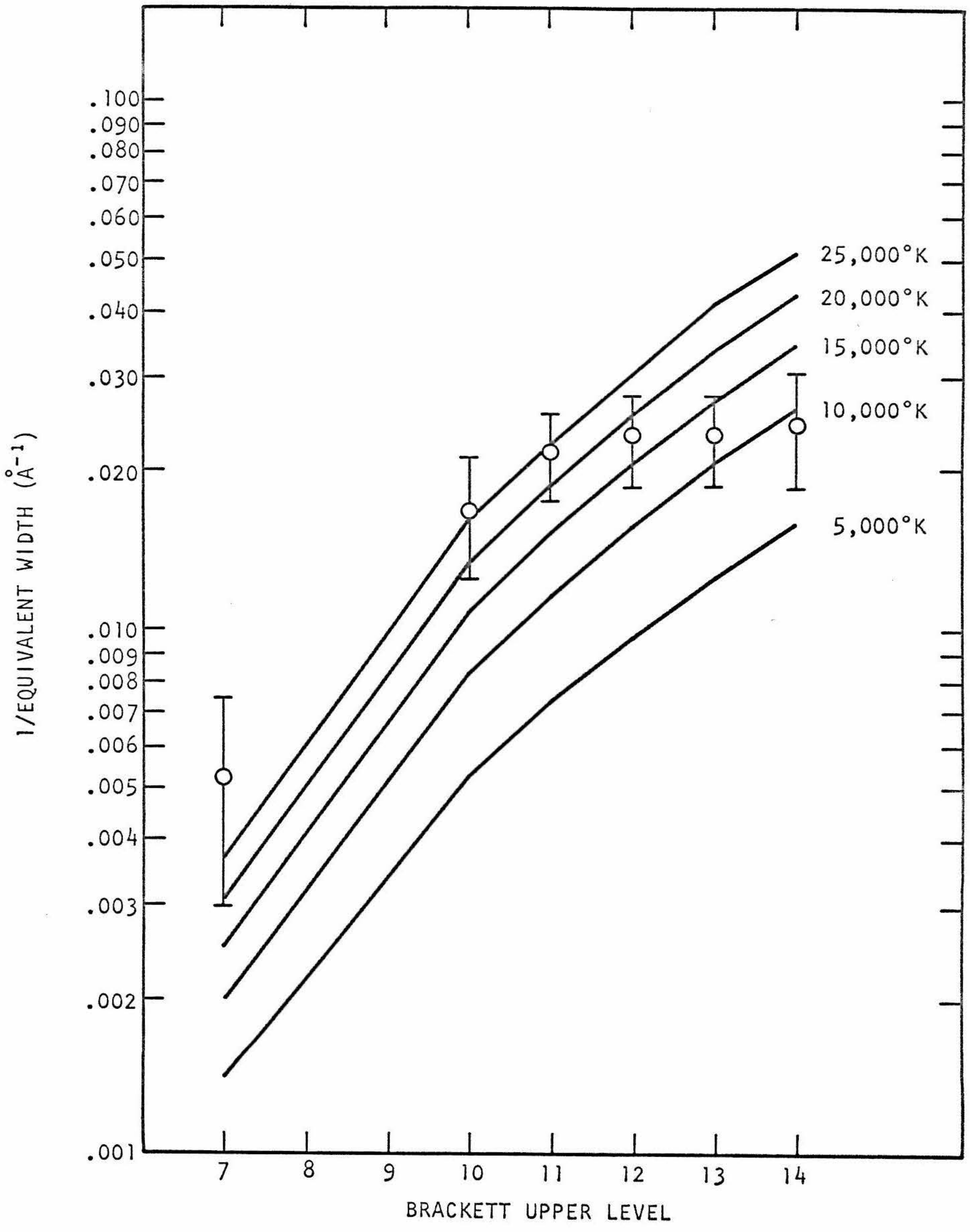

FIGURE 24 50'' NORTH OF TRAPEZIUM

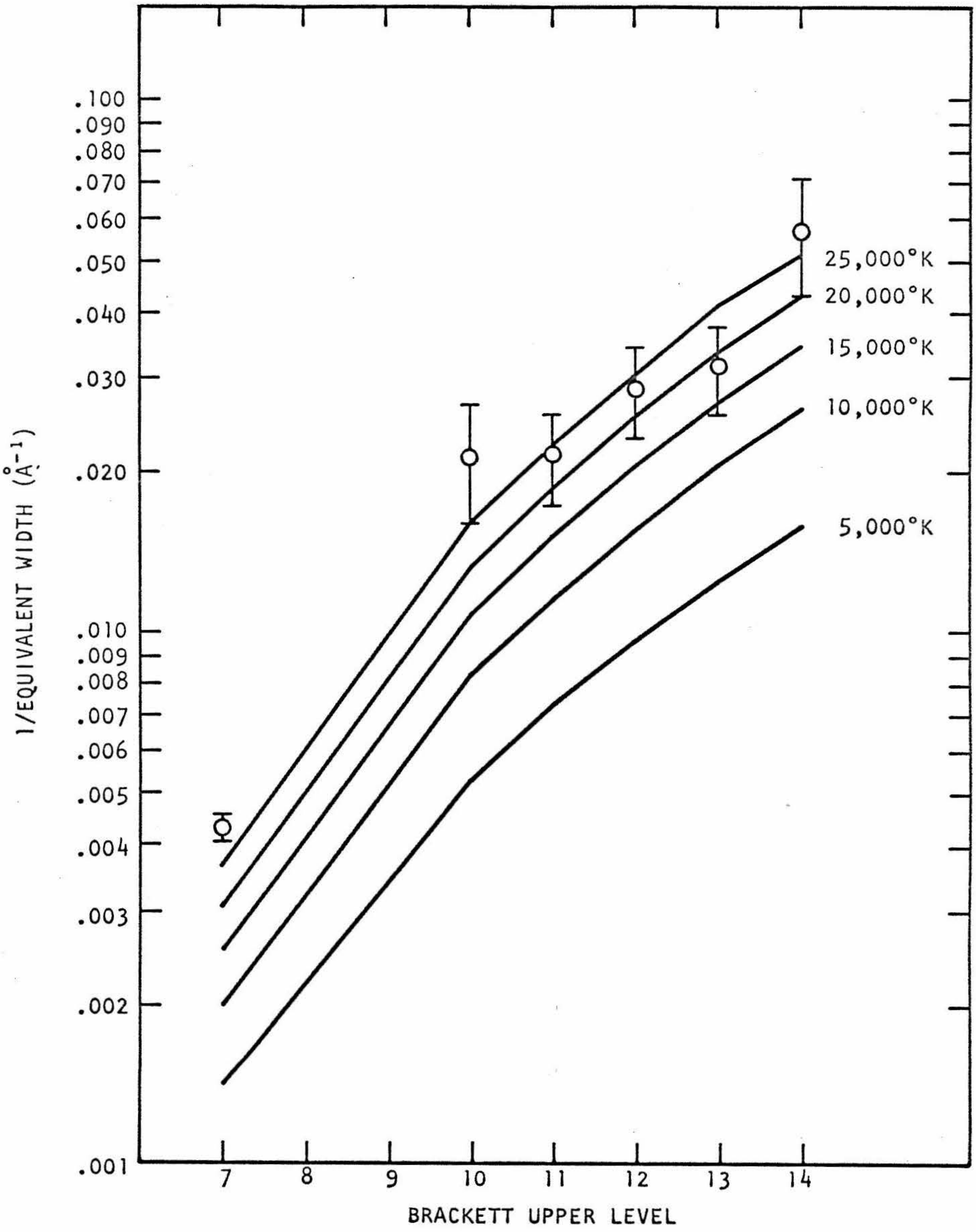

FIGURE 25 TRAPEZIUM

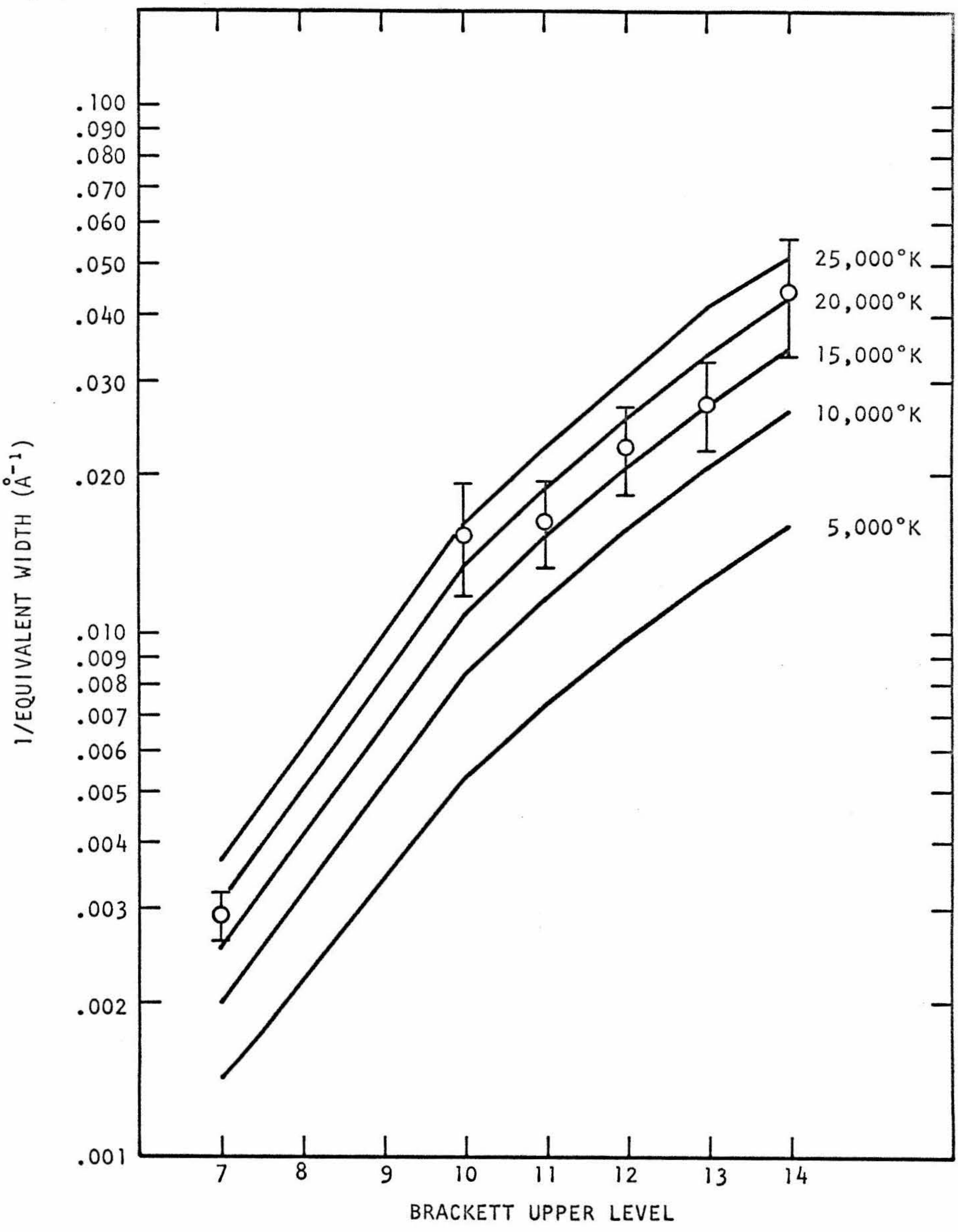

FIGURE 26 50'' SOUTH OF TRAPEZIUM

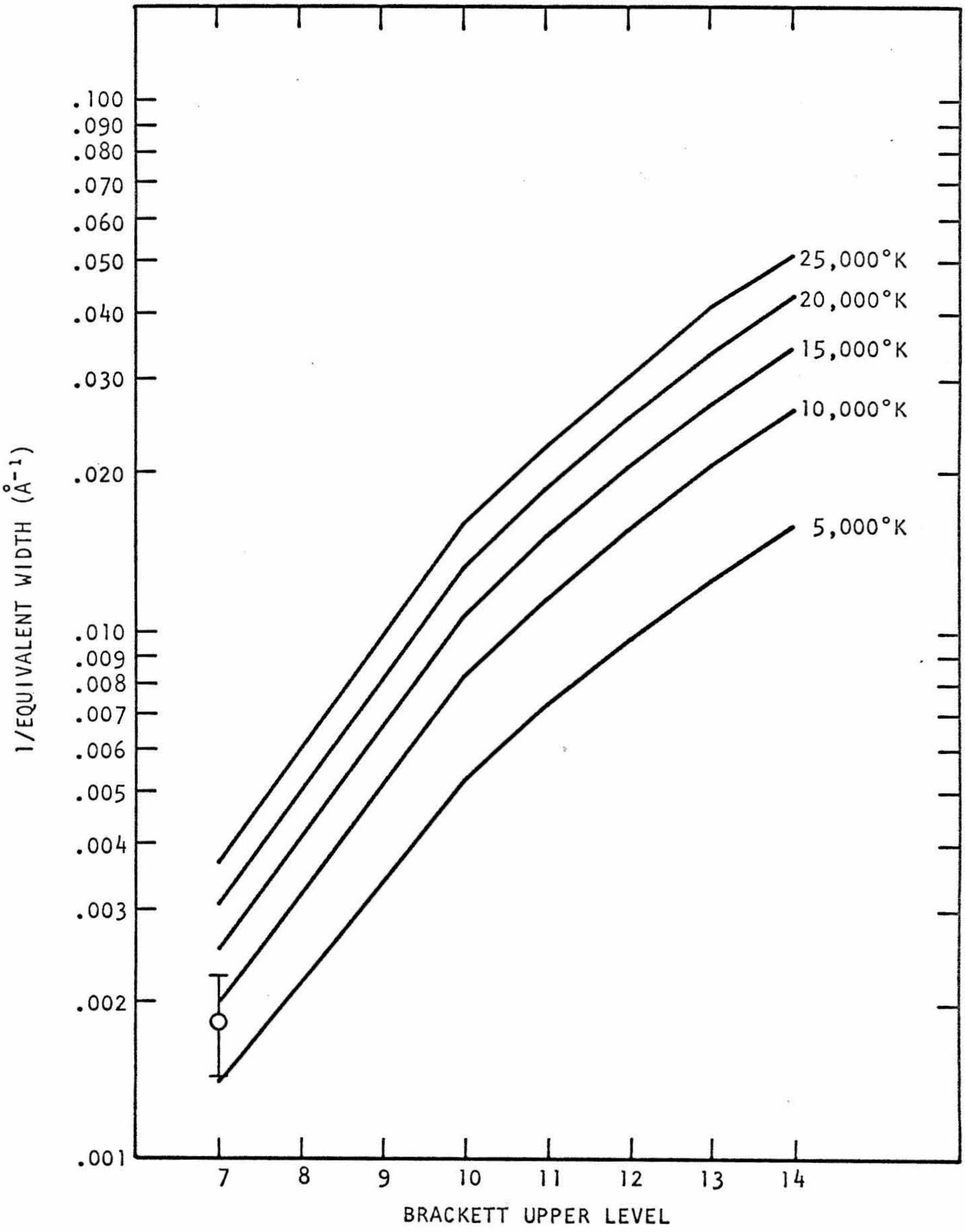

FIGURE 27   135" SOUTH OF TRAPEZIUM

TABLE 20

EXCESS CONTINUUM FROM INFRARED L/C METHOD

	2.2μ - Band		1.65μ - Band	
Position	Ratio To Predicted Continuum At 8000°K	Amount Of Excess Continuum (W M^{-2} Hz^{-1} Ster^{-1})	Ratio To Predicted Continuum At 8000°K	Amount Of Excess Continuum (W M^{-2} Hz^{-1} Ster^{-1})
(1) Dark Bay	1.4	.74 x 10^{-19}		
(2) 135'' NOT	2.0	2.34		
(3) 50'' NOT	3.0	10.0	1.7	3.5 x 10^{-19}
(4) Trapezium	2.5	13.6	2.3	10.4
(5) 50'' SOT	1.6	4.2	1.8	3.5
(6) 135'' SOT	1.0	.1		

The spectra provide still another method of obtaining the excess in the 2 micron band. This is to measure the Pfund Series discontinuity at 2.28 microns. Systematic effects are even less likely than in the line to continuum method, since continuum is compared with continuum and all spectrometer dependent factors should cancel. A comparison of the percentage discontinuity with theoretical predictions as in Figure 21 allows an estimate of the percentage of the continuum which is from recombination. Unfortunately, the faintness of the continuum makes this method much less accurate than the line to continuum method. This method is of such low accuracy that it has only been included for completeness.

The spectra were averaged in 500 A wide intervals centered at 2.252 microns and 2.310 microns, as given in Table 2. Table 21 shows the resulting percentage change and the predicted percentage changes at 8000°K and 10,000°K if the continuum were all recombination. Also shown is the ratio to predicted assuming 8000°K as in Table 20. With the large errors, about all that can be said is that these numbers are not in disagreement with the numbers of Table 20 for the 2.2 μ band and that the ratio numbers are more likely larger than 1 than they are equal to 1.

The third method of obtaining the excess is to predict the ratio of the radio continuum to the infrared continuum. Then the measured radio continuum can be used to predict the infrared continuum. Figures 28 and 29 show the predicted infrared continuum with assumed electron temperatures of 6000°K and 10,000°K, respectively. The

TABLE 21

EXCESS CONTINUUM FROM PFUND SERIES DISCONTINUITY

Position	ΔF_ν/Avg. F_ν	∇F_ν/Avg. F_ν Predicted For T_e = 8000°K	∇F_ν/Avg. F_ν Predicted For T_e = 10,000°K	Ratio Actual Continuum To Predicted Continuum For T_e = 8000°K
(1) Dark Bay	+0.26±0.25	+0.227	+0.179	1 -23
(2) 135'' NOT	-0.05±0.50			1 - ∞
(3) 50'' NOT	-0.02±0.20			1.3- ∞
(4) Trapezium	+0.02±0.10			1.9- ∞
(5) 50'' SOT	-0.05±0.20			1.5- ∞
(6) 135'' SOT	-0.45±0.50			4 - ∞

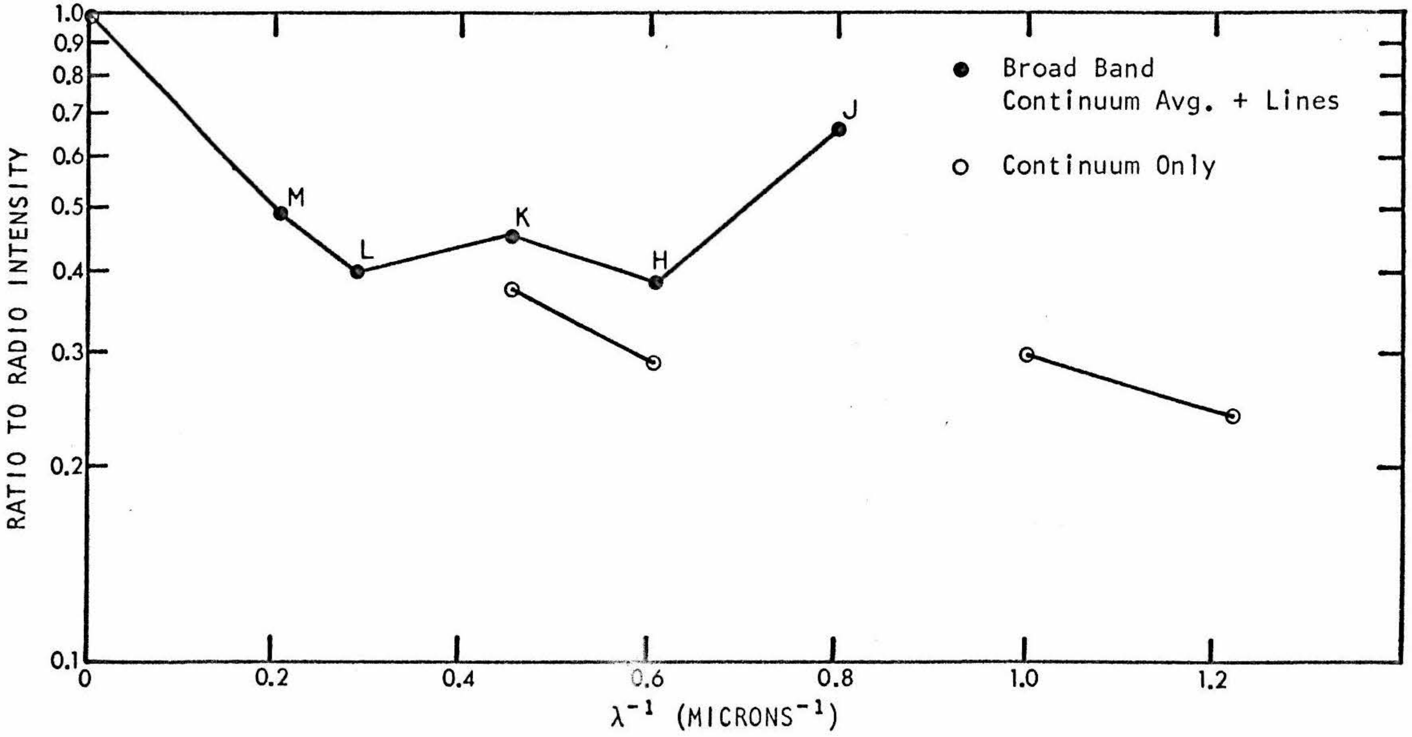

FIGURE 28 PREDICTED RATIOS OF INFRARED CONTINUUM INTENSITIES TO RADIO INTENSITY AT 15.375 GHz (T_e = 6000°K)

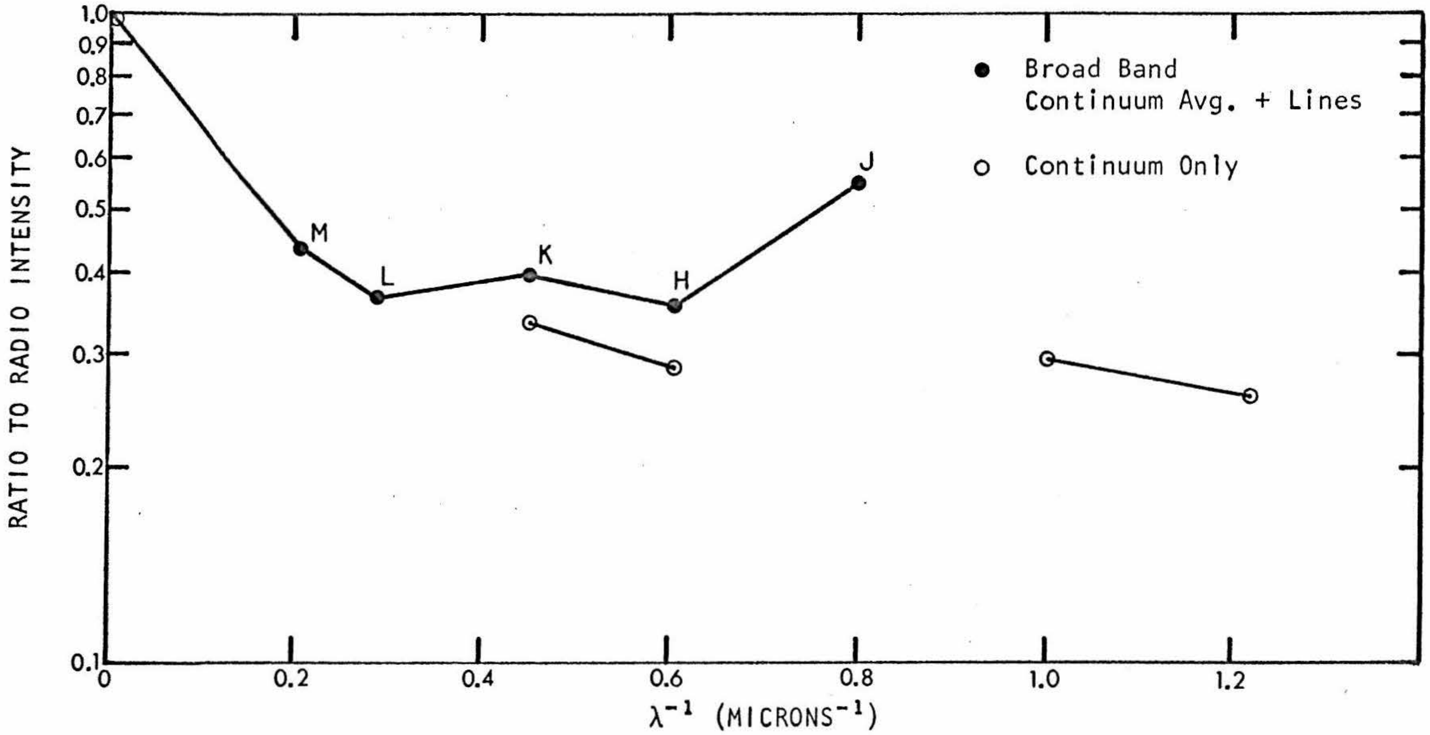

FIGURE 29 PREDICTED RATIOS OF INFRARED CONTINUUM INTENSITIES TO RADIO INTENSITY AT 15.375 GHz (T_e = 10,000°K)

predicted continuum values are for the broad band filter data. They have been obtained by averaging over the band (thus correcting for series discontinuities in the 2.2μ and 3.5μ bands) and adding in predicted line fluxes for H I, He I, and He II. The two additional points at the 1.6μ and 2.2μ bands are continuum only for comparison with the spectrometer measured continuum. The emission measure has been adjusted to give the same radio flux in both cases. It is clear from the two figures that the prediction is insensitive to temperature. For the remainder of this section, a temperature of 8000^{o}K will be assumed.

Taking the raw data of Table 5 and correcting for reddening of 10% at 2.2μ, 15% at 1.6μ, and 25% at 1.2μ as determined in Chapter III Section C, Figures 30-32 for the three central regions are obtained. Also shown in these figures are the predicted values at 8000^{o}K normalized to the radio intensity, and some longer and shorter wavelength outside data which will be needed for later analysis. The radio points at 15.375 gHz are from Schraml and Mezger (ApJ <u>156</u>, 269, 1969) and are the same as given in Table 12. The 11.6 and 20 micron points are from Ney and Allen (ApJ <u>155</u>, 193, 1969). The two points in the near infrared for the Trapezium region are from Mendez (Bol. de Los Obs. Ton. y Tac. <u>4</u>, no. 27, 41, 1965).

Two values, corrected for reddening, are shown for each wavenumber, using Mendez' derived reddening and using the reddening derived in this work. It is clear from these points why visual data have not been used to predict the infrared continuum.

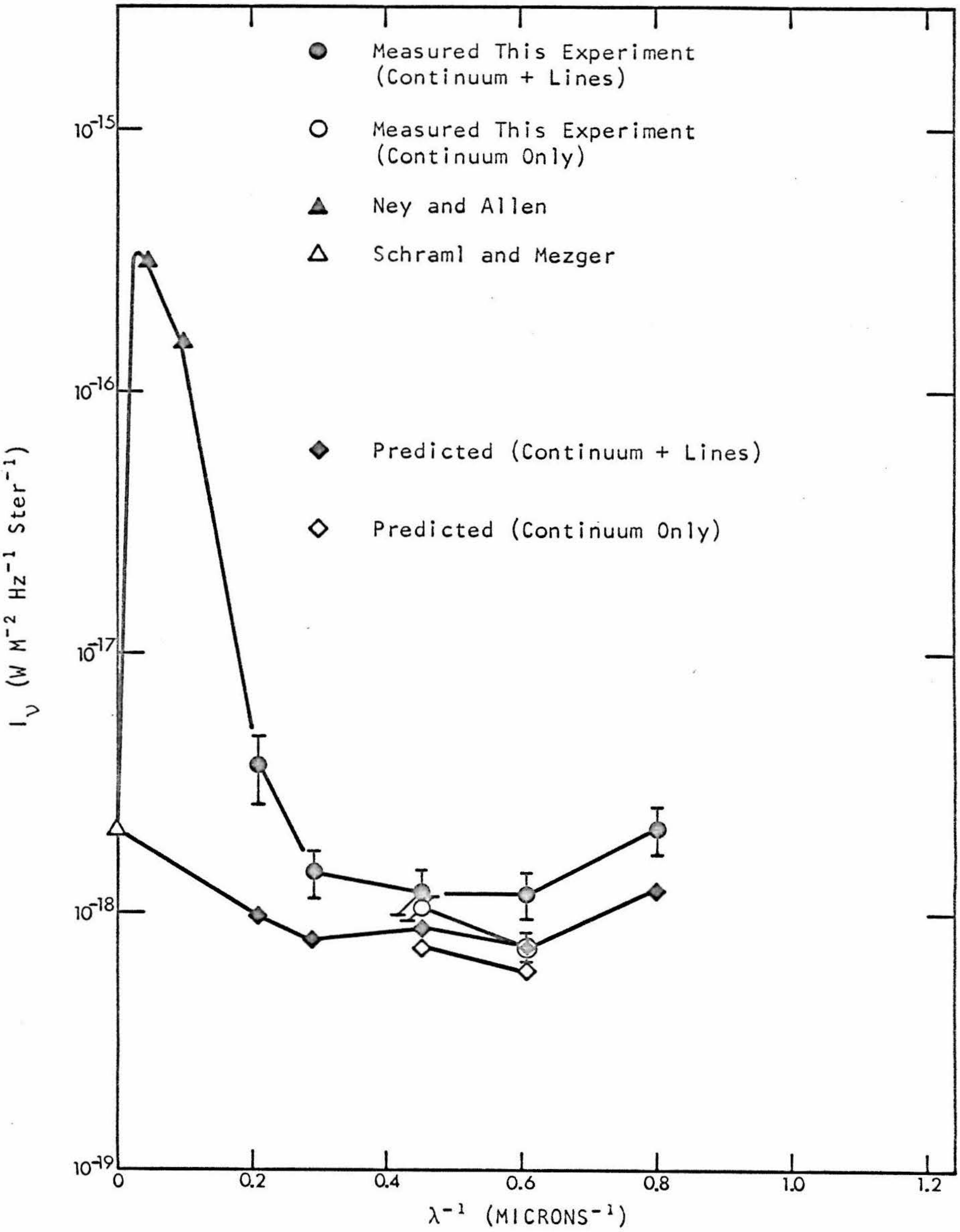

FIGURE 30 INTENSITIES FOR REGION 50'' SOUTH OF TRAPEZIUM

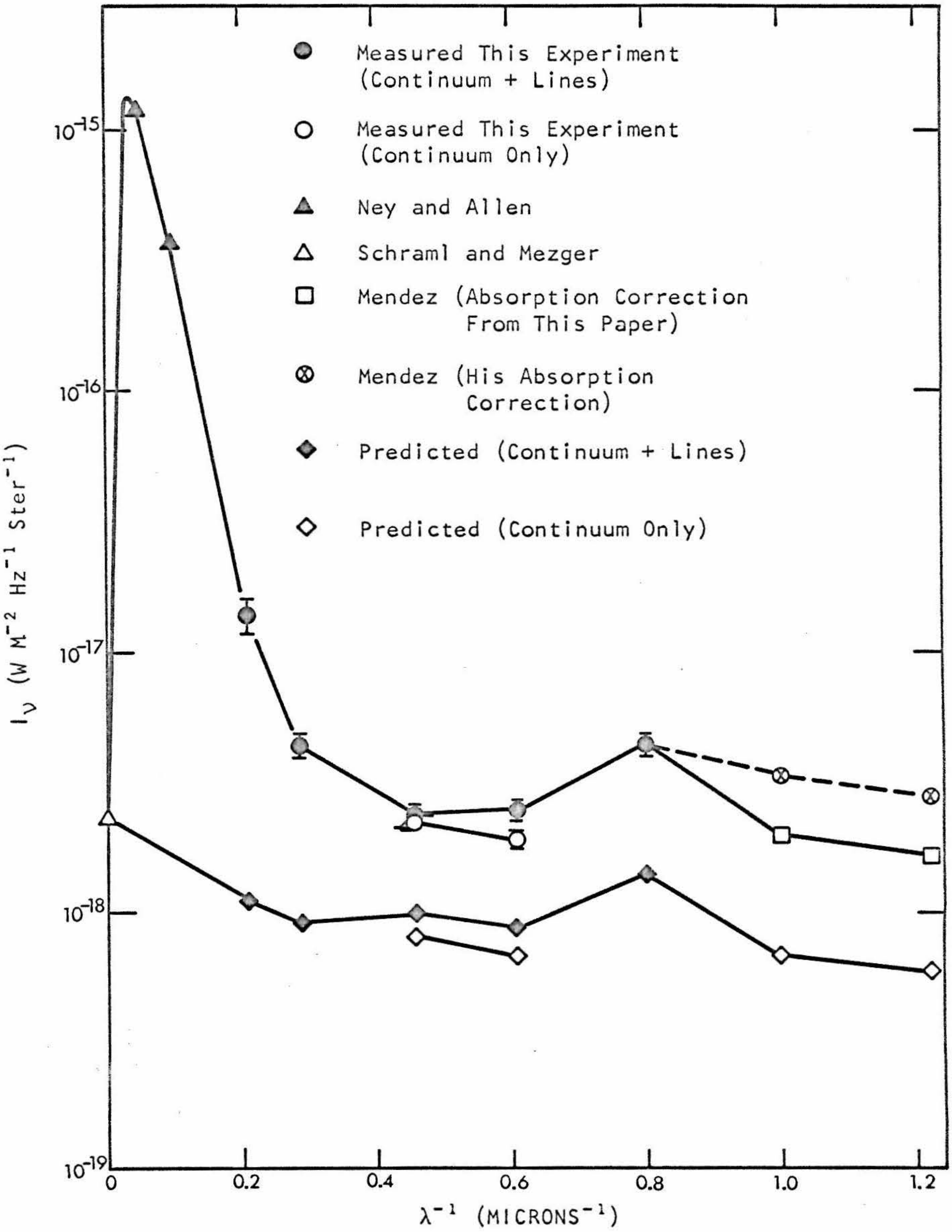

FIGURE 31 INTENSITIES FOR TRAPEZIUM REGION

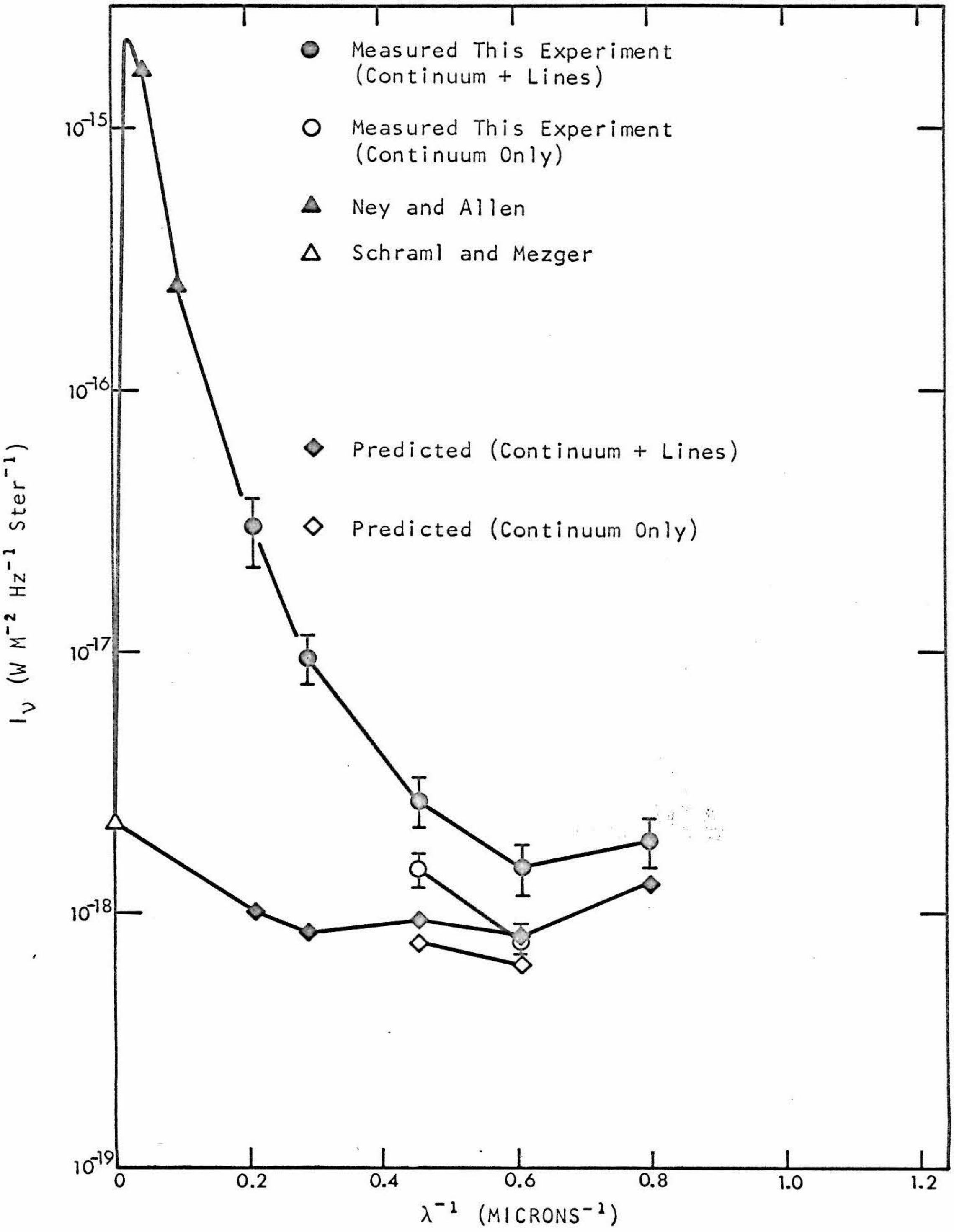

FIGURE 32 INTENSITIES FOR REGION 50" NORTH OF TRAPEZIUM

The data in Figures 30-32 have been used to calculate Table 22, which gives both the ratio excesses and the absolute excesses for the various wavelengths and bands considered. A comparison with Table 20 shows reasonable agreement for the 1.6 μ and 2.2 μ bands despite the virtually independent methods of arriving at the excess. Further discussion of the features of the excess will be left for the next section.

Some questions may be raised regarding the validity of the third procedure. Is it reasonable to extrapolate from the radio wavelengths to infrared wavelengths? How will the different spatial resolution of the infrared and radio data affect the conclusions?

From the theoretical standpoint, the first question is relatively easy to answer. Given that dust absorption has been well accounted for in the infrared, it remains only to show that self absorption is not significant in the radio regions. Since the same electrons are producing the radio and infrared recombination radiation, it is not likely that any other effect will change the radio to infrared ratio strongly. Qualitatively, it can be seen that self absorption is not serious since the kink in the radio spectrum which indicates the onset of strong self absorption comes at a frequency an order of magnitude lower than we used in the present calculations. See e.g. Terzian et al. (ApL 1, 153, 1968). An exact number for the "optical depth" from self absorption can also be calculated by means of Equation 1 if an emission measure and electron temperature are assumed. Equation 1 was derived from Equation III-17 by the law of detailed balancing.

TABLE 22

INFRARED EXCESSES FROM IR/RADIO RATIOS

Position	Band (μ)	Ratio of Measured/Predicted	Absolute Amount of Excess ($W\ M^{-2}\ Hz^{-1}\ Ster^{-1}$)
50'' SOT	20	1850.	32,000. $\times 10^{-19}$
	11.6	1080.	16,000.
	4.8	3.80	27.1
	3.5	1.82	6.5
	2.2	1.38	3.4
	2.2	1.44	3.2
	1.65	1.57	4.4
	1.65	1.27	1.6
	1.25	1.71	8.9
Trapezium	20	6280.	120,000.
	11.6	2280.	37,000.

[continued on next page]

TABLE 22 (Continued)

Position	Band (μ)	Ratio of Measured/Predicted	Absolute Amount of Excess (W M^{-2} Hz^{-1} $Ster^{-1}$)
Trapezium	4.8	12.9	128. x 10^{-19}
	3.5	4.91	34.7
	2.2	2.27	12.5
	2.2	2.75	14.4
	1.65	2.86	15.9
	1.65	2.83	12.2
	1.25	3.16	30.5
	1.0μ (Hilgeman Reddening)	2.79	12.3
	1.0μ (Mendez Reddening)	4.84	26.5
	.82μ (Hilgeman Reddening)	2.88	10.9
	.82μ (Mendez Reddening)	4.72	21.6
50'' NOT	20	9390.	170,000.

[continued on next page]

TABLE 22 (Continued)

Position	Band (μ)	Ratio of Measured/Predicted	Absolute Amount of Excess (W M^{-2} Hz^{-1} Ster^{-1})
50'' NOT	11.6	1730.	26,000. × 10^{-19}
	4.8	29.3	289.
	3.5	11.1	84.4
	2.2	2.88	17.5
	2.2	1.92	7.1
	1.65	1.85	6.8
	1.65	1.24	1.5
	1.25	1.43	5.7

$$(1)\quad \tau_{ff}^{RADIO} = E_m \cdot 3.16\times10^{16} \cdot \frac{(17.65 - \ln\nu + \frac{3}{2}\ln T_e)}{\nu^2\ T_e^{3/2}}$$

For $\nu = 15.375$ gHz, $T_e = 8000^{\circ}$K, and an Em of 2×10^6 cm^{-6} pc a value for τ_{ff}^{RADIO} of 0.003 is obtained. Thus, the correction for self absorption is of no importance. An experimental verification can also be obtained by comparing the excesses in the 1.6 μ and 2.2 μ bands from Tables 20 and 22. The reasonable agreement is an indication that the extrapolation of the radio data should also be valid for the other bands considered.

Another possibility which can be considered is whether there is any significant dust emission at radio wavelengths. Such emission would have the effect of reducing the observed infrared excess as defined by the radio flux. That is, the real excess would be larger than observed, so that this mechanism cannot explain away the excess already seen, but could add to it. If dust temperatures of the order of one to two hundred degrees Kelvin are assumed, the black-body radio continuum predicted from the 10 and 20 micron data is several orders of magnitude smaller than observed. In addition, the shape of the radio spectrum is that predicted from free-free emission, not from black-body emission, so it is probably safe to assume that this possibility can be ignored.

The second question, concerning the different spatial resolution of the infrared and radio data is somewhat more difficult to answer. The regions north and south of the Trapezium lie on the slope of the contour map, so little correction is needed. The effect of a deconvolution would be to decrease the radio intensity assumed at these points and thus make the excess larger than the graphs now indicate. By a similar argument, a deconvolution of the radio data would make the excess for the Trapezium point smaller than the graph now indicates. These effects should be small, of the order of 10% in the infrared measured/predicted ratios since the radio and infrared spatial resolutions differ only by about 40%.

D. Properties of the Infrared Excess

The preceeding section has established the existence of infrared continuum radiation in excess of that predicted from known stars and recombination processes. Because the excess varies both with wavelength and with position, it is worthwhile to examine these properties more closely before attempting further analysis.

Figures 33 and 34 summarize the results of the preceeding section. Figure 33 shows the excess at various frequencies as a function of position and Figure 34 shows the excess for the three central regions as a function of wavelength.

As a first general observation, the complexity of these graphs would indicate that the excess is not explainable by a single simple process. One uniformity does stand out, however. This is the considerable similarity between the spectrum at 50" South and at the Trapezium. The ratio of the excess intensities is about 4 over a considerable range of wavelength. This may be compared with a ratio of about 1.5 for the Brackett line intensities for these same two regions. The similarity of the spectra indicate similar physical processes at the two positions, while the more rapid drop-off with distance than for the recombination radiation would indicate that the excess is more likely associated with the direct starlight than with a diffuse energy source such as the electrons or Lyman radiation field.

If these two hypotheses are true, what interpretation is to be

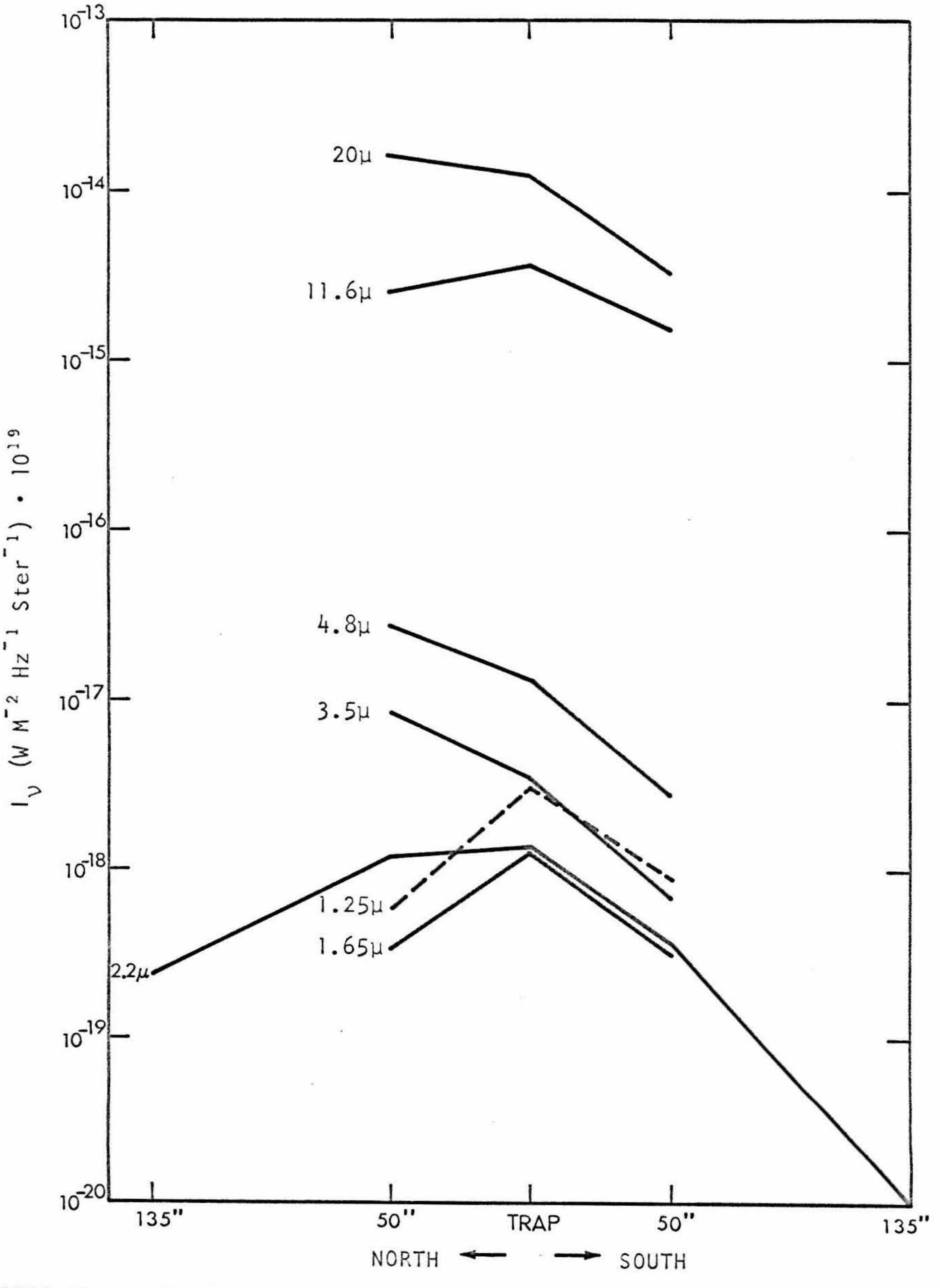

FIGURE 33 INFRARED EXCESS IN VARIOUS BANDS VS. DISTANCE FROM TRAPEZIUM (N.-S.)

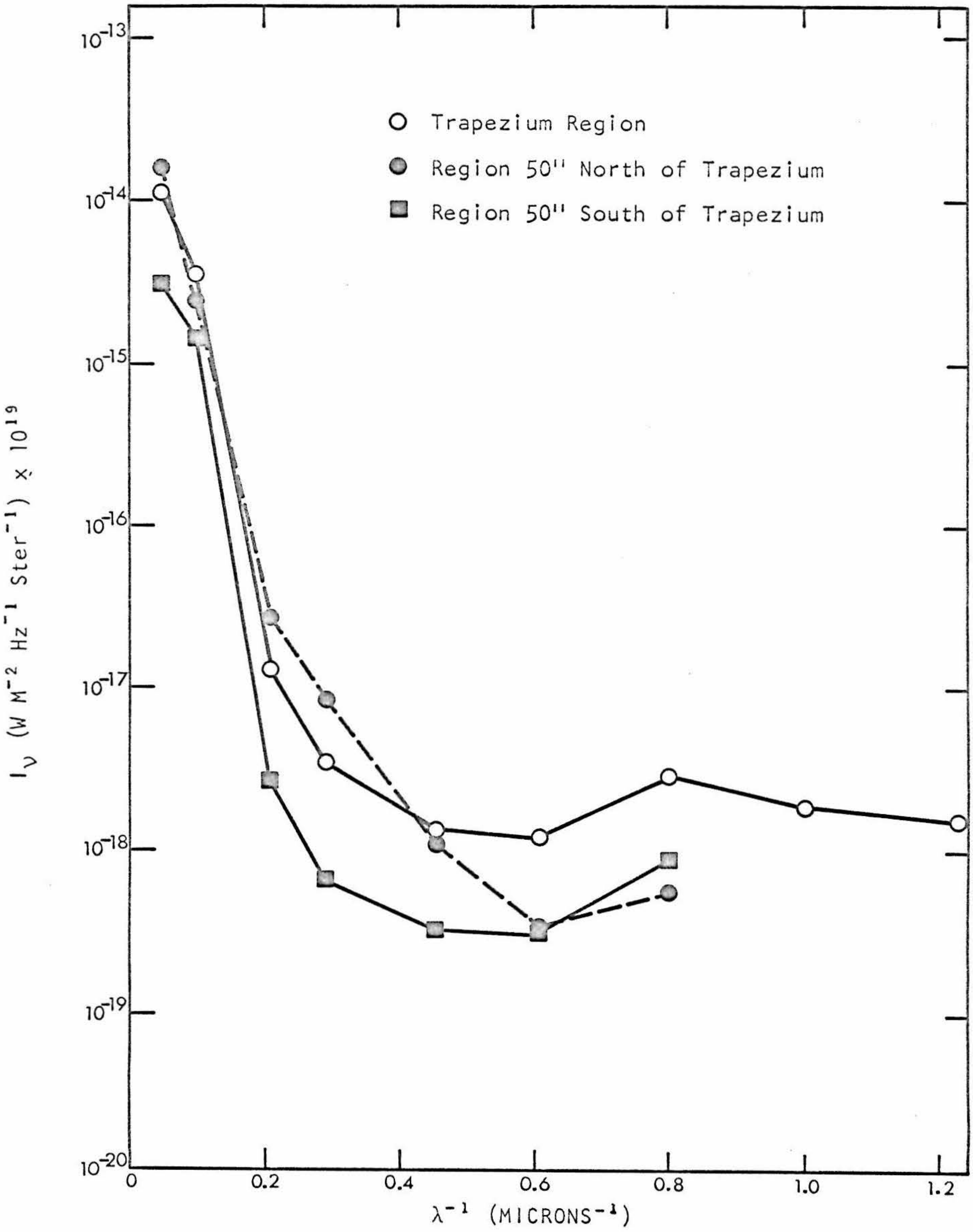

FIGURE 34   EXCESS OVER RECOMBINATION VS. λ^{-1}

made of the region 50" North? Either physical conditions are different or the physical processes are different, or both. If it is assumed that the same physical conditions are acting in the two similar regions to produce the excesses, it is also natural to assume symmetry around the Trapezium. With the exception of the 1.6 μ band, the region 50" North of the Trapezium has a larger excess in all bands than the region 50" South of the Trapezium. This is consistent with the interpretation of a symmetrical excess around the Trapezium to which is added an additional excess from the infrared nebula around ORS-1. If the excess from the southern region is subtracted from the excess in the northern region, an "excess in the excess" is obtained, as shown in Figure 35. Also shown in the figure are curves fit to the points for 150°K and 600°K black-bodies. 150°K is a believable temperature for the dust and 600°K may represent reflection or incomplete subtraction of the 600°K black-body spectrum of ORS-1. The flux represented on this figure at the 2.2 μ band is twice that of ORS-1, however. The errors in the ORS-1 flux are of the order of 10%, so incomplete subtration is an unlikely explanation.

If the technique of subtracting the two regions is valid, this is an interesting development. That is, the point-like 600°K source appears to be surrounded by a diffuse 600°K cloud, which has twice the flux of the point source.

Returning to the simple excess, either the preceding argument can be followed, or the nebula can be assumed non-symmetrical. If

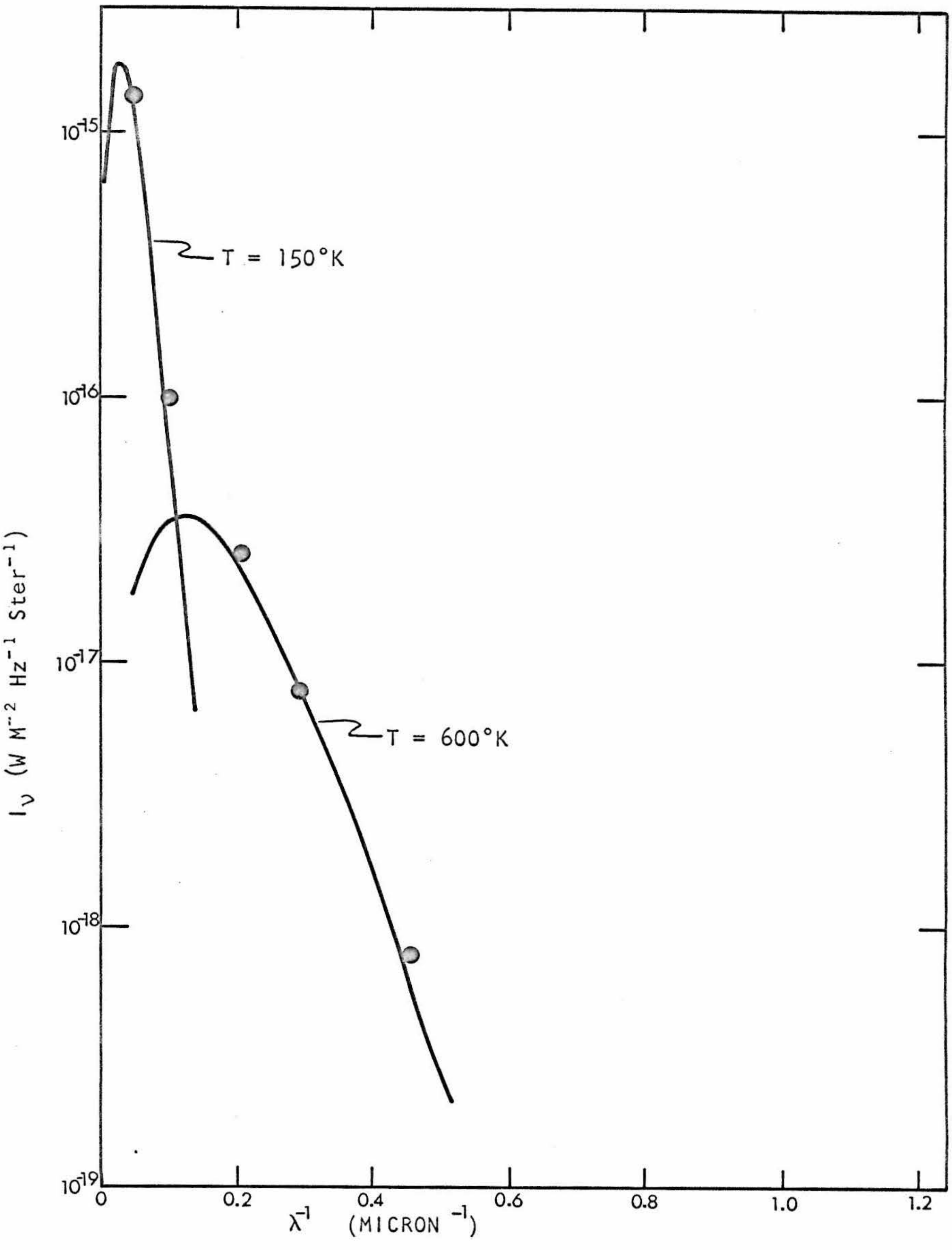

FIGURE 35 DIFFERENCE IN EXCESS BETWEEN NORTH AND SOUTH REGIONS IN M 42

the second course is followed, then different physical conditions must exist between north and south. This is an unattractive possibility since radio data and the infrared spectra of the preceeding chapter indicate a north-south symmetry in the fundamental physical parameters of electron temperature and density. For any further discussion, the symmetrical model with a perturbation from the ORS-1 nebula will be assumed.

E. H^- Emission and Absorption

The negative hydrogen ion (H^-) has a single bound state at 0.754 eV (1.64 microns). General considerations would then indicate that the sum of the free-bound and free-free radiation of this ion would show a dip in the spectrum at around 1.64 microns. Since this behavior does appear as a feature of the wavelength dependence of the observed infrared excess, a calculation of the expected amount of radiation is called for.

The derivation of the emission and absorption coefficients closely parallels that for neutral hydrogen, with the exception that the absorption cross section, $\varkappa(\nu, T_e)$ (cm^{-2} per H^- atom), must be evaluated numerically rather than included as simple analytic function. Fortunately, the calculation of values of $\varkappa(\nu, T_e)$ has already been accomplished with reasonable accuracy.

To calculate the emission coefficients, the absorption cross section is multiplied by the negative hydrogen ion density, the Planck function, and the correction for stimulated emission.

$$(2) \quad \epsilon_\nu^{H^-} = \varkappa(\nu,T_e) \cdot N_{H^-} \cdot \frac{2h\nu^3}{c^2} e^{-\frac{h\nu}{kT_e}} \quad \mathrm{ERG\ CM^{-3}\ SEC^{-1}\ STER^{-1}}$$

The Saha Equation may then be used to express N_{H^-} in terms of N_H (neutral hydrogen density) and N_e (electron density).

$$(3) \quad \epsilon_\nu^{H^-} = \varkappa(\nu,T_e) \cdot \frac{h^4}{2}\left(\frac{1}{2\pi m k}\right)^{3/2} \frac{\nu^3}{c^2 T_e^{3/2}} e^{-\frac{h}{kT_e}(\nu-\nu_0)} N_H N_e$$

where $h\nu_0 = 0.754$ eV.

The absorption coefficient is just the product of the absorption cross section and the negative hydrogen ion density. Once again using the Saha Equation, the absorption coefficient, α , becomes

$$(4)\quad \alpha = \varkappa(\nu, T_e) \cdot N_H N_e \frac{h^3}{(2\pi m k T_e)^{3/2}} \frac{e^{\frac{h\nu_0}{kT_e}}}{4} \; cm^{-1}$$

A table of $\varkappa(\nu, T_e)$ for free-bound transitions may be found in Geltman (ApJ 136, 935, 1962) for various values of ν . The free-bound absorption cross section is independent of electron temperature. A table of $\varkappa(\nu, Te)$ for free-free transitions may be found in Ohmura and Ohmura (Phys. Rev. 121, 513, 1961) for various values of ν and T_e.

For the present calculation, an electron temperature of 8400°K was assumed. In addition, a gross simplification is made in assuming homogeneity in N_H and N_e. This is done since only an upper limit to the H^- emission and self absorption is required.

With the assumption of homogeneity, the "in situ" ϵ and α may be used to calculate the observable $I_\nu \, d\nu$ and τ. Recent Lyman observations (Carruthers ApJL 156, 97, 1969) have determined the excess of neutral hydrogen atoms over the interstellar value in the direction of the Trapezium to be about 4×10^{20} hydrogen atoms/cm^2. Inserting this value for N_H and integrating, the unknown depth of the gas cancels, leaving

$$(5)\quad I_\nu^{H^-} = \varkappa(\nu, T_e) \cdot \frac{h^4}{2} \left(\frac{1}{2\pi m k}\right)^{3/2} \frac{\nu^3}{c^2 T_e^{3/2}} e^{-\frac{h(\nu-\nu_0)}{kT_e}} \cdot 4 \times 10^{20} N_e$$

$$(6) \qquad \tau = \kappa(\nu, T_e)\, \frac{h^3}{4} \left(\frac{1}{2\pi m k T_e}\right)^{3/2} e^{\frac{h\nu_0}{kT_e}} \cdot 4\times 10^{20} N_e$$

Evaluating τ at 18.2 microns and allowing a maximum electron density of 10^3 cm^{-3}, $\tau \approx 10^{-11}$. Thus, self absorption is of no consequence. If a maximum value of 10^3 cm^{-3} is again assumed for the electron density in evaluating $I_\nu^{H^-} d\nu$, Figure 36 is obtained. As can be seen, this maximum value which the H^- emission may take on is several orders of magnitude lower than the observed infrared excess. In further discussion, H^- emission and absorption will be ignored.

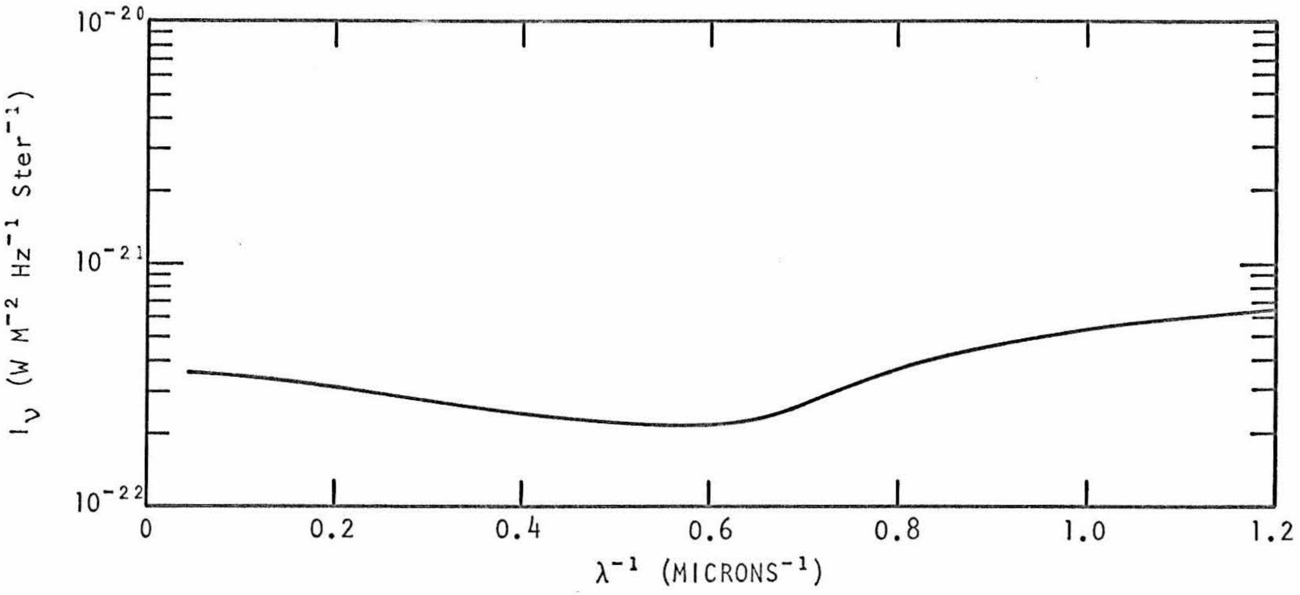

FIGURE 36 PREDICTED MAXIMUM H^- INTENSITY FOR THE ORION NEBULA

F. Heating and Cooling Mechanisms for Dust in M 42

As will be seen shortly, thermal emission from dust is unlikely to make any contribution to the excess for wavelengths shorter than two microns. In view of the aim of this chapter of determining whether various physical processes are acting, a division of the excess into longer or shorter wavelengths than 2 microns is thus convenient. Although the primary data indicating dust emission at long wavelengths do not come from the present work, effects of the emission are seen at wavelengths measured in this experiment. Some discussion of the dust emission is thus necessary.

Since an analytic solution for the dust absorption and emission properties does not exist for arbitrary values of shape of particle, size of particle, index of refraction, and incident wavelength, it will be necessary to make some assumptions in order to proceed.

The particles will be assumed to be smooth spheres. The emission will be essentially all at wavelengths much larger than the particle size. Thus, the emission is unlikely to be affected by the sphericity assumption. The absorption will be essentially all at wavelengths much smaller than the particle size. Here the smoothness of the surface can make a difference of as much as a factor of three.

Since the observed range of temperatures lies between $100^{\circ}K$ and $800^{\circ}K$, volatile materials such as ice, ammonia, etc. will not be considered. Two remaining possibilities are graphite and the metals, of which iron will be taken as representative.

Particles will be considered in a range of sizes from 0.01 microns to 100 microns. Smaller particles, while they may exist, require a quantum mechanical treatment which does not exist. Larger particles can be ruled out experimentally since they should show diffraction effects in visible light, and these are not observed. An attempt will be made to determine a representative particle size to see if the limits are consistent with the data.

First, the energy input from absorption of starlight will be computed. If a stellar temperature of 35,000°K (05V) is combined with the restraint on particle size, it is seen that 90% of the flux falls on particles for which the dimensionless quantity $x = 2\pi a/\lambda$ is greater than 0.2 and smaller than 10,000. Here "a" represents the radius of the particle. If this condition is met, then reference to absorption calculations (e.g. van de Hulst "Light Scattering by Small Particles," 1957) shows that, for the materials considered, the efficiency for absorption lies in the range 0.5 to 2.0. A great simplification arises if it is assumed that the absorption efficiency if identically 1.0, independent of wavelength. This makes it unnecessary to know the exact material properties in advance and introduces an error no greater than a factor of 2 in the energy balance equation. The primary advantage is that the expression for the particle heating rate (Equation 7) becomes separable in a and λ.

$$(7)\quad H_s = \int_0^\infty Q(a,\lambda)\, \pi a^2\, \pi B_\lambda(T_s) \left(\frac{R_s}{R_{sp}}\right)^2 d\lambda$$

$$(8)\quad H_s \approx \pi a^2 \, \frac{L_s}{4\pi} \left(\frac{1}{R_{sp}}\right)^2$$

H_s is the heating rate per particle, $Q(a, \lambda)$ is the absorption efficiency, $B_\lambda(T_s)$ is the specific flux from the star at temperature T_s, R_s is the radius of the star, R_{sp} is the distance from the center of the star to the particle, and L_s is the stellar luminosity. In order to calculate Equation 8, it was assumed $Q(a, \lambda) = 1$ and $B_\lambda(T_s)$ was the Planck function. Note that making the surface rough instead of smooth makes the absorption efficiency approximation even better.

The heating rate by collisions with electrons or protons is strongly dependent on the particle charge. Near the star, the photoelectric effect is expected to make the particle positive, while at great distances the higher thermal velocity of the electrons is expected to make the particle negative. It will be shown that for the inner regions considered in this chapter, the grain change is positive.

Following Mathews (ApJ 147, 965, 1967) one has, near the star,

$$(9)\quad \xi_p e^{\gamma} + K = \xi_e \left(\frac{M_H}{m_e}\right)^{1/2} (1 - \gamma) \quad \{\text{for } \gamma \le 0\}$$

where $\gamma = -\frac{eV}{kT_e}$, ξ_e (or ξ_p) represents the "sticking" probability for the electron (or proton) after a collision, K is the ratio of the photoelectrons ejected/sec. to the protons striking per second (evaluated for $\gamma = 0$), and M_H and m_e are the masses of the proton and electron respectively. K may be evaluated from

$$(10) \quad K = \frac{\Phi\, p\, L_s}{8\, \sigma\, T_s} \left(\frac{M_H}{2\pi k}\right)^{1/2} \frac{\Psi\left[\nu_t(\gamma)\right]}{N_p\, T_e^{1/2}\, R_{sp}^2}$$

where Φ is the mean value of photoelectric efficiency for photons beyond the threshold energy, pT_s^3 is the integrated photon flux from a black-body surface, L_s is the star's luminosity, k is Boltzmann's constant, N_p is the proton density, R_{sp} is the distance from the center of the star to the particle, and $\Psi[\nu_t(\gamma)]$ is the fraction of photons with energies greater than the threshold energy $h\nu_t(\gamma)$.

Near the star, the large positive charge on the particles makes the value of ξ_p unimportant and also makes the value of ξ_e approach 1. ξ_p will be taken as 1.

In order to determine the distance over which the grain is positive, $\gamma = 0$ is substituted into Equation 9, which gives for a proton density, N_p, of $10^3 \mathrm{cm}^{-3}$, an electron temperature T_e of 9000°K, a stellar temperature T_s of 35,000°K, a luminosity of 3×10^{39} erg/sec, $\Phi \approx 0.2$ electrons/photon, and $h\nu_t \approx 12$ ev a radius of 1.6 pc or 11' projected on the nebula. This is considerable larger than the region under discussion.

Since even for neutral particles the energy contributed from proton collisions is several orders of magnitude smaller than that from electron collisions, the proton collision contribution certainly can be ignored for these positively charged grains.

The heating rate from electron collisions may then be expressed as the average energy per electron times the collision rate

$$(11) \quad H_e = \tfrac{1}{2} m_e \langle v_e \rangle^2 \cdot Q_{coll}\, \pi a^2 \langle v_e \rangle\, N_e$$

(12) $$H_e = 4\sqrt{\frac{2}{\pi m_e}}\,(kT_e)^{3/2} \cdot Q_{coll}\,\pi a^2 N_e$$

where He is the heating rate from electron collisions, Ve is the electron celocity, < > denotes an average value, and Q_{coll} is the efficiency factor for collisions. It is easy to show

(13) $$Q_{coll} = 1 - \frac{2}{3}\vartheta = 1 + \frac{2}{3}\frac{eV}{kT_e}$$

from conservation of energy and angular momentum. ϑ can be calculated from an iterative solution of Equation 9.

The heating rate from the diffuse Lyman α (L_α) radiation field can be obtained from the product of the energy density in L_α, the velocity of light, and the particle cross section

(14) $$H_{L\alpha} = N_\alpha \cdot h\nu_\alpha \cdot c \cdot \pi a^2$$

Here N_α is the number density of L_α photons, and $h\nu_\alpha$ is the energy of a L_α photon. N_α may be calculated from the emission coefficient in L_α. Following O'Dell (ApJ 142, 1093, 1965) one obtains

(15) $$N_\alpha = \frac{(1-x)\,N_e\,N_p\,\alpha_B\,L\,n_s}{c}$$

where X is the percentage of transitions to level 2 which give two quantum radiation, N_e and N_p are electron and proton number densities, α_B is the recombination coefficient for levels 2 and higher, L is the mean free path of L_α, n_s is the average number of scatterings the radiation undergoes before it escapes or is destroyed, and c is the velocity of light. $L n_s$ may conveniently be expressed as

$$(16) \quad f R = L\, n_s$$

where R is the outer radius of the nebula and f, representing the ratio of the average distance traveled to the nebular radius, has been tabulated by O'Dell (loc. cit.).

Still another method of heating, which has not been considered before, is the diffuse Lyman continuum which is reflected back by the neutral outer regions of the nebula. While there is some question as to the radius of the outer neutral region, at least its existence has been demonstrated (Carruthers ApJL 156, 97, 1969 and Clark ApJ 142, 1398, 1965). From Clark, a radius (R) of 1 pc (6.9') will be assumed. This is also the radius of the Stromgren sphere for an O5 star with $N_e \approx 10^3$. For a star at 35,000°K, the luminosity below the Lyman limit (L_{LC}) is approximately 9 x 10^{38} erg/sec. If it is assumed that the Lyman quanta are destroyed or escape by conversion before a second reflection, then a minimum heating rate is given by

$$(17) \quad H_{LC} = L_{LC} \frac{a^2}{R^2}$$

The four heating rates considered are summarized in Equations 18-21, where appropriate numerical constants have been used at an assumed electron temperature of 9000°K and electron density of 1.5 x 10^3 cm^{-3}.

$$(18) \quad H_e = 6.9 \times 10^{-16} \left(1 - \tfrac{2}{3}\gamma\right) a^2(\mu) \qquad \text{WATT}/\text{PARTICLE}$$

$$(19) \quad H_s = 3.7 \times 10^{-12} \frac{a^2(\mu)}{R^2(')} \qquad \text{WATT}/\text{PARTICLE}$$

(20) $H_{L\alpha} = 6.6 \times 10^{-12}\, a^2(\mu)$ WATT/PARTICLE

(21) $H_{LC} = 9.5 \times 10^{-14}\, a^2(\mu)$ WATT/PARTICLE

Since the value of γ at 0'.3 from the Trapezium is only about -40, it is seen that the heating rate by electron collision is a minor contribution. This is important, and also somewhat puzzling. Far infrared spectroscopy of planetary nebula by Gillet et al. (ApJL <u>149</u>, 97, 1967) and Gillet and Stein (ApJL <u>155</u>, 97, 1969) show that the strengths of the infrared forbidden lines are one to two orders of magnitude fainter than theoretically predicted. The continuum is, however, two to three orders of magnitude higher than that expected from pure recombination, much like the Orion Nebula. If the above equations are correct, and the dust is only weakly coupled to the electron gas, one is left without an adequate mechanism for cooling the gas.

Ignoring the small contribution from the reflected Lyman continuum radiation, the heating is seen to be predominantly by starlight out to a radius of about .8', then by the diffuse L_α field. This is consistent with the observation that the observed infrared excess decreased more rapidly than the B_γ intensity (Section D).

Using Equations 19 and 20, and deriving an expression for the dust emission rate, it is possible to calculate the size of the particles radiating at various temperatures. Assuming radiative cooling only, the cooling rate is given by

$$(22)\quad C_R = \int_0^\infty Q(a,\lambda)\, 4\pi a^2\, B_\lambda(T_D)\, d\lambda$$

where Q(a,λ) is the efficiency factor as a function of particle radius "a" and wavelength "λ", and B_λ (T_d) is the Planck function evaluated at a dust temperature, T_d.

At this point, a considerable simplification arises if the particle radius is assumed smaller than the maximum wavelength considered (2 microns). This is a more restrictive assumption than was used for deriving the absorption. The validity of the assumption may be checked from the results of the size calculation to follow. If the particle size is small compared to the wavelengths of emission, the absorption efficiency simplifies to (see e.g. van de Hulst "Light Scattering by Small Particles" p. 70, 1957)

$$(23)\quad Q(a,\lambda) = -\frac{8\pi a}{\lambda}\, \mathrm{Im}\left\{\frac{m^2-1}{m^2+2}\right\}$$

$$(24)\quad Q(a,\lambda) = \frac{a}{\lambda}\, \frac{48\pi\, \eta\varkappa}{(\eta^2-\varkappa^2+2)^2+4\eta^2\varkappa^2}$$

where m is the complex index of refraction, $m = \eta - i\varkappa$. Substituting for the Planck function, the cooling rate then becomes

$$(25)\quad C_R = 384\,k \left(\frac{\pi a}{c}\right)^3 \left(\frac{kT_d}{h}\right)^5 \int_0^\infty \frac{\eta\varkappa}{(\eta^2-\varkappa^2+2)^2+4\eta^2\varkappa^2}\, \frac{x^4}{e^x-1}\, dx$$

In general, η and $\varkappa$ are complicated functions of λ, so the standard practice (see e.g. Swamy & O'Dell ApJ <u>147</u>, 529, 1967) is to remove them from the integral, evaluating them at some wavelength characteristic of the blackbody temperature. Since both η and $\varkappa$ vary rapidly with λ for graphite or the metals, this is not a very good approximation, nor is it necessary. In the wavelength intervals under consideration, both graphite and the metals obey the Law of Hagen-Rubens, which may be summarized by $\eta\varkappa \gg 1$, $\eta \approx \varkappa$, and $\varkappa^2 = \frac{\sigma}{2\nu}$, where σ is the conductivity in Gaussian units (sec^{-1}). Thus, the cooling rate may be evaluated analytically to a good approximation.

$$(26)\quad C_R = \frac{384\,h}{2\sigma}\left(\frac{\pi a}{c}\right)^3\left(\frac{k T_d}{h}\right)^6 \int_0^\infty \frac{x^5}{e^x - 1}\,dx$$

The value of the integral is 122. For graphite, a conductivity of 1.2×10^{15} sec^{-1} will be adopted from Taft and Philipp (Phys. Rev. 138, A197, 1965) and for iron, a conductivity of 2.2×10^{17} sec^{-1} will be adopted from the Handbook of Chemistry and Physics (44, 2667, 1962). Equation 26 shows an important property of the cooling rate for the present discussion, in that it is proportional to a^3. As will be recalled, the heating rates were derived as all being proportional to a^2. Thus, in postulating thermal balance, a relation is obtained between the particle size and particle temperature. For this discussion, the dust temperature will be regarded as an observed quantity, and the particle size derived.

While a spread of particle sizes, and thus of temperature, is the most likely situation, it is not possible to convert the observed flux into temperatures in a unique way. Since the temperature distribution cannot be uniquely determined, neither can the particle size distribution.

A different question can be asked. What is the minimum number of single temperature blackbody curves which, when superimposed, will represent the excess? As has already been mentioned, the region 50" north of the Trapezium appears more complicated and will be discussed in Section I. The long wavelength excess in the other two regions is reasonably well fit by two blackbody curves at temperatures of 200°K and 800°K. Table 23 gives the particle radii derived from equating the heating and cooling rates for the two regions and assuming either iron or graphite particles.

The higher temperature results offer little to prefer between graphite and iron, although the graphite particles are so small that the analysis is probably no longer valid. Note that the particle sizes at higher temperatures would vary as T^{-6}, so it is unlikely that there is any significant dust emission at wavelengths shorter than 2 microns. The lower temperature results show that the particle size is larger than assumed. The very large numbers are not believable since the derivation is no longer valid, and about all that can be said is that the particles are larger than a one micron radius. It should be mentioned that a particle size larger than the supposed interstellar average (0.2-0.5 microns) would be consistent with the abnormal reddening curve in Figure 13. Although the size of particle is difficult to evaluate from the curve, it is not likely that the average size would be much larger than 2 microns.

For large particles, a different expression for the cooling rate is necessary.

$$(27) \quad C_R = 4\pi a^2 \frac{\epsilon}{2} \sigma T_0^{\,4}$$

where ϵ is the bulk emissivity at perpendicular incidence (the factor of two accounts approximately for the non-Lambertian character of the

TABLE 23

DERIVED PARTICLE SIZES

Region	Dust Temperature	Dust Material	Particle Size (μ)
Trapezium	200°K	Graphite	63
		Iron	11,500
	800°K	Graphite	.016
		Iron	2.9
50" SOT	200°K	Graphite	16
		Iron	3,000
	800°K	Graphite	.004
		Iron	.72

TABLE 24

DERIVED EQUILIBRIUM TEMPERATURES

Region	Dust Material	Equilibrium Temperature Large Particles
Trapezium	Graphite	130°K
	Iron	210°K
50" SOT	Graphite	90°K
	Iron	160°K

material), and σ now is the Stefan-Boltzmann constant.

If Equation 27 is used in place of Equation 26, the ratio of the heating and cooling rates is no longer dependent upon particle size. An interesting calculation can be made, however. The equating of the heating and cooling rates for large particles determines the temperature uniquely. This has been done for Table 24. The agreement of the predicted and observed value of the temperature is a check on the validity of the calculations. Table 24 shows a closer agreement for iron than for graphite to the measured color temperature of 200°K.

Wickramasinghe ("Interstellar Grains" p. 109, 1967) has pointed out that the observed interstellar absorption of about 1 mag/kpc would imply an abundance of about .01 by mass if it were caused by iron particles. Since the solar iron abundance is about .0002 by mass (Wickramasinghe, p. 55, loc. cit.), it would appear that iron is an unlikely possibility for interstellar material. As will be shown later, a similar argument can be applied to the Orion Nebula.

G. Gas to Dust Ratio in M 42

The relative amount of gas and dust in interstellar clouds is an important parameter in the early stages of star formation (Spitzer in Stars and Stellar Systems, Vol. VII). Attempts to determine this ratio in the visual have necessarily depended upon an analysis of the scattered and absorbed light. These processes are difficult to evaluate and strongly dependent upon the sizes, shapes, configuration, and composition of the dust particles, which are poorly known. The ratio can be determined much more accurately by an analysis of the far infrared emission from the particles. Unfortunately, limitations in the transparency of the atmosphere permit observations only out to about 25 microns. Thus, only those particles hotter than about 100°K can be accurately observed. For this reason, the infrared method must, for the present, be limited to regions near hot stars where neither the masses, sizes, or configurations of the particles are likely to be similar to those which comprise the bulk of interstellar matter. In the following, only properties of the dust in the inner regions of M 42 will be discussed.

As was seen in the preceding section, the heating by starlight and L_α should be sufficient to produce temperatures of 150°K to 200°K within the ionized region for large particles. Small particles will necessarily have larger temperatures. Outside the ionized region, the energy available for heating decreases rapidly with distance and the bulk of these particles are probably at temperatures an order of magnitude lower (Spitzer "Diffuse Matter in Space" p. 145, 1968). Thus, two extremely useful features of the configuration are that emission from all the particles is seen and the emitting region is sharply defined. The presence of dielectric mantles upon the grains would challenge the first feature, but Wickramasinghe (Interstellar Grains, ed. by Greenberg and Roark, p. 182, 1967) has calculated that the time to sputter away such mantles is considerably less than the probable age of the nebula.

The optical depth, τ, may be related to the particle number density by

$$N_D(a) \cdot \ell \cdot \pi a^2 = \tau(a) \tag{28}$$

where $N_D(a)$ is the number of particles of radius a per cm^3, and L is the depth in line of sight.

Thus, the usual expression calculated for the gas to dust ratio becomes

$$\frac{N_H}{N_D\ C_D} = \frac{L}{\tau} \cdot N_e \cdot \frac{N_H}{N_e} \tag{29}$$

where C_D is an effective average cross section.

At this point, it is useful to evaluate τ. The two methods of evaluation used in Section III-D will be applied here. If the two temperature approximation to the long wavelength excess which was used in the preceding section is retained, Table 25 results. τ from the percent of total flux cannot be accurately determined for 800°K, where τ is small.

TABLE 25

OPTICAL DEPTH FROM INFRARED EMISSION

Region	T_{DUST}	τ (Color-Brightness)	τ (% of Total Flux)
Trapezium	200°K	.085	.10
	800°K	6.5×10^{-7}	-
50'' SOT	200°K	.028	.025
	800°K	1.2×10^{-7}	-

If all the dust is really being observed, these optical depths appear discordant with the observed extinction as given in Section III-C. One explanation is that the extinction really is small within the ionized inner region and that the observed extinction is dominated by similar particles, only with ice mantles, positioned outside the ionized region. This would also agree with the remarkable similarity in the wavelength dependence of the infrared excess between the Trapezium region and the region south of the Trapezium. Another prediction of this model is that the gas/dust ratio calculated from extinction at a wavelength near H β should be about 14 times smaller than that calculated from the infrared emission for the Trapezium region and 48 times smaller for the region 50" South of Trapezium. As will be seen shortly, the difference turns out to be factors of four and twelve, respectively. This is probably in reasonable agreement with the prediction, considering the simplifications of the model.

With the observed values of τ, and assuming a depth in line of sight of 3.6×10^{18} cm, Equation 29 was used to calculate Table 26, giving the gas to dust ratio at the various positions and effective temperatures. These numbers are to be compared with the value of 144×10^{20} cm^{-2} obtained by O'Dell ("Interstellar Grains" Greenberg & Roark, eds., p. 137, 1967) for the inner regions of M 42 from the line to continuum ratio at H_β. As was suggested earlier, the differences with the 200°K data may be directly explained in terms of the differences in τ for emission and absorption, which suggest

TABLE 26

GAS/DUST RATIO BY NUMBER

Region	Dust Temperature	N_H/N_DC_D (Cm^{-2})
Trapezium	200°K	520×10^{20}
	800°K	$7.2 \times 10^{7} \times 10^{20}$
50'' SOT	200°K	1700×10^{20}
	800°K	$3.9 \times 10^{8} \times 10^{20}$

either that different regions are absorbing than are emitting or that not all the dust is seen in emission. The latter possibility was excluded by thermal balance arguments. The differences with the 800°K data exist because only a small amount of the total dust is emitting at that relatively high temperature.

If a characteristic radius and bulk density of the dust are now assumed, the numbers in Table 26 can be turned into mass density ratios. The particle number density may be related to the bulk material density, ρ, by

$$M_D(a) = N(a)\,\rho\,\frac{4}{3}\pi a^3 \tag{30}$$

where $M_D(a)$ is the mass of dust per cm^3 of space. $M_D(a)$ may thus be expressed by

$$M_D(a) = \frac{4}{3}\frac{\tau \rho a}{\ell} \tag{31}$$

The mass of hydrogen per cm^3, M_G, may be expressed by

$$M_G = \frac{N_p}{N_e} * N_e * m_p \tag{32}$$

where N_p is the proton density and m_p is the mass of the proton. Taking the ratio of Equations 31 and 32, and combining with Equation 29

$$\frac{M_G}{M_D} = \frac{3}{4}\frac{\ell N_p m_p}{\rho a \tau} = \frac{3}{4}\frac{m_p}{\rho \bar{a}}\left(\frac{N_H}{N_0 C_0}\right) \tag{33}$$

With the assumption of $\rho = 2.2$ gm cm^{-3} for graphite and $\rho = 7.8$ gm cm^{-3} for iron (CRC Tables), all quantities in Equation 33 are known. Lest the last statement appear too enthusiastic, it will be admitted that they are not all known well. However, the gas to dust ratio should be good to an order of magnitude, and this is sufficient.

Evaluating Equation 33, Table 27 results. Since the Solar H/C ratio is 160 by mass, and the H/F_e ratio is 4800 by mass (Wickramasinghe "Interstellar Grains" p. 55, 1967), Table 27 permits the elimination of iron as the source of the emission. Near the Trapezium, a high proportion of the carbon is tied up in the dust. Very few of the grains are small (high temperature), and the grain density appears to decrease faster than the hydrogen density with distance from the Trapezium.

If a value of M_G/M_D of 500 is adopted for the highly ionized region (4' radius) and a value of $N_H \approx 10^3$ cm^{-3}, a total of 20 $M_\odot$ is obtained for the gas and 0.04 $M_\odot$ for the dust. Clearly, grain growth and condensation processes could have disturbed this small amount of dust from its initial interstellar equilibrium properties. It would thus be unwise to attempt any extrapolation of the M 42 dust properties to the general interstellar medium.

TABLE 27

GAS/DUST RATIO BY MASS

Region	T_{DUST}	$\bar{a}$ (μ)	Material	M_G/M_D (By Mass)
Trapezium	200°K	2.0	Graphite	200
		2.0	Iron	50
	800°K	.02	Graphite	2×10^9
		2.0	Iron	7×10^6
50'' SOT	200°K	2.0	Graphite	600
		2.0	Iron	200
	800°K	.004	Graphite	7×10^{10}
		1.0	Iron	8×10^7

H. The Shorter Wavelength Infrared Excess

After subtracting the well defined recombination radiation and dust emission at the longer wavelengths, a portion of the continuum remains unaccounted for. Hot dust is not possible since the implied temperatures would vaporize any known material. H^- emission has been shown to be too weak. The remaining possibility is some form of scattering, either by dust or by electrons. In order to examine this possibility, a review of the properties of the remaining excess is in order.

The essential properties of the excess are that it decreases in intensity with increasing distance from the Trapezium, and that it increases with frequency at least out to a wavelength of 1.25 microns - at higher frequencies the spectrum of the excess may be flat or may decrease. The scattering process is capable of explaining these properties.

First, some qualitative points need to be made. Dust is known to scatter light in the visible; it is a likely candidate in the infrared also since large particles are indicated by the extinction curve. High resolution photographs of M 42 in H_α show a considerably different appearance from photographs in the light of the nearby continuum (Munch, private communication). Some process other than recombination radiation, and not proportional to N_e^2 must produce the continuum. Unfortunately, both dust and electron scattering satisfy these criteria (electron scattering only if there are large density fluctuations). The chief difference between electron scattering and dust scattering is that electron scattering is wavelength independent. If the scattered light is bluer or redder than the object, dust would be more likely than electrons. The cloud around the ORS-1 Nebula shows a reflection spectrum of 600°, identical to that of the point source. It is hard to conceive how dust could produce such a uniform scattering out to the M band (4.8 microns).

These remarks show that some numerical calculation is necessary to estimate the relative contribution of the dust and of the electrons. For unpolarized radiation, the Thompson scattering cross section per electron is given by (see e.g. Jackson "Classical Electrodynamics," p. 489, 1962)

$$(34) \qquad d\sigma = \pi \left(\frac{e^2}{mc^2}\right)^2 \frac{1+\cos^2\theta}{2\pi} \, d\Omega$$

where θ is the angle between the observer-electron and star-electron lines, and $d\Omega$ is the solid angle subtended by the observer.

Integrating over solid angle, the total scattering cross section, σ_T, is given by

$$(35) \qquad \sigma_T = \frac{8}{3} \pi \left(\frac{e^2}{mc^2}\right)^2$$

Combining Equations 34 and 35,

$$(36) \qquad d\sigma = \sigma_T \, \frac{3}{4} \left(1+\cos^2\theta\right) \frac{d\Omega}{4\pi}$$

The Trapezium flux, F_e, measured at the electron, times $\frac{d\sigma}{d\Omega}$, times the electron density is the volume emissivity per steradian, ϵ,

$$\epsilon = N_e \; F_e \; \frac{d\sigma}{d\Omega} \tag{37}$$

Multiplying by the depth in line of sight, L,

$$I_\nu = \overline{\frac{d\sigma}{d\Omega} \; N_e \; F_e} \;\; L \qquad \mathrm{w\,m^{-2}\,ster^{-1}\,Hz^{-1}} \tag{38}$$

where the $\overline{}$ denotes an average along the line of sight. $\overline{F_e}$ may be expressed in terms of the unreddened Trapezium flux, F_E, measured at the Earth by

$$\overline{F_e} = \left(\frac{R_{ET}}{\overline{R_{eT}}}\right)^2 F_E \tag{39}$$

where R_{ET} is the Earth-Trapezium distance (500 pc), and $\overline{R_{eT}}$ is a representative distance between the Trapezium and the electrons. Since F_E is corrected for reddening, Equation 39 gives a minimum value of the flux measured at the electrons.

Combining Equations 35-39, the quantity to be compared with observations is I_ν

$$I_\nu = \frac{8\pi}{3}\left(\frac{e^2}{mc^2}\right)^2 * \frac{3}{4}\,\overline{(1+\cos^2\theta)} \;\; \frac{F_E}{4\pi}\left(\frac{R_{ET}}{\overline{R_{eT}}}\right)^2 \overline{N_e} \; L \tag{40}$$

If Equation 40 is evaluated for the region 50" south of the Trapezium at a wavelength of 1.65 microns, the predicted intensity is 1.0×10^{-21} $\mathrm{wm^{-2}\ Hz^{-1}\ ster^{-1}}$. This is several orders of magnitude less than the observed excess, indicating that electron scattering is an unlikely cause of the excess.

The above conclusion is in direct contradiction to that of Mendez (Bol. de Los Obs. Ton. y Tac. 4, No. 27, 41, 1965). This is one reason the present derivation has been written out explicitly. An argument against Mendez' result which does not depend on a numerical calculation can be made. If electron scattering were the major contribution to the excess between 0.6 microns and 1.0 microns, then the excess should follow the Trapezium flux and decrease by a factor of ten over that interval (the factor is five if the reddened Trapezium is considered). That it does not is a strong argument against electron scattering.

A turnover at about 1 micron in the spectrum of the excess can be surmised from a comparison of Mendez' data (loc. cit.) and the results of Section D. This can be attributed to the dust being a stronger absorber at the shorter wavelengths. An accurate analysis of the spectrum of the observed excess would require first being able to estimate the spectrum of the Trapezium as if observed from various positions within the nebula. The preceding section has, however, indicated that the dust may not be uniformly distributed throughout the gas. All that will be concluded with the present data is that the position of the turnover in the spectrum of the excess would indicate a particle size on the order of 1 micron, in agreement with previous conclusions (Section F).

I. The ORS-1 Nebula

It has been some time now since the discovery of the very red star northwest of the Trapezium (here called ORS-1 for Orion Red Star no. 1 to avoid confusion with the second red star nearby, ORS-2, reported in Section II-G for the first time) by Becklin and Neugebauer (ApJ 147, 799, 1967) and the subsequent report by Kleinman and Low (ApJL 149, 1, 1967) that the object was surrounded by a bright nebula at 20 microns. Since that time, ORS-1 has been found to be a strong source of OH radio emission (Raimond and Eliasson, ApJL 150, 171, 1967) and a contour map has been produced of the ORS-1 nebula at 11.6 microns and 20 microns by Ney and Allen (ApJL 155, 193, 1969). The available data are consistent with the interpretation of the object as a collapsing protostar. It is worthwhile to examine the present data to see if any contribution to the knowledge of the properties of the object can be made.

The infrared spectra primarily indicate the properties of the hydrogen. As has been seen, there is little difference between the north and south regions of the nebula as far as the gas is concerned.

The spectra can also be used as a sensitive indicator of a continuum excess, however. The region to the north shows a greater excess than that in the south. This is also indicated by the photometry. The interpretation has been made in Section D that the northern excess can be understood as being the same as the southern excess only with the addition of radiation from the ORS-1 nebula. This being done, a spectrum showing the excess characteristic of the ORS-1 nebula was shown in Figure 35. The 600°K portion of the curve may be interpreted as scattered light from ORS-1. Since electron scattering has been eliminated as a possibility in the preceding section, this result is quite surprising. If the scattering is by dust, the particles must be of the order of five microns or more in diameter. This is gargantuan by normal interstellar standards.

The separation into two temperatures (150°K and 200°K) is probably not valid. The dust is probably really hotter in the north, near the ORS-1 nebula. This can be seen from the maps of Ney and Allen (loc. cit.) which have good spatial resolution. Near the maximum of the ORS-1 emission, the Trapezium nebula contribution can be shown small. Thus, the observed color temperature of 220° (Ney and Allen, loc. cit.) is characteristic of the ORS-1 nebula. It should be mentioned that contour maps at the 3.5 μ and 4.8 μ bands would be useful in deciding if the 600°K reflection spectrum is real. As can be seen from the argument of the preceding section, maps in the 2.2 μ band are confused by reflection of the Trapezium light and would not be as suitable.

In summary, the present data suggest that ORS-1 is surrounded not only by hot dust, but also by a reflection nebula of unusually large dust particles.

APPENDIX 1

Considerations of Optimum Resolution and Scanning Techniques

The primary objectives of this discussion are to consider the controllable factors affecting the power received at the spectrometer detector from an astonomical source of line and continuum emission. For simplicity, point sources will be perfect points, mirrors will be perfect reflectors, and the projected size of the entrance and exit slits of the spectrometer will be equal. Extension to more complicated situations is not difficult and does not affect the basic conclusions.

When considering a point source, the observable quantity at the Earth's surface is flux, which may be expressed in units of watts/m^2/μ for the continuum and watts/m^2 for a line. When considering an extended object the observable quantity at the Earth's surface is intensity, which may be expressed in units of watts/m^2/μ/steradian for the continuum and watts/m^2/steradian for a line.

The detector system is assumed capable of receiving all the power which passes through the exit slit. With a reasonable choice of size of slit, this is not a serious constraint. Detector noise is considered to be the limiting noise in the system; that is, an optimizing of S/N is achieved by maximizing the power passing through the exit slit. If sky noise should be more important than detector noise, maximizing the power through the exit slit does not necessarily improve the S/N. In low S/N applications it is important to know the dominant source of noise as well as its power spectrum (see

Appendix 2).

For observation of a point source a large telescope is desirable since the power through the exit slit will be proportional to the primary mirror area. The f ratio (focal length/mirror area) of the spectrometer is not important and it can be chosen to satisfy design constraints internal to the spectrometer, such as size of grating and desired resolution. It can be argued that it must be the same as the telescope f ratio, but since most large telescopes have a choice of several f ratios, this is not a serious difficulty.

For observations of extended objects a small f ratio is desirable since the power through the exit slit will be proportional to primary mirror area times solid angle covered (solid angle is proportional to (focal length)$^{-2}$ for a fixed slit); that is, the power through the exit slit will vary as (f ratio)$^{-2}$ for a fixed slit. Changing telescope size without changing the f ratio or the slit size will affect only the spatial resolution. Of course, if the extended object is not of uniform intensity, a change in spatial resolution can be important, so that as a practical matter the telescope size is a consideration. Another minor consideration is that in double beam work, it is usually desirable to have one of the beams off the object and spatial resolution can again be a practical factor.

At this point it should be mentioned that it is possible to design different combinations of telescope, spectrometer, and detector which will do an identical job on extended objects. There is no one to one relationship between job to be done and ideal spectrometer (if we ignore individual preferences and financial factors). The primary aim here is to examine factors affecting the performance of a spectrometer once the arbitrary decisions have been made. Assuming then that a grating and an f ratio have been selected, the linear dispersion is fixed (if the full grating is used) and we can examine the consequences of varying slit size, which is the only parameter left to discuss.

For a point source, we see that as long as the resolution ($\Delta\lambda$) is wider than the line, the line power through the exit slit (and thus the line S/N) is independent of $\Delta\lambda$. Similarly, the continuum S/N must be proportional to $\Delta\lambda$. If little information is known about the variation of the continuum or the number of nearby lines, it would appear that the optimum resolution is of the order of the line width. If wider, the continuum measurement will necessarily be at a point further from the line and may include other unresolved lines. If narrower, it will take more than one measurement to obtain the whole line intensity. Sometimes, however, the shape of the line is important and it is worth the sacrifice in S/N to obtain this extra information. Or perhaps there are many nearby lines and $\Delta\lambda$ has to be decreased to make a continuum measurement. Little is gained by increasing $\Delta\lambda$ beyond the line width except a better S/N on the continuum.

The situation with an extended source is significantly different. For the continuum, the power passing through the exit slit is proportional to $\Delta\lambda$ times the area of the entrance slit. For a line, it is proportional to the area of the entrance slit. Thus, remembering the entrance and exit slits are of equal projected area, the observing time needed for a line is proportional to $(\Delta\lambda)^{-2} \cdot (\text{slit length})^{-2}$. At first it might be assumed that this would imply opening the slits as wide as possible and making them as long as possible, but this is not necessarily best. If a reasonable S/N can be obtained with the slits closed down, the previously mentioned considerations of varying continuum and nearby line may be of more importance. Another consideration which affects the choice of $\Delta\lambda$ and slit length is that some types of variations of line intensity across a large aperture are not well represented by a simple average. The optimum resolution must be recalculated for each new situation. When measuring a previously unmeasured object, $\Delta\lambda$ should be such that the line intensity can just be measured. This is, of course, impossible to calculate on an unmeasured object, but it does suggest that a trial measurement at large $\Delta\lambda$ can save a great deal of wasted effort in later measurements.

The arguments presented on optimum resolution have made a simplification which does not usually hold in practice. That is, the assumption of perfect step scanning. In practice, the slit does not simply alternate between totally on the line and totally off, but instead scans onto and off the line; only part of the total power discussed will be getting through the exit slit during such times. If a square response is assumed, the average S/N is reduced by a factor of two by using continuous scanning. What is so good about continuous scanning that makes it worth giving up a factor of four in integration time? First, continuous scanning frees one from having to know the exact wavelength of the line in advance. This is usually not a serious problem. Second, continuous scanning will indicate the presence of nearby lines and varying continuum. This is a critical piece of information when observing an object for the first time, but becomes useless once a negative result is obtained. Thus, it is highly recommended that any future observations of M 42 be done by step scanning. NGC 7027 showed a satellite line near B_7 and should not be looked at by step scanning techniques.

Another technique similar to step scanning is chopping in wavelength instead of in position. If the wavelength is not scanned while chopping, the effect is similar to step scanning except (1) no value is obtained for the continuum flux (2) absolute calibrations are thus more difficult and (3) no reference dewar can be used as a monitor. These disadvantages are accompanied by the advantages (1) of not having to keep a reference beam off an extended object (2) of being able to handle signals which may be varying in intensity during the observation (e.g., if the dominant noise is sky noise) (3) of a gain in S/N of a factor of two over step scanning. The third point is merely a consequence of not measuring the continuum. If a continuum measurement is needed, it has to be made some other way with the built in difficulties of trying to measure the same position and area. Measuring the continuum by some other means would also allow the step scanning method to gain a factor of two in S/N merely by not measuring the continuum but using the externally generated value to subtract from the line plus continuum measurement total of both beams. It should be pointed out that the wavelength chopping method will also lose a factor of two in S/N if the wavelength is scanned while chopping.

In summary then, the wavelength is continuously scanned if there are doubts about the surrounding continuum. Spatial chopping is used if the continuum is needed at the same position. Wavelength chopping is used if (1) the signal is varying rapidly or (2) the continuum is not needed and a maximum S/N is desired on the line.

APPENDIX 2

Optimizing Signal to Noise Ratios in Scanning Spectrometers by Convolution Techniques

It has been shown in Appendix 1 that when scanning point sources with resolution of the order of the line width or extended objects with equal entrance and exit slits, losses in S/N can become as large as a factor of two. However, by making use of some of the properties of the scanning, a portion of the loss can be recovered. The scan may be thought of not only as a scan in wavelength, but also as a signal which varies in time. It is this second property which is used in the analysis to follow. If the source itself does not vary, then variations in output can only be caused by spectral intensity differences in the source or spectral sensitivity differences in the atmosphere-telescope-spectrometer-detector combination. The spectrometer acts like a filter in that only certain variations with time are permitted. Noise which does not satisfy the same restrictions may be separated from the signal and eliminated.

The case of an extended source of line emission will be considered. Other cases may be developed along similar arguments. The line may be thought of as a delta function input at time $t = \tau$, $\delta(t-\tau)$. The response of the spectrometer to this input is some characteristic function $\lambda(t, \tau)$. A common case is where the function is separable into a "spectrometer wavelength response" and a "slit response."

(1) $$h(t,\tau) = w(t) \cdot s(t-\tau)$$

The spectrometer wavelength response can always be divided out of a scan, so for the remaining analysis w(t) = 1. This has the effect of making the response time invariant. A well known property of linear systems which will be used here is that a knowledge of the system response to a delta function input permits the calculation of the system response to an arbitrary input. An arbitrary input spectral distribution may be represented on the time axis by a function f(t). Express f(t) as a sum of impulses

(2) $$f(t) = \int_{-\infty}^{\infty} f(\tau)\, \delta(t-\tau)\, d\tau$$

Introduce the linear operator $L\{\ \}$ such that

(3) $$L\{\delta(t-\tau)\} = s(t-\tau)$$

then the output function g(t) may be represented by

(4) $$g(t) = L\{f(t)\} = \int_{-\infty}^{\infty} f(\tau)\, L\{\delta(t-\tau)\}\, d\tau$$

(5) $$g(t) = \int_{-\infty}^{\infty} f(\tau)\, s(t-\tau)\, d\tau$$

or

(6) $$g(t) = \int_{-\infty}^{\infty} f(t-\tau)\, s(\tau)\, d\tau$$

Now consider the Fourier transform S(ω) of the impulse response s(t).

(7) $$S(\omega) = \int_{-\infty}^{\infty} s(t)\, e^{-i\omega t}\, dt$$

"ω" should not be confused with the frequency of the light passing through the slit nor with the chopping frequency; it represents a frequency of modulation of the signal. If the Fourier transforms of the input and output functions are represented by F(ω) and G(ω), we can use Equation 6 and the convolution theorem to obtain

(8) $$G(\omega) = F(\omega) \cdot S(\omega)$$

With a noise free output signal, this relationship can be inverted to obtain the original input signal. The aim of this work is somewhat different however; the quantity to be measured is a line intensity, which may be represented by

(9) $$I = \int_{-\infty}^{\infty} f(t)\, dt \quad - C$$

where C represents a continuum value. In practice, we know a reasonably accurate value for C and also

(10) $$g'(t) = \frac{1}{2\pi} \int_{-\infty}^{\infty} \left[F(\omega) \cdot S(\omega) + N(\omega) \right] e^{i\omega t}\, d\omega$$

(11) $$g'(t) = g(t) + \frac{1}{2\pi} \int_{-\infty}^{\infty} N(\omega)\, e^{i\omega t}\, d\omega$$

where N(ω) represents the power spectrum of the noise which is added to a particular scan. For this argument the noise is represented by a stationary Gaussian random process with zero average. The problem then is to obtain a best approximation to the value of I.

If the response function has been normalized so that

(12) $$\int_{-\infty}^{\infty} s(t)\, dt = 1 = S(0)$$

it is easy to use Equation 5 to prove

(13) $$\int_{-\infty}^{\infty} g(t)\, dt = \int_{-\infty}^{\infty} f(t)\, dt$$

Thus,

(14) $$I + C = \int_{-\infty}^{\infty} g(t)\, dt$$

Taking

(15) $$G'(\omega) = F(\omega) \cdot S(\omega) + N(\omega)$$

and

(16) $$R'(\omega) = G'(\omega) \cdot S(\omega) = F(\omega) \cdot S^2(\omega) + N(\omega) \cdot S(\omega)$$

and

(17) $$R(\omega) = G(\omega) \cdot S(\omega) = F(\omega) \cdot S^2(\omega)$$

Then by the same argument used to derive Equation 14, it can be shown that

(18) $$I + C = \int_{-\infty}^{\infty} r(t)\, dt$$

where

$$(19)\quad r(t) = \frac{1}{2\pi}\int_{-\infty}^{\infty} R(\omega)\, e^{i\omega t}\, dt$$

The point of introducing these additional variables $r(t)$, $R'(\omega)$, AND R(W) is that under certain conditions using the transform of R'(w) to calculate I will give a more accurate value than will using the transform of G'(w)

Since either r(t) or g(t) will give the exact value of I, the difference is in what happens to the noise. Here it is probably best to use an example since each situation is different. For the scanning rates used in this experiemnt, the functions s(t) and S(W) are shown in Figures 36 and 37. The detector noise is white noise which is band limited by the output time constant of the electronics (0.5 second RC in this case). In this case, multiplying N(W) by S(W) further band limits the noise. The result is that r'(t) is a closer approximation to r(t) than g'(t) is to g(t).

While this method can decrease the noise, it is by no means the only way to do so and perhaps a comparison of some other approaches should be made. The discussion will be restricted to those methods which can be represented in the frequency domain of ω by a function which is normalized to a value 1.0 at $\omega = 0$. All of these functions will satisfy Equation 12 and by a derivation similar to that of Equation 13 it can be shown that they will not affect the equivalent width when multiplied by the transform of the received signal.

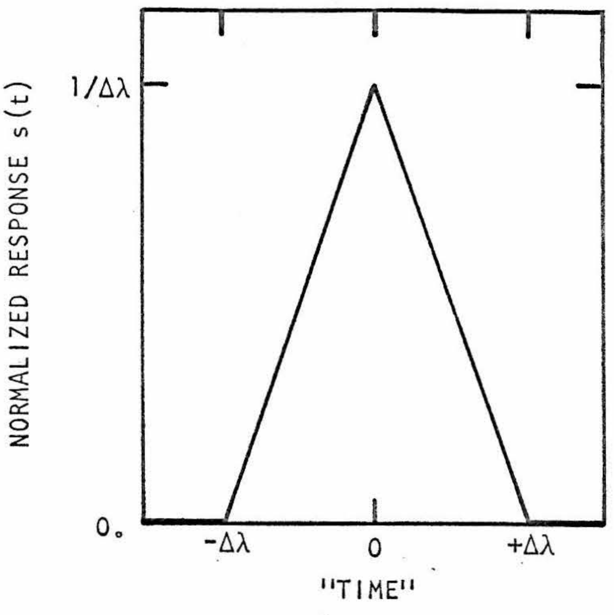

FIGURE 37 SLIT RESPONSE - TIME DOMAIN

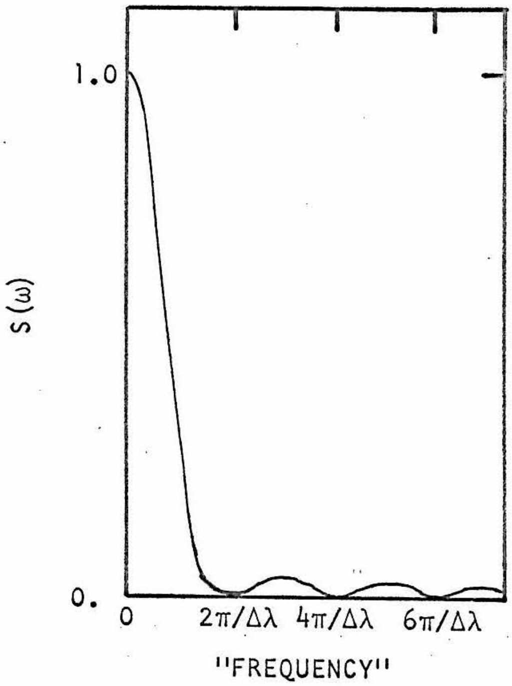

<u>FIGURE 38</u> SLIT RESPONSE - FREQUENCY DOMAIN

One method might involve multiplication by $S^2(\omega)$ instead of $S(\omega)$. While there would be a further band limiting of the noise, it would not be a significant increase over just multiplication by $S(\omega)$. There would also be a further degrading of the resolution to the point where an error in the value of C might be important, so, in general, this is not recommended. Also important to consider for this case and for the others to be discussed is that multiplication by $S(\omega)$ weights the noisy signal according to previous knowledge of what a noiseless signal looks like. Clearly this is an optimum treatment and any other function of ω such as $S^2(\omega)$ cannot do this. While this is the primary reason for choosing $S(\omega)$ for this experiment, other types of information may be desired and other functions may prove more convenient for other experiments.

A method sometimes used in communications engineering is simply to eliminate all frequencies above some frequency ω_0. It is possible to prove that this truncation method will give a new function of time y(t) which minimizes the overall RMS error, ϵ

$$(20) \qquad \epsilon = \int_{-\infty}^{\infty} |g(t) - y(t)|^2 \, dt$$

for a given band limited response. Using this method on this experiment's data would preserve the resolution and decrease the noise somewhat, but it would also introduce a "ringing" effect (Gibb's phenomenon).

A method often followed because of its practical ease is to use a long time constant when taking the data. A proper choice of time constant will provide an approximation to $S(\omega)$ which may be good enough for some purposes. The signal assymetry introduced and the long exponential decay make measurement a more difficult problem, however.

As a practical matter, it is often inconvenient to work in the transform domain of ω. Fortunately, the convolution theorem provides a way out. The function desired is

$$(21) \quad r'(t) = \frac{1}{2\pi} \int_{-\infty}^{\infty} G'(\omega) \cdot S(\omega)\, e^{i\omega t}\, dt$$

this can be transformed into

$$(22) \quad r'(t) = \int_{-\infty}^{\infty} g'(\tau) \cdot s(t-\tau)\, d\tau$$

Thus, by convolving the slit function with the spectral data, the S/N ratio is maximized in an optimum way.